Synchrotron X-ray Scattering Studies of Complex Oxides

A DISSERTATION
SUBMITTED TO THE FACULTY OF THE GRADUATE SCHOOL
OF THE UNIVERSITY OF MINNESOTA
BY

Biqiong Yu

IN PARTIAL FULFILLMENT OF THE REQUIREMENTS
FOR THE DEGREE OF
DOCTOR OF PHILOSOPHY

Advisor: Martin Greven

December, 2019

Acknowledgements

I express my sincere appreciation to those who have contributed to the research in this Thesis and who have supported me over the years. Without them, the completion of this Thesis work would not have been possible.

First and foremost, I would like to thank my advisor, Martin Greven, for his continual support during my Ph.D. study. His immense knowledge, valuable comments, and patient guidance greatly inspired my enthusiasm in research. I learn from him not only about physics, but also the skills of a scientific researcher: critical thinking, presentation, and academic writing. Further, I am grateful for the opportunities that Martin offered to travel worldwide to conduct synchrotron X-ray experiments, to attend conferences, workshops and summer schools, where I developed valuable skills as well as collaborations.

I would like to thank all my former and current colleagues here at the University of Minnesota for helping me on various subjects. My special thanks go to Wojciech Tabis, with whom I collaborated on most of my projects, and from whom I learned synchrotron X-ray scattering techniques. I also want to thank Guichuan Yu for arranging the trips to Argonne and teaching me some data analysis tricks. Thank you to Yangmu Li, Nina Bielinski, Sajna Hameed, Zach Anderson, and Yang Tang for their help with crystal growth and characterization, and to Damjan Pelc, Neven Barišić, and Nikolaos Biniskos for valuable discussions. I thank Chris Leighton and his students Jeff Walter, Vipul Chaturvedi, Joseph Gotchnik, and Will Postiglione for their guidance and help with electrolyte-gating techniques.

I learned a lot from the people I met and collaborated with at the beamlines: Kenji Ishii at SPring8, Japan; John Freeland, Diego Casa, Hua Zhou, and Zhan Zhang at the Advanced Photon Source (APS), Argonne, USA; Ronny Sutarto and Feizhou He

at the Canadian Light Source (CLS), Canada; Flora Yakhou, Nicholas Brookes, Alexey Bosak, Michaela Souliou, and Luigi Paolasini at the European Synchrotron Radiation Facility (ESRF), France. Thank you all for your generous support. I also thank Yuan Li and his students Lichen Wang, Biaoyan Hu, Xiangpeng Luo, and Junbang Zeng from Peking University, China for making the early morning (5 am) discussions at the CLS delightful. I appreciate the energetic time at the ESRF spent with Andrzej Kozlowski and his student Izabela Biało from the AGH University of Science and Technology, Poland.

I want to thank my Thesis committee members Chris Leighton, Andrey Chubukov, and Vlad Pribiag, as well as Allen Goldman, who served on my oral exam committee, for their time and valuable comments.

Thank you to my friends, Yanjun Yang, Jiashen Cai, Mengqun Li, Yuting Wang, Ming Li, Shuhui Luo, Yuguang Chen, Tianbai Cui, and Dehua Wang for your help and support with my study and life, especially during my first few months in the United States. I would like to thank Sajna Hameed and Vaidya Sethuraman for enjoyable lunch time discussions, and also for introducing me to the Indian community, which made my Ph.D. life much more cheerful. I thank Ruihan Liu for her encouragement during dark times. Thank you Hui Zhang, my lifetime friend since high school, for sharing the joy of life.

I am grateful to my parents for their unconditional and endless support. Finally, I thank Yangmu for his unbound love and companionship throughout this journey.

Abstract

Complex oxides, such as the copper-based high-temperature superconductors and the perovskite cobaltites, exhibit a vast range of properties and phases and are prominent research topics in condensed matter physics and materials science. Synchrotron X-ray techniques are powerful tools to study the electronic and magnetic properties of materials. In this Thesis, I present synchrotron X-ray scattering studies of four complex oxides: the cuprates $HgBa_2CuO_{4+\delta}$ (Hg1201), $La_{2-x}Sr_xCuO_4$ (LSCO), and $Nd_{2-x}Ce_xCuO_4$ (NCCO), and the cobaltite $La_{0.5}Sr_{0.5}CoO_{3-\delta}$ (LSCoO).

I first describe a study of the dynamic charge correlations in the moderately-doped model cuprate Hg1201 ($T_c = 70$ K) using resonant inelastic X-ray scattering (RIXS) at the Cu L-edge. The cuprates exhibit a charge-density-wave (CDW) instability in the underdoped, pseudogap part of the phase diagram that competes with superconductivity. This study aims to discern the connection between CDW and pseudogap phenomena, and to understand the extent to which CDW correlations shape the phase diagram. With a new analysis method, I demonstrate that the charge correlations at the two-dimensional wave vector $\boldsymbol{q}_{CDW} \approx (0.28, 0)$ feature three characteristic energy scales: (1) quasi-elastic; (2) $\sim$ 40 meV, in the optic-phonon range; (3) 150-200 meV, well beyond the phonon range. Intriguingly, the two dynamic energy scales identified here are comparable to previously measured pseudogap scales and to energy scales associated with the glue function deduced from optical and Raman spectroscopy. The paramagnon dispersion along [1,0] is also measured and found to be insensitive to the CDW correlations.

The dynamic charge correlations may manifest themselves as anomalous softening or broadening of phonon modes. In order to investigate this possibility, I carried out non-resonant inelastic X-ray scattering (IXS) measurements of Cu-O bond-stretching phonons in hole-doped LSCO and electron-doped NCCO. In LSCO ($x = 0.125$), anomalous phonon broadening is observed at low temperature ($T = 20$ K) around the wave vector $\boldsymbol{q}_{ph} \sim (0.25, 0)$, close to the CDW wave vector $\boldsymbol{q}_{CDW}$. The anomalous broadening is significantly weakened at higher temperatures ($T = 150$ K, 300 K) and higher

doping ($x = 0.20$). Measurements across the structural transition temperature T_s suggest that the effect is not due to unit cell doubling below T_s. Rather, the dynamic charge correlations appear to be the cause of the observed phonon broadening. The anomalous softening and broadening behavior is also observed in NCCO, but found to be independent of temperature (up to $T = 500$ K) and doping ($x = 0.078$, 0.145), and therefore is likely the result of an anti-crossing between two phonon modes rather than due to dynamic charge correlations.

Motivated in part by a recent phenomenological charge (de)localization model, which successfully captures the temperature and doping dependence of the pseudogap and strange-metal phenomena, I also studied the doping and temperature dependence of charge-transfer excitations in LSCO and NCCO via Cu K-edge RIXS. The measurements, which range from low temperature (15 K) to very high temperature (1200 K), reveal a distinct spectral weight decrease upon heating in both compounds that remains to be understood.

Finally, I present a synchrotron X-ray study of ion-gel-gated LSCoO thin films. Electrolyte-based transistors utilizing ionic liquids/gels have been highly successful in the study of charge-density-controlled phenomena in diverse materials, particularly oxides. Experimental probes beyond electronic transport have played a significant role, despite challenges to their application in the electric double-layer transistor geometry. I demonstrate the application of synchrotron *soft* X-ray absorption spectroscopy (XAS) and X-ray magnetic circular dichroism (XMCD) as *operando* probes of the charge state and magnetism in ion-gel-gated ferromagnetic perovskite thin film LSCoO/$LaAlO_3$(001). Application of gate voltages up to + 4 V is shown to dramatically suppress the O K-edge XAS pre-peak intensity and XMCD signal at the Co L-edges, and thus enables the Co valence and ferromagnetism to be tracked upon gate-induced reduction. This work lays the foundation for *operando soft* XAS/XMCD studies of other electrolyte-gated oxides, which could be especially illuminating in the case of battery, ionic conductor and supercapacitor materials.

Contents

List of Tables

List of Figures

List of Acronyms

ARPES	Angle-Resolved Photoemission Spectroscopy
Bi2201	$Bi_2Sr_2CuO_{6+\delta}$
Bi2212	$Bi_2Sr_2CaCu_2O_{8+\delta}$
CDW	Charge Density Wave
CT	Charge Transfer
CTB	Charge-Transfer Band
EDLT	Electric Double-Layer Transistor
EELS	Electron Energy Loss Spectroscopy
EI-RIXS	Energy-Integrated Resonant Inelastic X-ray Scattering
EMI:DCA	1-Ethyl-3-Methylimidazolium Dicyanamide
EMI:TFSI	1-Ethyl-3-Methylimidazolium Bis(trifluoro-methylsulfonyl)imide
ESRF	European Synchrotron Radiation Facility
FC	Field Cool
FL	Fermi Liquid
FWHM	Full Width at Half Maximum
Hg1201	$HgBa_2CuO_{4+\delta}$

Hg1212	$HgBa_2CaCu_2O_{6+\delta}$
Hg1223	$HgBa_2Ca_2Cu_3O_{8+\delta}$
HTT	High-Temperature Tetragonal
HWHM	Half Width at Half Maximum
INS	Inelastic Neutron Scattering
IXS	Inelastic X-ray Scattering
LCO	La_2CuO_4
LHB	Lower Hubbard Band
LSCO	$La_{2-x}Sr_xCuO_4$
LSCoO	$La_{1-x}Sr_xCoO_{3-\delta}$
LTO	Low-Temperature Orthorhombic
MO	Molecular Orbital
NBCO	$Nd_{1+x}Ba_{2-x}Cu_3O_{6+\delta}$
NCCO	$Nd_{2-x}Ce_xCuO_{4+\delta}$
NMR	Nuclear Magnetic Resonance
NQR	Nuclear Quadrupole Resonance
OP	Optimally Doped
OV	Overdoped
PG	Pseudogap
P(VDF-HFP)	Poly(Vinylidene Fluoride-Co-Hexafluoropropylene)
REF	Total Reflectivity
RIXS	Resonant Inelastic X-ray Scattering

RXS	Resonant X-ray Scattering
SC	Superconductivity
SDW	Spin Density Wave
SEM	Scanning Electron Microscopy
SHG	Second-Harmonic Generation
SM	Strange Metal
SQUID	Superconducting Quantum Interference Device
STM	Scanning Tunneling Microscopy
TEY	Total Electron Yield
TFY	Total Fluorescence Yield
TSFT	Traveling-Solvent Floating Zone
UD	Underdoped
UHB	Upper Hubbard Band
$\mathbf{V_O}$	Oxygen Vacancy
XAS	X-ray Absorption Spectroscopy
XMCD	X-ray Magnetic Circular Dichroism
YBCO	$YBa_2Cu_3O_{6+\delta}$
ZFC	Zero-Field Cool

Chapter 1

Introduction

Perovskite and peroskite-related oxides are of high interest in the fields of condensed matter physics and materials science as they exhibit a vast range of electronic and magnetic properties and phases. This Chapter briefly describes the two families of oxides studied in this Thesis: the lamellar copper-based high-temperature superconductors and the pseudocubic cobaltite $La_{1-x}Sr_xCoO_3$ (LSCoO). I first introduce the basic structural and electronic properties of cuprate materials, followed by an introduction to the electrolyte-gating technique applied to LSCoO thin films. Finally, I present the outline of this Thesis.

1.1 The Cuprates

1.1.1 High-Temperature Superconductivity

Superconductivity was first discovered in 1911 by Kammerlingh Onnes, who observed that the electrical resistivity of mercury falls to zero below a characteristic temperature of $T_c \approx 4.2$ K [1]. In the 1930s, Meissner and Ochsenfeld subsequently found that superconductors actively expel an externally-applied magnetic field [2], known as the Meissner-Ochsenfeld or perfect diamagnetism effect. The zero resistivity and Meissner-Ochsenfeld effect are the two defining properties of a superconductor.

It took until the 1950s for Bardeen, Cooper and Schrieffer to put forward a successful theoretical description of superconductivity, known as the BCS theory [3]. In their

theory, electrons overcome their mutual electronic repulsion and are coupled by quantized vibrations of crystal lattice (phonons) to form Cooper pairs. Naively, as bosonic pairs, these Cooper pairs condense into a macroscopic coherent state below a critical transition temperature T_c, and can then move through the lattice without electrical resistance. According to the theory, the magnitude of T_c is related to the strength of electron-phonon coupling V, as described by the formula $k_B T_c = 1.13 E_D e^{-1/(N(0)V)}$, where E_D is the Debye cutoff energy and $N(0)$ is the electronic density of states at the Fermi level [4]. It was predicted that superconductivity could not occur at temperatures higher than about 30 K. BCS theory, and the specific model of phonon-mediated pairing, constitute a major success of 20^{th} century science. More recently, it has been uncovered that exceptions may occur due to presence of very light atoms, e.g., $T_c \approx 203$ K was subsequently reported in H_2S under extremely high pressure of 155 GPa [5]. Note that it is important to distinguish between the BCS theory and the BCS model: the former is the general theory of superconductivity described by a retarded bosonic pairing glue, whereas the latter specifies that the pairing is mediated by electron-phonon coupling.

Despite intensive experimental efforts, the maximum T_c did not exceed 25 K for more than 70 years. In 1986, Bednorz and Müller announced evidence for superconductivity in the copper-oxide (also referred to as "cuprate") $La_{2-x}Ba_xCuO_4$ at about 30 K [6]. This breakthrough opened a major new field of research. In the following years, superconductivity was reported in numerous cuprate compounds, in many cases with a T_c value higher than the boiling point of the liquid nitrogen (77 K), a benchmark for industrial applications. Interestingly, the superconductivity in these materials cannot be explained by the standard BCS model of phonon-mediated pairing, and thus is referred to as unconventional superconductivity [7].

In addition to the cuprates, other families of superconductors also exhibit unconventional superconducting behavior, including the iron-pnictide, heavy-fermion, and organic superconductors. Remarkably, more than thirty years after Bednorz and Müller's seminal discovery, the underlying mechanism of superconductivity in these unconventional superconductors is still actively debated, and high-temperature superconductivity remains a major research topic in the field of condensed matter physics.

1.1.2 Crystal Structures

There exist well over 100 cuprate superconductors, all of which share a common structural building block: the two-dimensional copper-oxygen (CuO_2) sheet. The CuO_2 sheets are stacked with intermediate compound-dependent charge reservoir layers, forming a three-dimensional structure. A schematic diagram of the CuO_2 sheet and lattice structure is shown in Figure 1.1. The charge-carrier density of the CuO_2 sheets can be tuned by altering the chemical composition of the charge reservoir layers. The undoped parent compounds, e.g., La_2CuO_4 and Nd_2CuO_4, are Mott insulators as a result of strong electronic correlations. Depending on the type of carriers, the cuprates are classified as either hole- or electron-doped. The majority of cuprates are hole-doped, including $HgBa_2CuO_{4+\delta}$ (Hg1201) studied in Chapter 3, and $La_{2-x}Sr_xCuO_4$ (LSCO) investigated in Chapters 4 and 5. On the other hand, $Nd_{2-x}Ce_xCuO_4$ (NCCO), studied in Chapters 4 and 5, is a prototypical electron-doped cuprate.

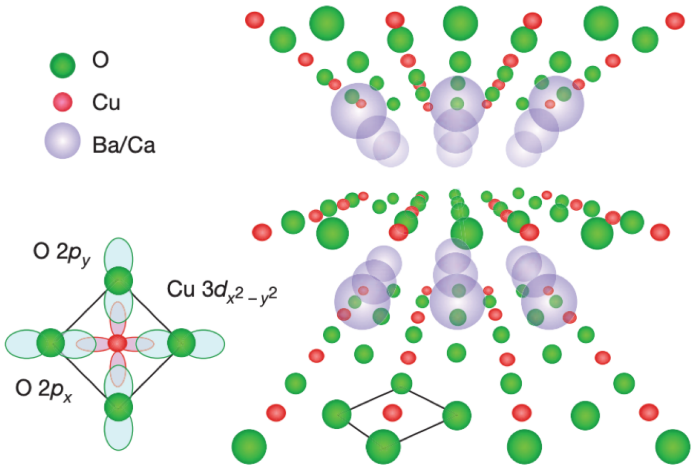

Figure 1.1: Schematic of CuO_2 sheet, reproduced from [7]. Each of copper atom (red) in the CuO_2 sheet is surrounded by four planar oxygen atoms (green). The bottom left figure illustrates the hybridization of Cu $3d_{x^2-y^2}$ and O $2p_{x,y}$ orbitals that is crucial to the unusual properties of the cuprate superconductors.

The cuprates can also be classified based on the number of CuO_2 sheets per unit cell. Nearly all of the materials studied in this Thesis (Hg1201, LSCO, and NCCO) are single-layer compounds, with one CuO_2 sheet per primitive cell. Cuprates with more

than one CuO_2 layer per primitive cell are common. For instance, $HgBa_2Ca_2CuO_{8+\delta}$, which exhibits the highest $T_c \sim 135$ K at ambient pressure of all known materials, is a three-layer ($n = 3$) compound. In the introduction of Chapter 3, I briefly summarize our collaborative CDW results for double-layer $HgBa_2CaCu_2O_{6+\delta}$ (Hg1212). For a family of cuprates with the same charge-reservoir layers, T_c increases with the number of CuO_2 sheets up to $n = 3$, and then decreases with larger n. Although the initial increase of T_c is still under investigation, the subsequent decrease is ascribed to the increasing difficulty in simultaneously optimizing the charge concentrations of all CuO_2 sheets [8].

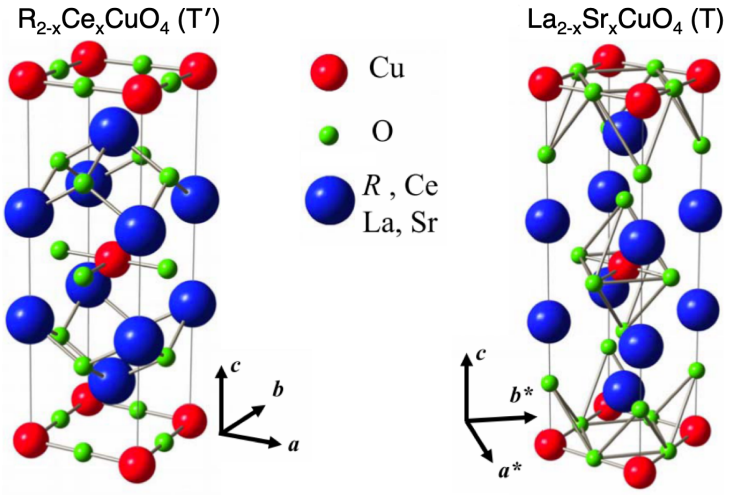

Figure 1.2: Crystal structures of single-layer electron- and hole-doped cuprates, reproduced from [9]. Left: T′ structure of electron-doped $R_{2-x}Ce_xCuO_4$ (R is one of a number of rare-earth ions: Nd, Pr, Sm, or Eu). Right: T structure of $La_{2-x}Sr_xCuO_4$.

Notable differences are revealed between electron- and hole-doped cuprates after close inspection [10, 11]. Figure 1.2 compares the T′ crystal structure of the electron-doped cuprates and the T structure of their closest hole-doped counterpart, LSCO. In the T structure, the planar copper atom is surrounded by six oxygen atoms, four in the plane, and two at the apical position, whereas in the T′ structure, the apical oxygens are nominally absent. Typical room-temperature lattice parameter are $a = b = 3.95$ Å and $c = 12.15$ Å for NCCO, and $a = b = 3.81$ Å and $c = 13.2$ Å for LSCO. Whereas NCCO is tetragonal at all temperatures, LSCO undergoes a structural transition to an orthorhombic phase (e.g., at $T_s \sim 530$ K for undoped $LaCuO_4$).

1.1.3 Electronic Structures

The electronic structures of the cuprates are dominated by the CuO_2 layers, especially the hybridized Cu $3d_{x^2-y^2}$ and O $2p_{x,y}$ orbitals (see Figure 1.1). Some studies point to small admixtures of out-of-plane orbitals, e.g., Cu $d_{z^2-r^2}$, although the contributions from these out-of-plane orbitals are believed to be less than 10% [12, 13]. As a result of the Coulomb potential due to the surrounding O^{2-} ions, the five nominally degenerate $3d$ Cu^{2+} orbitals are split in energy, with $3d_{x^2-y^2}$ being the highest-energy orbital. In the undoped parent compounds, the Cu^{2+} ions feature nine out of a maximum of ten $3d$ electrons. Band theory therefore predicts a half-filled conduction band, i.e., the parent compounds to be good metals. However, it turns out that the undoped compounds are insulating. This seeming contradiction can be understood by considering the on-site electron-electron interaction, i.e., there is a significant energy cost U for two electrons to occupy the same $3d_{x^2-y^2}$ orbital due to their mutual Coulomb repulsion. The undoped parent compounds therefore are Mott insulators. Theoretically, one often considers the single-band Hubbard model:

$$H = \sum_{ij} t_{ij} c_i^\dagger c_j + U \sum_i n_{i\sigma} n_{i\sigma'}, \tag{1.1}$$

where i and j label sites on a square lattice, σ and σ' are the spin states, t_{ij} is hopping energy between site i and j, $c_i^\dagger$ and c_j are the creation and annihilation operators, U is the on-site interaction energy, and $n_{i\sigma}$ is the number operator $c_{i\sigma}^\dagger c_{i\sigma}$. Charge fluctuations are strongly suppressed in the case of a large local Coulomb interaction U. If $U \gg t_{ij}$, the band structure of the undoped system ("half-filling") can be described by an empty upper Hubbard band (UHB) and a filled lower Hubbard band (LHB), and the Fermi level lies in the middle of the Mott gap, as shown in Figure 1.3a.

The situation is more complicated, in fact, as the cuprates are better characterized as charge-transfer Mott insulators. This is due to the presence of nearby O^{2-} ions, specifically the $2p_{x,y}$ orbitals along the Cu-O bond direction. The energy level of the O $2p_{x,y}$ orbital lies between the UHB and LHB of the Cu $3d_{x^2-y^2}$ orbital. Therefore, it is easier to excite an electron from an occupied O $2p_{x,y}$ orbital than from the LHB. Figure 1.3b shows this schematically. Upon doping, holes tend to reside in the so-called charge-transfer band (CTB), which is primarily composed of O $2p_{x,y}$ orbitals, whereas

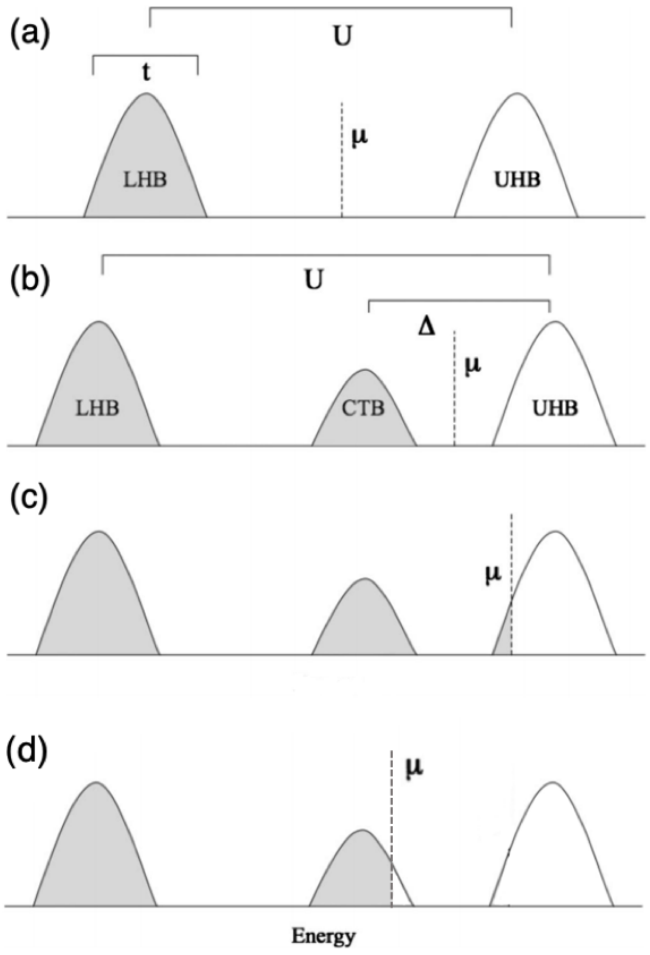

Figure 1.3: Schematic of Hubbard and charge-transfer insulator band structures, adapted from [9]. (a) Single-band Hubbard model with empty upper Hubbard band (UHB) and filled lower Hubbard band (LHB). μ denotes the chemical potential and lies in the middle of the Mott gap in the undoped, half-filling case. (b) Charge-transfer insulator. The charge-transfer band (CTB) lies between the UHB and the LHB. Δ is the charge-transfer gap between CTB and UHB. (c) Band structure of electron-doped cuprates. The chemical potential μ moves upward into the UHB upon doping with electrons. (d) Band structure of the hole-doped cuprates. The chemical potential μ moves downward into the CTB.

doped electrons tend to occupy Cu sites and to fill the UHB. The charge-transfer gap, Δ, between the CTB and the UHB is found to be 1-2 eV in the parent compounds [14]. The doping and temperature dependence of Δ (and the emerging charge excitations below Δ) is the focus of Chapter 5.

The three-band Hubbard model involves all three orbitals (Cu $3d_{x^2-y^2}$ and O $2p_{x,y}$) and hence enables, in principle, a more accurate description of the doped CuO_2 sheets [15]. However, this model is currently unsolvable. By treating the charge-transfer gap Δ as an effective Hubbard U, and considering the Zhang-Rice singlet [16] band as an effective LHB, the three-band Hubbard model can be simplified to an effective single-band model (Equation 1.1).

It is possible to reduce the sinlge-band Hubbard model further by taking the limit $U \gg t$, such that no two electrons occupy a single site. At half-filling, the localized electrons have oppositely-aligned spins on adjacent sites and can reduce their kinetic energy via virtual hops between neighboring sites. This hopping process is prohibited for electrons with parallel spins, due to Pauli exclusion. This gives rise to an antiferromagnetic interaction, $J \approx 4t^2/U$. Neglecting correlated-hopping terms, the single-band Hamiltonian then reads:

$$H = \sum_{ij} t_{ij} \tilde{c}^{\dagger}_{i,\sigma} \tilde{c}_{j,\sigma} + J \sum_{i,j} (S_i \cdot S_j - \frac{n_i n_j}{4}), \tag{1.2}$$

where $\tilde{c}_{i\sigma} = c_{i\sigma}(1 - n_{i,-\sigma})$ to exclude doubly-occupied states, and $S_{i,j}$ is the spin operator. Equation 1.2 is the t-J model, which is widely used to understand the electronic and magnetic properties of the cuprates. A next-nearest hopping term, t', and next-next-nearest term, t'', are often introduced to refine the model and obtain better agreement with experimental results.

1.1.4 Phase Diagram

Since the 1986 discovery of high-temperature superconductivity in the cuprates, a vast range of experimental and theoretical studies have been carried out to investigate the physical properties of these complex oxides. Figure 1.4 shows the phase diagram of the hole-doped cuprates [7]. The undoped compounds are antiferromagnetic Mott (charge-transfer) insulators. The antiferromagnetic order is rapidly suppressed when holes are

doped into the CuO_2 sheets. Superconductivity occurs upon further doping, and T_c has a dome-like shape. At optimal doping ($p_{op} \approx 0.16$), T_c is maximal. Materials with $p < p_{op}$ are referred to as underdoped, and those with $p > p_{op}$ as overdoped. In the heavily overdoped regime, the cuprates exhibit the properties of a conventional Fermi-liquid metal [17–19]. Above the T_c dome, there are two robust regimes in the phase diagram: the strange metal and the pseudogap. The strange metal is characterized by T-linear planar resistivity above T^*. Below T^*, the system enters the pseudogap phase, where the Fermi surface is partially gapped. The pseudogap phase exhibits a number of ordering tendencies, including charge-spin stripe, spin-density-wave (SDW), and charge-density-wave (CDW) order. The dynamic CDW response and the possible coupling to optical phonons are the focus of Chapters 3 and 4, respectively. Chapter 5 is motivated by the desire to better understand the charge-transfer excitations of the doped CuO_2 sheets.

This Thesis work also includes studies of phonon anomalies (Chapter 4) and of charge-transfer excitations (Chapter 5) of the archetypal electron-doped cuprate NCCO. Although the electron- and hole-doped cuprates exhibit many of the same phases, there exists a considerable electron-hole asymmetry. For example, antiferromagnetic correlations are much more robust in the electron-doped cuprates [9]. CDW correlations also exist in NCCO and persist to higher temperatures [20,21]. The studies of NCCO aim to provide a comparison with the hole-doped counterparts as well as meaningful insights into universal aspects of high temperature superconductivity.

1.2 The Cobaltites

1.2.1 Bulk and Thin-Film Properties

The cobaltites are of particular interest, as they lie in the crossover region between Mott and charge-transfer insulator. The $x = 0$ parent compound $LaCoO_3$ is a non-magnetic semiconductor. Substitution of Sr for La introduces holes to the system and increases the valence state of Co from 3+ to 4+. Meanwhile, with one less electron in the $3d$ orbital, Co^{4+} has a nonzero spin state, which causes dramatic changes in magnetic properties. The evolution of magnetic and electronic properties in the $La_{1-x}Sr_xCoO_{3-\delta}$ (LSCoO) system upon Sr doping is usually described by a simple percolation picture

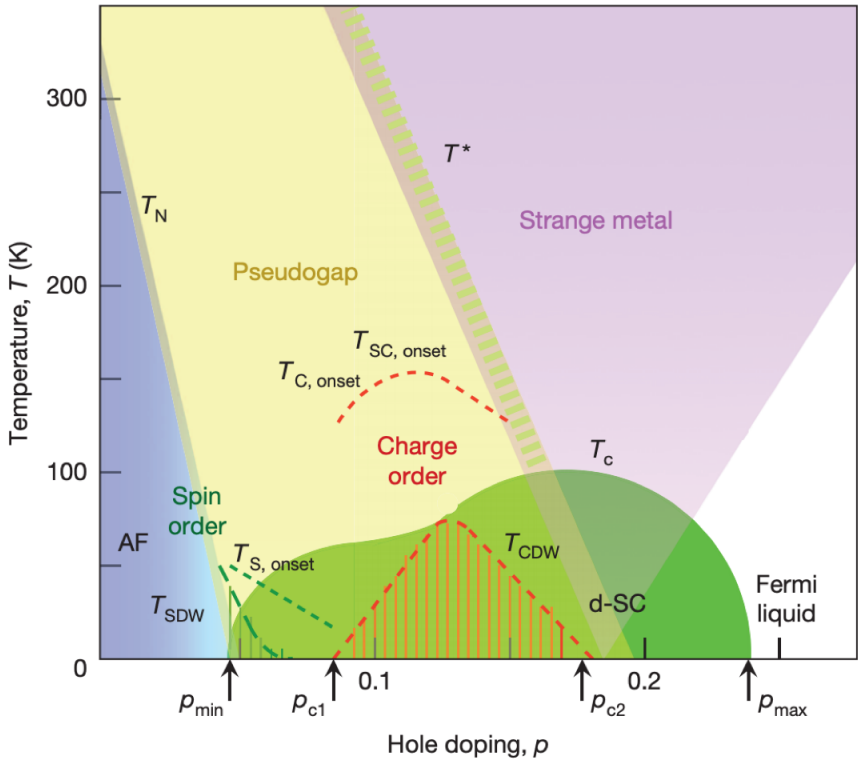

Figure 1.4: Phase diagram of the hole-doped cuprates, reproduced from [7]. The blue and green areas indicate the antiferromagnetic and superconducting phases with characteristic temperatures T_N and T_c, respectively. $T_{S,onset}$ and $T_{C,onset}$ denote the onset temperatures of short-range spin-density-wave (SDW) and charge-density-wave (CDW) correlations. T^* is the pseudogap temperature below which the Fermi surface is partially gapped. T_{CDW} and T_{SDW} indicate the long-range CDW and SDW order observed in some cuprates. p_{min}, p_{max}, p_{c1} and p_{c2} are characteristic doping levels for superconductivity and charge order.

(Figure 1.5). Nanoscopic ferromagnetic clusters start to form in a non-magnetic matrix at $x \approx 0.05$. The clusters grow as doping is increased, percolate at $x \approx 0.18$, and form a homogeneous ferromagnetic metal at $x \approx 0.22$ [22–26].

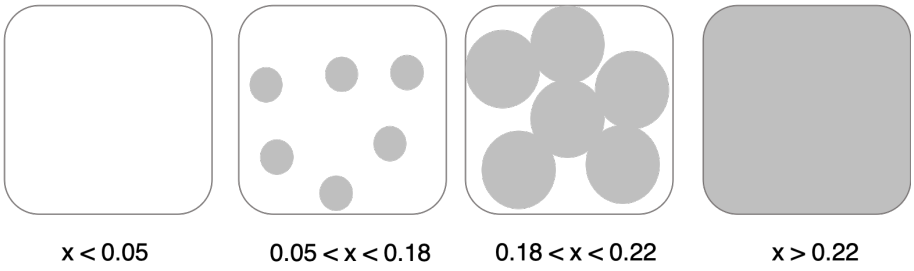

Figure 1.5: Schematic of percolative magnetic and electronic states in $La_{1-x}Sr_xCoO_{3-\delta}$. Grey area: ferromagnetic metal phase; white area: insulating non-magnetic phase.

In the LSCoO lattice, all Co-O distances and Co-O-Co angles are the same, whereas there are three different La-O distances because of the tilting of adjacent CoO_6 octahedra along the cubic axis (Figure 1.6) [27]. These different La-O distances gradually become close to each other as x increases, and the system eventually forms a cubic structure at $x > 0.55$ [27].

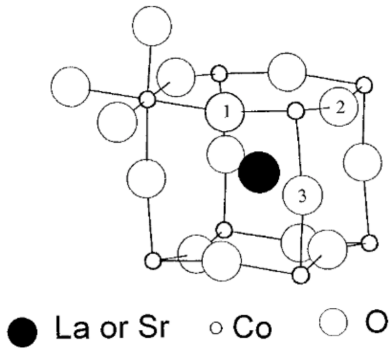

Figure 1.6: Distorted cubic structure of $La_{1-x}Sr_xCoO_{3-\delta}$, reproduced from [27]. The numbers (1, 2 and 3) indicate oxygen sites with different La-O distances.

The other feature of LSCoO that is important to this Thesis work is the formation of oxygen vacancies due to the unstable Co^{4+} state [28]. The oxygen vacancies occur especially at high Sr concentrations, where two electrons from O^{2-} are donated back to

the lattice in order to compensate the hole doping in the simplest model. The resulting effective doping level then becomes $x_{\text{eff}} = x - 2\delta$, with δ being the oxygen deficiency. In thin films, in order to accommodate the lattice mismatch between the film and substrate, oxygen vacancy ordering occurs [29, 30]. Recent work also demonstrates that magnetic anisotropy in LSCoO can be controlled by strain-engineered vacancy ordering [31].

The wealth of electronic and magnetic properties as well as the ease of forming oxygen vacancies make LSCoO an ideal material for detailed electrolyte gating studies.

1.2.2 Electrolyte Gating

In perovskites and perovskite-derived oxides, one typically varies the charge-carrier concentration via cation/anion substitution or by changing the interstitial oxygen density. Both methods introduce disorder and inhomogeneity, often cause considerable sample-to-sample variation of macroscopic physical properties, and do not allow continuous charge concentration control. A rather novel method of potentially reversible charge control is doping via an applied electric field [32–35]. Continuous doping control has been demonstrated in a wide variety of systems, such as the cuprate high-temperature superconductors [36–39], colossal magnetoresistance manganites [40, 41], and organic semiconductors [42]. Due to the strong charging capability of electrostatic doping, it was possible to induce superconductivity in the wide-gap insulators $KTaO_3$ [43] and $SrTiO_3$ [44]. It is notable that it has not been possible to dope $KTaO_3$ to become superconducting with conventional methods.

The most efficient electrolyte doping involves gating the material of interest in a so-called electric double-layer transistor (EDLT) structure using an ionic liquid or ionic gel, as shown in Figure 1.7. Such structures are nanoscale capacitors with highly mobile ions in the electrolytes, providing giant specific capacitances and very high areal charge densities ($> 10^{14}$ cm^{-2}) [41, 43, 45–48]. The carriers can be induced into the sample electrostatically via applying a voltage drop across the electrolyte/sample interface. However, it is now widely accepted that, in addition to electrostatic doping, the operating mechanisms of EDLTs also involve various other responses [34, 35, 49–51]. For example, in the electrolyte-gated oxides, an electric field often induces redox, particularly via oxygen vacancy formation. Initial evidence for oxygen vacancy formation came from transport measurements in a controlled atmosphere, and with tracking of

irreversibility [52–58]. Although charge transport measurements continue to be the main technique in the field of electrolyte gating, novel *operando* probes such as hard X-ray diffraction [59–62], X-ray absorption spectroscopy [60, 63], and neutron reflectometry [59, 64] have the potential to provide fruitful insights. In fact, in order to understand the doping mechanisms and advance this promising field, the development of new *operando* probes complementary to transport is essential. This is the motivation for the study in Chapter 6, where soft X-ray absorption spectroscopy (XAS) and X-ray magnetic circular dichroism (XMCD) measurements of electrolyte-gated thin films are performed for the first time.

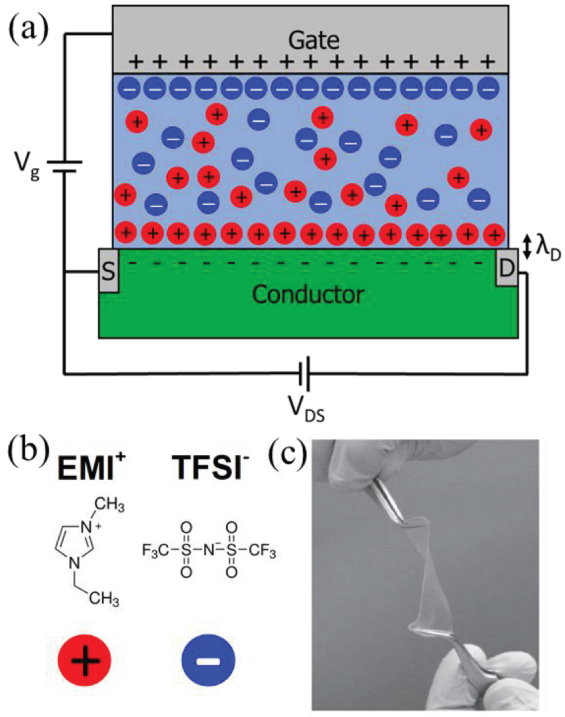

Figure 1.7: Illustration of electrolyte gating, reproduced from [65]. (a) Schematic of an electric double-layer transistor (EDLT). The middle blue area indicates the ionic liquid or gel with representative cations and anions. S and D are the source and drain electrodes. (b) Molecular structures of the ionic liquid EMI:TFSI. (c) Picture of a practical "cut-and-stick" ion gel [66].

1.3 Outline of this Thesis

Chapter 2 describes the experimental methods that I used for my Thesis work. Single crystals were grown using traveling-solvent floating-zone (TSFZ) or flux growth methods, and then were characterized by X-ray Laue diffraction and superconducting quantum interference devices (SQUID) magnetometry. The basic theoretical background of non-resonant inelastic X-ray scattering (IXS) and resonant inelastic X-ray scattering (RIXS) is also discussed.

Chapter 3 describes a Cu L-edge RIXS study of the model cuprate Hg1201 with nearly unprecedented energy resolution. The experiment was performed at beam line ID32 of the European Synchrotron Radiation Facility (ESRF), Grenoble, France. In addition to the expected observation of quasi-elastic charge-density-wave (CDW) order at low temperature, using a new analysis method, I demonstrate the existence of dynamic charge correlations with characteristic scales of about 40 meV and 150-200 meV. The existence of three distinct features in the charge response is highly unusual for a CDW system, and suggests that charge order in the cuprates is closely related to the pseudogap phenomenon and more complex than previously thought. In addition, I determine the paramagnon dispersion across $\boldsymbol{q}_{\mathrm{CDW}}$ and find it to be insensitive to the CDW correlations. Finally, I discuss the possible connection among these two dynamic charge scales, the magnetic excitations, and the superconducting glue function.

Chapter 4 describes IXS measurements of the Cu-O bond-stretching phonon in LSCO and NCCO. In LSCO ($x = 0.125$), at low temperature, the phonon linewidth exhibits an anomalous broadening around $\boldsymbol{q}_{ph}$, consistent with the CDW vector $\boldsymbol{q}_{CDW}$. The broadening effect is significantly weakened at higher temperature and higher doping ($x = 0.20$). Measurements across the structural transition temperature, T_s, suggest that the effect is not due to unit cell doubling below T_s. Rather, the presence of dynamic charge correlations might be the cause of the phonon broadening. Anomalous phonon softening and broadening is also observed in NCCO, but found to be independent of temperature and doping ($x = 0.078$ and $x = 0.145$). The scenario of anti-crossing between two phonon modes is thus proposed in the case of NCCO.

Chapter 5 describes a study of the temperature dependence of charge-transfer excitations in LSCO and NCCO using Cu K-edge RIXS. I first describe prior RIXS measurements of the doping dependence of charge-transfer excitations in LSCO as well as a phenomenological charge (de)localization model, which are the motivation of this study. The Cu K-edge RIXS measurements, which range from low temperature (15 K) to very high temperature (1200 K), reveal a distinct spectral weight decrease upon heating in both compounds. The results indicate dissimilar doping and temperature effects that remain to be understood.

Chapter 6 demonstrates synchrotron $soft$ XAS/XMCD as *operando* probes of the charge state and magnetism in ion-gel-gated ferromagnetic $LaAlO_3(001)$/LSCoO thin films. As a first step, in order to establish baseline behavior, XAS/XMCD measurements of 4-25 unit-cell-thick films are shown to probe the evolution of hole density and ferromagnetism. *Operando* soft XAS/XMCD of electrolyte-gated films is then demonstrated, using specifically optimized spin-coated gels with thickness down to $\sim$1 μm and specific composition. Application of gate voltages up to + 4 V is shown to dramatically suppress the O K-edge XAS pre-peak intensity and XMCD signal at the Co L-edges, and thus enables the response of Co valence and ferromagnetism to be tracked upon gate-induced reduction. This work lays the foundation for *operando* $soft$ XAS/XMCD studies of other electrolyte-gated oxides, which could be especially illuminating in the case of battery, ionic conductor and supercapacitor materials.

At the time of completing this Thesis, the dynamic CDW correlation study of Hg1201 described in Chapter 3 [67] and the *operando* $soft$ XAS/XMCD study of ion-gel-gated LSCoO thin films discussed in Chapter 6 [68] have been submitted for publication. A manuscript describing the NCCO phonon work (Chapter 4) is in preparation, whereas the LSCO phonon work will require additional measurements in the future. Similarly, the work on the charge-transfer excitations described in Chapter 5 may benefit from additional measurements with higher energy resolution. However, a related manuscript on the effect of the reduction step on charge-transfer excitations in NCCO is currently in preparation (work not discussed in Chapter 5). In addition to the work described in this Thesis, I contributed to numerous other experiments. These include the RXS measurement of CDW correlations in Hg1201 [69], NCCO [21, 70], and Hg1212 [71],

the growth of Hg1212 single crystals [72], and hard X-ray diffraction studies of ion-gelgated LSCoO [59] and $BaSnO_3$ thin films [73]. Moreover, some of the crystals that I prepared were studied with a new nonlinear magnetic response technique [74], and are presently investigated via angle-resolved photoemission spectroscopy (ARPES) and second-harmonic generation (SHG) optical measurements.

Chapter 2

Experimental Methods

In this Chapter, I describe the experimental methods that I used throughout this Thesis work. The in-house laboratory work involved crystal growth and characterization. The key experiments were performed at various national and international synchrotron X-ray facilities. The synchrotron-based X-ray techniques used are non-resonant inelastic X-ray scattering (IXS; Chapter 4), resonant inelastic X-ray scattering (RIXS; Chapters 3 and 5), and X-ray absorption spectroscopy/X-ray magnetic circular dichroism (XAS/XMCD; Chapter 6). In essence, XAS/XMCD constitutes the first step in the RIXS process, and therefore is not discussed separately in the present Chapter.

2.1 Crystal Growth

Successful experimental efforts in condensed matter physics crucially depend on the quality of the samples to be investigated. Typically, the earliest available samples of a new material are polycrystalline powders. Studies of polycrystalline samples have a fundamental limitation, because the individual crystallites are randomly oriented, such that spatial information is averaged over. In order to achieve satisfactory experimental understanding of quantum materials and their typically anisotropic behavior, the study of single crystalline samples is essential.

A prime example are the high-T_c superconductors, which consist of copper-oxygen (CuO_2) sheets that are separated by intervening layers of other atoms, and exhibit highly anisotropic electronic properties. In fact, it is thought by many that the unusual

properties exhibited by these quantum materials originate from the highly correlated CuO_2 sheets. Single crystals thus are necessary to study the quasi-two-dimensional properties of these materials. Two crystal growth methods, traveling-solvent floating zone (TSFZ) and flux growth, are used and developed in our research group to obtain high-quality single crystals.

2.1.1 Traveling-Solvent Floating-Zone Growth of LSCO

Single-grain crystals of many materials can be obtained by slowly solidifying melt or vapor that consists of the elements of the desired crystal. Industrial single-crystal silicon is produced in this manner. One might guess that single crystals can be easily grown, given a high enough starting temperature and a slow enough cooling rate, and that the slower the cooling rate, the larger crystals that are obtained. However, unlike elemental silicon, most cuprates cannot be grown in this manner due to their incongruous-melting nature. That is, as the material is heated, it decomposes into a mixture of transition-metal oxide solid and Cu-rich liquid. Figure 2.1 shows the temperature-composition phase diagram of the La_2O_3-CuO system as an example. According to this phase diagram, stoichiometric La_2CuO_4 decomposes into La_2O_3 solid and CuO liquid above 1320 °C, and additional CuO liquid flux is needed to fully dissolve the La_2O_3-CuO system into liquid melt. The melting point of the system decreases with increasing CuO composition and reaches a minimum at 90% mol CuO. A good window for the growth of La_2CuO_4 single crystals is the CuO composition range between 70% and 90% and the temperature range between 1050 °C and 1320 °C.

The easiest way to grow La_2CuO_4 single crystals is the so-called flux- or solvent-growth. Once appropriate amounts of La_2CuO_4 and CuO flux have been mixed well and put into a crucible, the crucible is heated up to high temperature until the the mixture melts completely, and then slowly cooled down. As the melt is cooled across the solidus line in Figure 2.1, it starts to precipitate La_2CuO_4 single crystals. Note that, as more and more La_2CuO_4 precipitates from the melt, the melt composition changes, following the solidus line. If the melt reaches the eutectic point, the entire melt will solidify with a large portion of CuO remaining in the mixture. Once the crucible has been cooled to room temperature, the La_2CuO_4 single crystals can be removed mechanically from the solidified mixture. Crystals grown by the flux method often have CuO secondary phase

inclusions and impurities from the crucible material. For example, in the early days of cuprate research, it was common to use Pt crucibles, which led to Pt impurities on the Cu site [75].

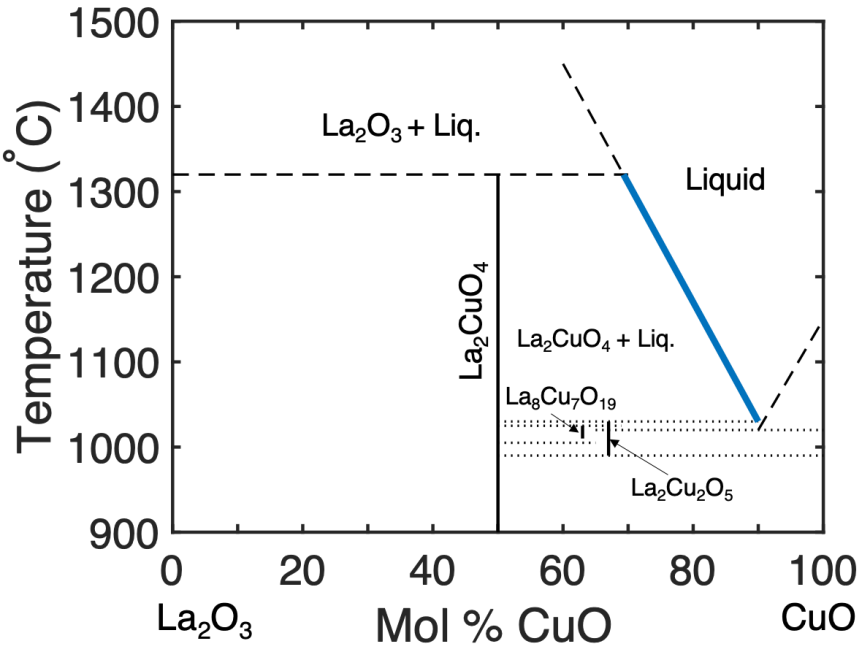

Figure 2.1: Temperature-composition phase diagram of the La_2O_3-CuO system, adapted from [76, 77]. The solid single-phase compositions are shown as black solid lines. The target material La_2CuO_4 lies at 50% CuO composition. Above 1320 °C, La_2CuO_4 decomposes into solid La_2O_3 and Cu-rich liquid phase, thus single-phase La_2CuO_4 cannot be obtained by simply cooling the polycrystalline material with this chemical composition from the melting point. Rather, the growth of La_2CuO_4 needs to start in a CuO rich melt, with a CuO composition between 70% and 90%. The solidus line, below which single phase La_2CuO_4 completely solidifies, is highlighted in blue.

A more advantageous method is traveling-solvent floating-zone (TSFZ) growth, which eliminates the usage of crucibles. This technique suspends the molten material between the polycrystalline feed rod and growing crystal by surface tension. The high-temperature molten zone is achieved by focusing light from halogen lamps using elliptical mirrors. The molten zone is usually a small volume, around 5 mm in height and diameter, depending on the size of needed crystal. During the growth, the mirror

stage including the lamps moves slowly upward, the polycrystalline material melts into the top part of molten zone, and "freezes" out at the bottom of the zone, forming the growing single crystal. Compared to the traditional flux method, much larger single-grain crystals can be obtained using the TSFZ technique. Figure 2.2 is a photo of the TSFZ furnaces in our laboratory, and Figure 2.3 illustrates the interior of such a furnace.

Figure 2.2: Photo of TSFZ furnaces.

The first step involved in the TSFZ growth is to prepare polycrystalline powders. For Sr-doped La_2CuO_4, chemical powders of La_2O_3 (99.99%), $SrCO_3$ (99.99%) and CuO (99.99%) are first dehydrated above 200 °C for 2 hours to ensure accurate chemical compositions. Stoichiometric quantities of powders are weighed using an analytic balance, and mixed using a mortar and pestle. In order to significantly reduce the particle size and to increase the homogeneity of the mixed powders, ethanol is usually added to the mixture in the first round of the mixing process. The mixed powers are then collected into an alumina crucible and heated to high temperature (950 °C) for 12 hours. The

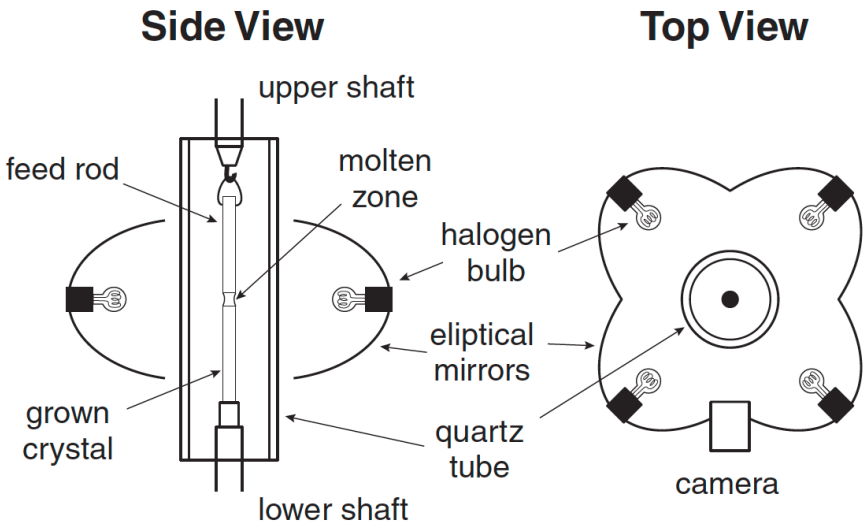

Figure 2.3: Illustration of the TSFZ furnace, reproduced from [78].

resultant solid-state chemical reaction can be expressed as:

$$(1-\frac{x}{2})\cdot La_2O_3 + x\cdot SrCO_3 + CuO + \frac{x}{4}\cdot O_2 \rightarrow La_{2-x}Sr_xCuO_4 + x\cdot CO_2. \qquad (2.1)$$

The grinding and baking process is repeated five times to ensure that powders are fully reacted. The final powders are black and have fine particle size. X-ray powder diffraction indicates that the powders are single-phase $La_{2-x}Sr_xCuO_4$ (LSCO). The next step is to transform these powders into a polycrystalline feed rod for use in the TSFZ furnace. A thin latex tube and a glass funnel are used to pack the powders into a uniform cylindrical shape (typically 5-6 mm in diameter and 7-10 cm in length). Once all the powders are packed into the latex tube, the tube is connected to a vacuum pump to evacuate air, and then sealed and compressed in a hydrostatic press. The latex tube is then carefully cut away from the powder rod after the compression. The resultant fragile powder rod is immediately baked at 980 °C for 12 hours . The hardened rod is then suspended by a high-temperature-resistant Ni-Cr wire inside the TSFZ furnace and sintered at high temperature (close to the doping-dependent decomposition temperature) for 20 hours. The rod is much denser after this sintering step, and light reflection from tiny polycrystals on its surface is visible. Figure 2.4a shows a picture of

a high-temperature sintered LSCO feed rod.

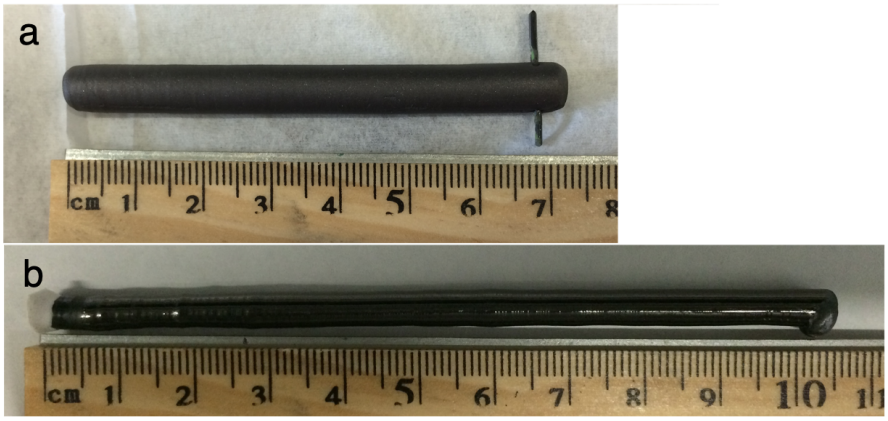

Figure 2.4: Pictures of LSCO (a) feed rod and (b) crystal grown by the TSFZ method. The $\sim$ 7 mm long feed rod was sintered at high temperature. The LSCO crystal is roughly 10.5 cm long and 5 mm in diameter. Most of this crystal is single-grain.

The seed rod is usually a small piece of single crystal (10 mm long) cut from an earlier growth. It is not necessary for the seed to have the same composition as the feed rod. If single crystals are not available, a short polycrystalline rod (such as a section of a feed rod) can also serve as seed. The seed is glued to an alumina post, which is in turn connected to a holder. The holder can be screwed to the lower shaft of the TSFZ furnace and has six screws on the side to adjust the position of the seed to ensure that it lies along the central axis of the furnace.

The flux rod is prepared in the same manner as the feed rod. It contains a La_2O_3-CuO mixture with 85% CuO. The flux rod is cut into small pellets, each with mass around 350 mg, which are heated at 980 °C for 12 hours. In an earlier growth protocol, there was a "melting flux" step before the actual growth, in which a small piece of the flux pellet was melted and attached to the polycrystalline feed rod which was mounted upside down in the furnace. The feed rod with flux attached was then taken out and aligned well with the seed rod to start the growth. I found this step unnecessary for the growth of LSCO, and instead mounted the feed and seed rods with a flux pellet sitting on top of the seed. At the beginning of the growth, the top part of the flux melts first, the feed rod can easily "pick up" the flux, and the latter forms a drop at the tip of the

feed rod as the temperature is increased. The feed and seed rods can then be attached to start the growth once the flux has completely melted. This improvement decreases the time and effort needed to heat and cool the furnace while melting the flux.

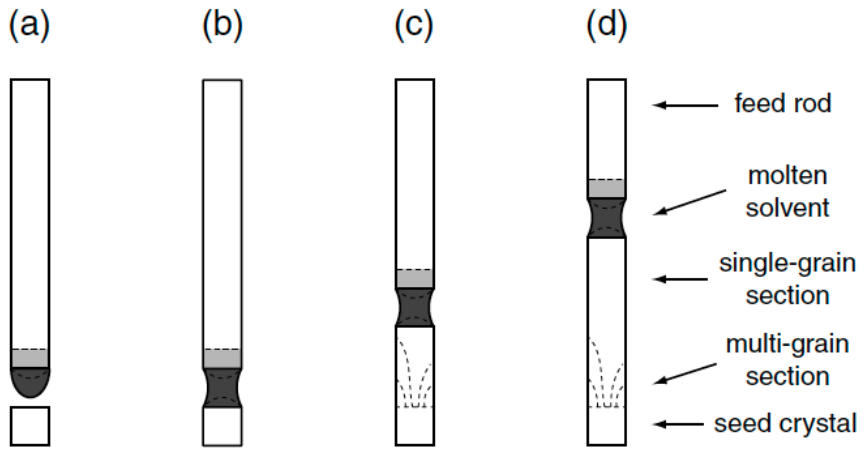

Figure 2.5: Illustration of the TSFZ growth, reproduced from [78].

The TSFZ growth progression is illustrated in Figure 2.5. During the growth, the upper and lower shafts counter-rotate to eliminate the azimuthal temperature gradient of the furnace. As the mirror stage moves upward, the bottom part of the feed rod slowly dissolves into a molten zone, and crystallites freeze out at the bottom. At the beginning of a growth, there are usually multiple crystal grains. Once one grain becomes larger than others, it will eventually dominate the growth to form a singe-grain crystal. There are multiple factors that can affect the quality of the growth: lamp power level, growth rate, growth atmosphere, gas pressure, etc.

The power level directly controls the temperature of the molten zone, which cannot be measured directly though, as it depends on the crystal size and melt composition. The growth must be periodically monitored to ensure that the right lamp power is used. If the power level is too high, the molten zone will drop. Once the feed rod dissolving rate is smaller than the seed rod depositing rate, the solvent will narrow, eventually causing the feed and seed rods to detach if no action is taken. On the other hand, if the power level is too low, part of the solvent will remain solid and cause the feed and seed rods to "knock" at each other and, eventually, to detach.

The growth rate also affects the crystal quality. High growth rates cause the crystals to remain multi-grain. Single-grain crystals are more likely to form with a low growth rate. However, growth with a low growth rate is more time consuming, and for materials with small surface tension, it is impossible to keep the growth at a small rate. For LSCO crystals with a diameter of ~ 5 mm, the growth rate is optimized at 0.5 mm/h.

High O_2 partial pressure is needed to suppress CuO evaporation during the growth of LSCO. This is achieved by containing the growth within a thick-wall quartz tube to maintain pressure, using an Ar/O_2 mixture for continuous gas flow. The melting point of the solvent increases with pressure. If the pressure is too high, the melting point becomes larger than the deposition point, and thus the growth is not feasible. For LSCO, the optimized pressure is around 2 atm with a 1:3 flow ratio of Ar:O_2 (50 cc/min of Ar and 150 cc/min of O_2).

The TSFZ-grown LSCO crystals are black and have shiny surfaces. Their typical size is 4-5 mm in diameter and more than 8 cm in length. Figure 2.4b shows an as-grown LSCO ($x = 0.02$) crystal grown with the TSFZ technique. After the crystals are grown, they are usually annealed at high temperature in an atmosphere that depends on the Sr doping level. For $x \leq 0.05$, crystals are annealed in Ar flow at 800 °C for 20 hours to remove excess oxygen and thermal stress. For $0.05 < x \leq 0.16$, crystals are heated in air at 800 °C for 40 hours to remove thermal stress. For $x > 0.16$, 900 °C in oxygen flow for 100 hours is used in order to recover oxygen deficiency and remove thermal stress.

2.1.2 Flux Growth of Hg1201 and Hg1212

This Thesis also involves the study of Hg-based cuprates. The Hg-family of compounds, whose formula reads as $HgBa_2Ca_{n-1}Cu_nO_{2n+2+\delta}$, where n is the number of CuO_2 layers per primitive cell, features a simple tetragonal symmetry. Moreover, it exhibits the record value of T_c for each n, and the record of $T_c = 134$ K ($n = 3$) at ambient pressure for all known materials to date [79]. The growth of single crystals requires relatively high Hg and O partial pressures [80] and is not feasible with the TSFZ method described above. Previous members of our research group have developed a two-step method to grow single-layer ($n = 1$) $HgBa_2CuO_{4+\delta}$ (Hg1201) single crystals [81]. Recently, double-layer ($n = 2$) $HgBa_2CaCu_2O_{6+\delta}$ (Hg1212) and triple-layer ($n = 3$) $HgBa_2Ca_2Cu_3O_{8+\delta}$ (Hg1223) crystals have also been obtained using a similar method [72].

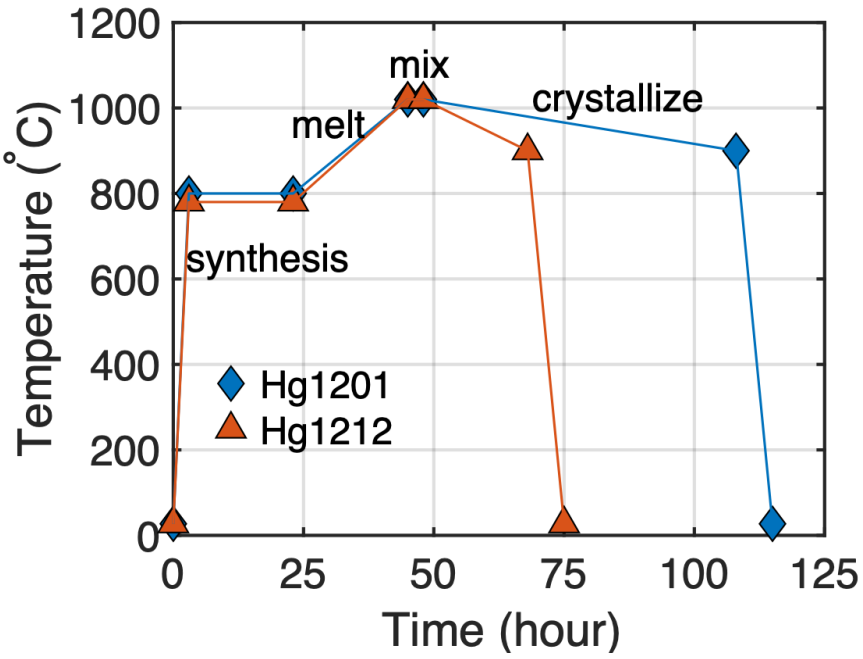

Figure 2.6: Temperature profiles for the Hg1201 and Hg1212 crystal growth.

The two-step growth includes an initial precursor preparation step and a subsequent high-temperature synthesis step. The purpose of the precursor step is to increase sample homogeneity, and also to reduce contamination from air and water. To prepare the precursor, stoichiometric powders of 99.99% $Ba(NO_3)_2$ and CuO_2 are weighted and mixed using a mortar and pestle. The mixture is then placed into a zirconia crucible and heated at 920 °C for 12 hours with oxygen flow at a rate of 4 L/min. $Ba(NO_3)_2$ decomposes into BaO and NO_2 at high temperature, with the latter being flushed away by oxygen flow. The $Ba_2Cu_nO_{2+n}$ precursor is formed following:

$$2 \cdot Ba(NO_3)_2 + n \cdot CuO \rightarrow Ba_2Cu_nO_{2+n} + 4 \cdot NO_2 + O_2. \tag{2.2}$$

The $Ba_2Cu_nO_{2+n}$ precursor is then ground and placed inside a zirconia crucible with an excess amount of HgO powder at the bottom. For the growth of Hg1212, an excess amount (30% more than the stoichiometric amount) of CaO powder is mixed with the precursor powders using a mortar and pestle. This process is performed in

a N_2 atmosphere glove box to avoid H_2O and CO_2 contamination, and also to reduce exposure to toxic HgO powders. The crucible is sealed inside an evacuated quartz tube with a small amount (20-30 mg) of $MgSO_4$ hydrate crystals, which introduce water to the reaction to facilitate the crystal nucleation. The sealed quartz tube is then placed in a furnace, heated to 1020 °C, and then slowly cooled. The cooling rate used for the crystallization was 2 °C per hour for Hg1201 and 6 °C per hour for Hg1212, as shown in Figure 2.6. The faster rate was chosen for Hg1212 in order to suppress the formation of the single-layer phase. The best Hg1212 crystals grown in this manner have a size of 1-2 mm along the CuO_2 planae, and a thickness around 0.1 mm. One such as-grown Hg1212 crystal is shown in Figure 2.7. The chemical reaction for the synthesis can be expressed as:

$$Ba_2Cu_nO_{2+n} + (n-1)\cdot CaO + HgO + \frac{\delta}{2}O_2 \rightarrow HgBa_2Ca_{n-1}Cu_nO_{2n+2+\delta}. \qquad (2.3)$$

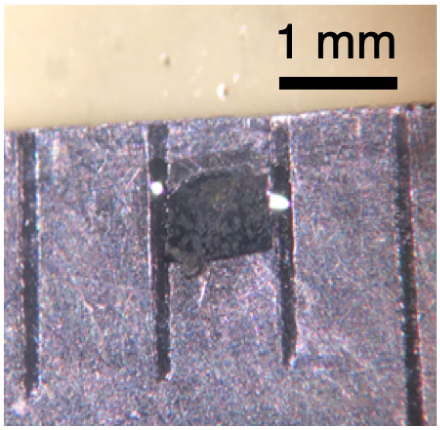

Figure 2.7: Picture of an as-grown Hg1212 crystal.

A problem with this growth method is that the high pressure generated by the excess HgO at high temperatures may cause explosions of the quartz tube. For the growth of Hg1201, where 30% of excess HgO is sufficient, the explosion rate can be kept below 10%. However, much higher Hg partial pressure is required to grow Hg1212 (and Hg1223) single crystals. The pressure generated during the Hg1212 growth, where 60% of excess HgO is added, is close to the stability limit of the quartz tubes, causing an explosion rate as high as 50%. This precludes the synthesis of Hg1223 single crystals

using this method, as this would require even larger pressures. A more advanced two-layer encapsulation method that utilizes custom-built high-pressure furnaces to grow larger Hg1212 and Hg1223 single crystals was reported in [72].

Anneal Condition	Final T_c (K)
300 °C, 6 bar O_2	92 (OV)
300 °C, O_2 flow	95 (OP)
450 °C, air	80 (UD)
480 °C, N_2 flow	71 (UD)
500 °C, air	65 (UD)
500 °C, 3 mTorr vacuum	55 or lower (UD)

Table 2.1: Anneal conditions for Hg1201 crystals, reproduced from [82]. OV: overdoped; OP: (nearly) optimally-doped; UD: underdoped.

As-grown Hg1201 and Hg1212 crystals are usually underdoped, with T_c values of about 80 K and 90 K, respectively. In order to obtain the desired hole content and to increase the doping homogeneity, as-grown crystals are subjected to a subsequent anneal processes at various temperatures and in different atmospheres (e.g., air, O_2, Ar, vacuum; see Table 2.1). The anneal time ranges from a week to several months, depending on the crystal size and target T_c.

2.2 Sample Characterization

In this Section, I discuss various in-house sample characterization techniques used to determine basic structural and magnetic properties of the crystals. X-ray Laue diffraction is routinely used to determine the crystal orientation. SQUID magnetometry measurements are performed to check the magnetic properties, especially to determine the Néel temperature (T_N) and superconducting critical temperature (T_c).

2.2.1 Laue Diffraction

Laue diffraction is named after Max von Laue, who was the first to study crystal structure using X-ray diffraction [83]. Unlike the monochromatic beam that is widely used in modern scattering techniques, Laue diffraction uses a white X-ray beam that consists of

a continuous range of photon energies. The photon energy ($\hbar\omega$) is related to its wavelength (λ) via $\hbar\omega = \frac{hc}{\lambda} = \frac{1.24\times10^4\text{eV}\cdot\text{Å}}{\lambda}$, where c is the speed of light. Instead of carefully tuning the scattering angle θ to satisfy Bragg's law ($2d\sin\theta = n\lambda$, where n is an integer, d is the lattice spacing, and θ is the scattering angle), Laue diffraction utilizes the full scattering angle and satisfies Bragg's law via a broad spectrum of λ. Because X-rays with a wide range of energies are generated simultaneously, Laue diffraction thus has the advantage of providing an immediate measurement of the crystal structure, and thus is routinely used for sample alignment prior to experiments at synchrotron facilities.

Due to the relatively low X-ray penetration depth (on the order of a few μm for typical $\sim$ 10 keV in-house X-rays), the backscattering geometry is usually used in Laue diffraction. That is, the photons are emitted from the X-ray source (typical in-house sources are X-ray tubes and rotating anodes), scattered by the crystal, and then detected by an area detector on the same side as the incident beam. The sample is mounted on a goniometer that has two rotational degrees of freedom, and the goniometer is then placed on a sample stage that can be moved translationally (x, y and z axes). Once the crystal structure is known from powder diffraction measurements, the crystal orientation can be theoretically calculated based on an arbitrary pattern. In practice, some synchrotron beamlines have limited scattering angle accesses, and it is desirable to polish the crystal surface along high symmetry axes (i.e., ab or ac planes) based on experimental needs. For the Hg-familiy of cuprates, this is easy to achieve, as as-grown crystals have shiny ab-plane surfaces. Figure 2.8 shows the Laue pattern for a Hg1201 UD70 crystal (the sample studied in Chapter 3). For TSFZ-grown LSCO, the c-axis is usually nearly perpendicular to the growth direction (i.e., perpendicular to the cylinder axis), and therefore sample alignment is straightforward as well.

2.2.2 SQUID Magnetometry

The temperature-doping phase diagram of the cuprates spans from the antiferromagnetic Mott-insulating state at zero doping, to the superconducting state at intermediate doping, to the non-superconducting over-doped regime (Figure 1.4). The Néel temperature (T_N) of antiferromagnetic samples and the superconducting transition temperature (T_c) of superconducting samples are two important defining characteristics. The simplest method to determine T_N and T_c is to measure the magnetic response of a sample

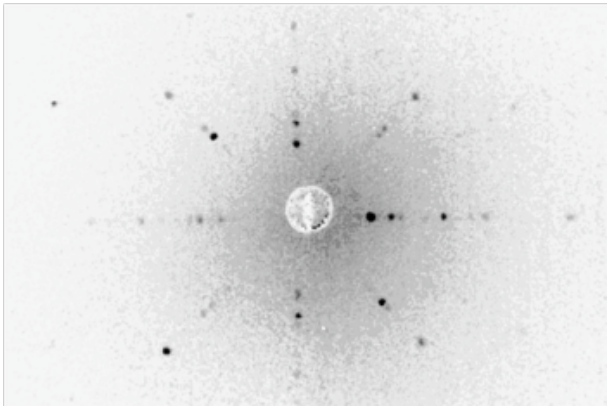

Figure 2.8: X-ray Laue diffraction pattern for a Hg1201 crystal (UD70) studied in Chapter 3. The incident X-rays were along the crystalline c-axis (i.e., [001]) and the horizontal/vertical directions correspond to the (100) axes. The bright and clear Bragg peaks in the pattern indicate good sample quality. The four-fold nature of the pattern implies tetragonal symmetry ($a = b$) of the lattice.

to an applied magnetic field.

Our laboratory uses a commercial MPMS XL magnetometer developed by Quantum Design, Inc. The MPMS system involves superconducting quantum interference devices (SQUIDs). A SQUID is a superconducting loop, connected by two parallel Josephson junctions, that is used to measure magnetic flux. In practice, in order to eliminate the flux of the applied external magnetic field, two or more SQUIDs are oppositely positioned above and below the sample. The magnetic flux produced by the sample can then be determined from the flux difference through the loops.

Once the temperature and magnetic field are set, SQUID measurements are performed through a sample position scan. If the sample size is small enough compared to the distance between oppositely positioned loops, the position scan can be modeled using an ideal dipole moment. By fitting the signal to a predefined line shape, the magnetic moment is determined from the fitted amplitude.

In general, probes such as nuclear magnetic resonance (NMR) and neutron scattering are widely used to determine the magnetic properties of materials. In the case of the antiferromagnetic insulator La_2CuO_4, neighboring magnetic moments align antiparallel to each other. Due to the staggered nature of the arrangement, one might not expect a SQUID magnetization measurements to be sensitive to the magnetic order.

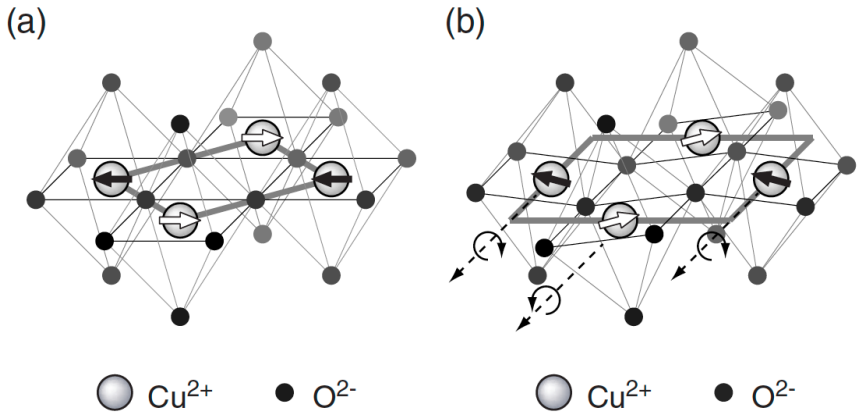

Figure 2.9: Copper-oxygen octahedra of LSCO in the (a) high-temperature tetragonal (HTT) and (b) long-range distorted low-temperature orthorhombic (LTO) phases, reproduced from [78]. The octahedra rotate in a staggered fashion about the [110] axis. The directions of the Cu^{2+} spin-1/2 magnetic moments of undoped La_2CuO_4 ($x = 0$) are indicated by black and white arrows.

However, when a strong magnetic field is applied perpendicular to the CuO_2 planes, the magnetic susceptibility peaks at $T_N = 325$ K (for $x = 0$), indicative of a transition. This anomalous behavior can be explained by the spin-canting in the buckled CuO_2 plane [84]. The LSCO system undergoes a structural phase transition from high-temperature tetragonal (HTT) to low-temperature orthorhombic (LTO) upon cooling (T_s is 530 K for $x = 0$ and decreases approximately linearly with doping to $T_s \approx 0$ at $x \approx 0.22$). As shown in Figure 2.9, the LTO phase introduces a staggered rotation of the oxygen octahedra. This causes the copper magnetic moments to cant, giving rise a non-zero net magnetic moment of each CuO_2 sheet. These weak ferromagnetic moments in turn are staggered along [001]. Application of a c-axis magnetic field causes the non-zero net moments to align along the field direction, giving rise to a cusp in the uniform susceptibility at T_N.

In the case of superconductors, the samples become perfect diamagnets below T_c, so that any small positive external magnetic field will give a large negative signal (the so-called Meissner-Ochsenfeld effect). Above T_c, in the normal state, the samples are paramagnetic with a relative weak net positive response. In practice, a sample is first cooled in zero magnetic field and the magnetic moment is measured as a function of

temperature upon heating in a small field (zero-field cooling, or ZFC). The measurement is then repeated on cooling in a field of the same magnitude (field cooling, or FC). The ZFC signal results from the full Meissner-Ochsenfeld effect, which is usually larger than the FC signal, since in the latter case some magnetic flux is pinned by impurities or defects. The ratio between FC and ZFC signals below T_c is an indication of the amount of disorder in the sample. A large FC/ZFC indicates that the sample is of high quality. In the case of $HgBa_2CuO_{4+\delta}$, a ratio of nearly 100% was observed [85]. For LSCO, values in the 10-20% range are typical.

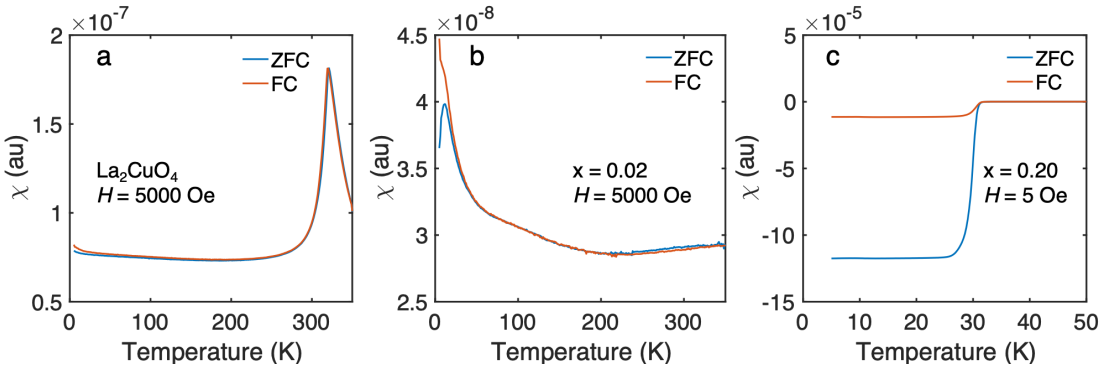

Figure 2.10: Representative SQUID magnetization measurements of LSCO. (a) Néel transition in the antiferromagnetic parent compound La_2CuO_4. (b) Spin-glass state in lightly-doped LSCO ($x = 0.02$). (c) Overdoped superconducting LSCO ($x = 0.20$). Blue and red curves represent zero-field-cool (ZFC) and field-cool (FC) measurements. The magnitude of the applied c-axis DC magnetic field is indicated in each panel.

Figure 2.10 shows representative measurements of the magnetic susceptibility of LSCO, for $x = 0$ (parent compound), $x = 0.02$ (underdoped), and $x = 0.20$ (overdoped). The cusp for undoped La_2CuO_4 in Figure 2.10a indicates the antiferromagnetic (Néel) transition around $T_N = 320$ K [86]. The susceptibility of the $x = 0.02$ sample exhibits a difference between ZFC and FC measurements indicative of a spin-glass state at low temperature [87]. The $x = 0.20$ sample is superconducting, as seen from the sharp transition around $T_c = 30$ K.

2.3 Synchrotron X-ray Scattering

Photon-based probes provide deep insight into the electronic properties of materials because photons directly interact with electrons. Synchrotron X-ray facilities are important photon sources for scattering and spectroscopy studies. A synchrotron facility accelerates electrons close to the speed of light using accelerators, stores the relativistic electrons in a storage ring, and produces X-ray photon radiation by changing the motion of (accelerating) the electrons. Compared to photons generated with traditional methods, synchrotron X-rays have much higher brilliance (by a factor of $\sim 10^{12}$) and penetrating power. In addition, the tunability of the photon energy and polarization enables adaptation to different experimental needs.

In this Thesis, inelastic X-ray scattering is the main technique used in the study of the cuprates (Chapters 3, 4, and 5). Depending on the energy of incident photons, one distinguishes between non-resonant inelastic X-ray scattering (IXS) and resonant inelastic X-ray scattering (RIXS). IXS is widely used to measure low-energy excitations, such as phonons, whereas in RIXS experiments, the cross section is enhanced by a resonant process, enabling the detection of otherwise unobservable excitations. In Chapter 6, X-ray absorption spectroscopy (XAS) and X-ray magnetic circular dichroism (XMCD) are employed to directly measure the electronic and magnetic structure around the Fermi level in $La_{1-x}Sr_xCoO_{3-\delta}$. Below, I first discuss basic scattering principles, and then give brief introductions to IXS and RIXS. XAS/XMCD is essentially the first step of the RIXS process, and thus not further discussed here.

2.3.1 Scattering Basics

A basic scattering schematic is shown in Figure 2.11. An incident photon with energy $\hbar\omega_i$, momentum $\hbar\mathbf{k}_i$, and polarization ϵ_i is scattered by a sample. The emitted photon has final energy $\hbar\omega_f$, momentum $\hbar\mathbf{k}_f$, and polarization ϵ_f. The momentum and energy conservation laws require:

$$\hbar\omega = \hbar\omega_i - \hbar\omega_f \tag{2.4a}$$

$$\boldsymbol{Q} = \hbar\mathbf{k}_i - \hbar\mathbf{k}_f \tag{2.4b}$$

Here $\hbar\omega$ and $\boldsymbol{Q}$ are the energy and momentum transferred to the sample. The

momentum transfer $\boldsymbol{Q}$ is a three-dimensional vector in reciprocal space, usually defined as $\boldsymbol{Q} \equiv H\mathbf{a}^* + K\mathbf{b}^* + L\mathbf{c}^* \equiv (H, K, L)$, where $a^* = \frac{2\pi}{a}$, $b^* = \frac{2\pi}{b}$ and $c^* = \frac{2\pi}{c}$ are reciprocal lattice constants. Because a crystal features a periodic lattice, the reduced wavevector $\boldsymbol{q}$ is usually used to describe excitations in a single Brillouin zone: $\boldsymbol{q} \equiv \boldsymbol{Q} - \boldsymbol{G}$, where $\boldsymbol{G}$ is a reciprocal lattice vector closest to $\boldsymbol{Q}$. Bragg reflections correspond to coherent elastic scattering (zero energy transfer and zero reduced momentum: $\hbar\omega = 0$ and $\boldsymbol{q} = 0$). In the case of the cuprates, which are lamellar, quasi-two-dimensional materials with CuO_2 sheets, the electronic properties are only weakly L-dependent. Thus, one often simply considers the two-dimensional vectors (H, K) and (h, k).

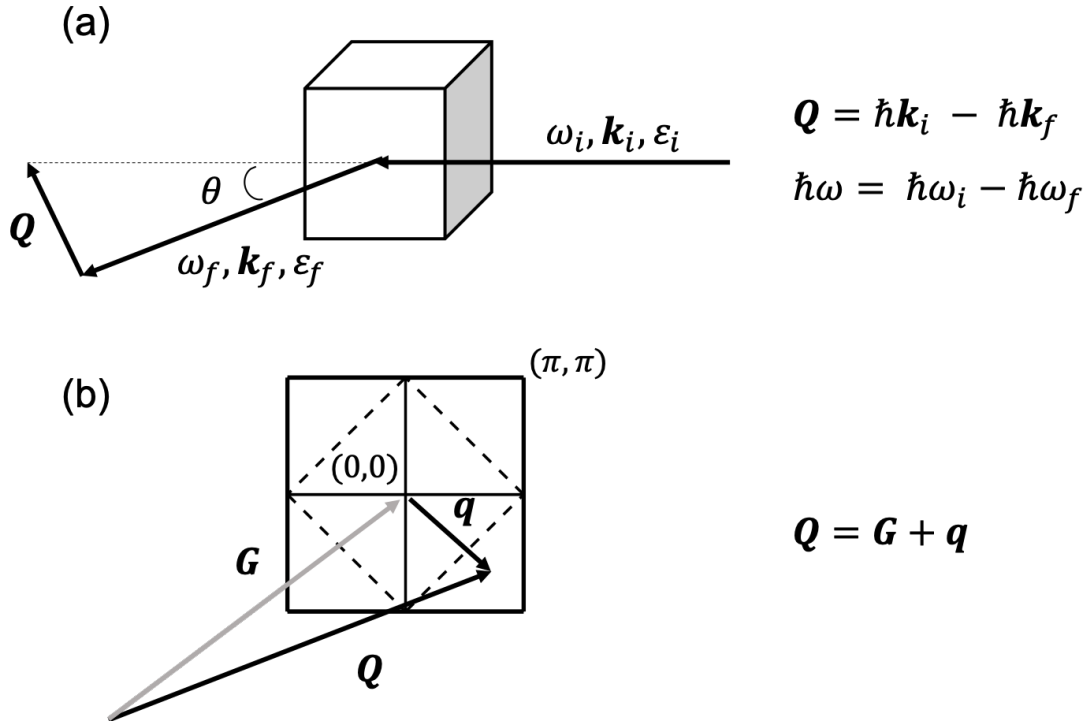

Figure 2.11: Basic scattering principles. (a) Scattering process. Photons are characterized by their energy $\hbar\omega$, momentum $\hbar\boldsymbol{k}$, and polarization $\boldsymbol{\epsilon}$. The subscripts i and f indicate incident and final-state (scattered) photons, respectively. The photon energy and momentum differences, $\hbar\omega = \hbar\omega_i - \hbar\omega_f$ and $\boldsymbol{Q} = \hbar\boldsymbol{k}_i - \hbar\boldsymbol{k}_f$, are transferred to the sample. (b) Momentum transfer in reciprocal space. The solid and dashed lines indicate the two-dimensional lattice and antiferromagnetic Brillouin zones of the cuprates, respectively. The reduced wavevector $\boldsymbol{q}$ is defined via $\boldsymbol{Q} = \boldsymbol{G} + \boldsymbol{q}$, where $\boldsymbol{G}$ is the nearest reciprocal lattice vector.

The scattering process can be understood with the theory of quantum electrodynamics [88]. X-rays are usually described by an electromagnetic field with vector potential $\boldsymbol{A}(\boldsymbol{r})$, which can be expanded as plane waves:

$$\mathbf{A}(\mathbf{r}) = \sum_{\mathbf{k},\boldsymbol{\epsilon}} \sqrt{\frac{\hbar}{2V\epsilon_0\omega_{\mathbf{k}}}}\left(\boldsymbol{\epsilon} a_{\mathbf{k},\boldsymbol{\epsilon}} e^{i\mathbf{k}\cdot\mathbf{r}} + \boldsymbol{\epsilon}^* a^\dagger_{\mathbf{k},\boldsymbol{\epsilon}} e^{-i\mathbf{k}\cdot\mathbf{r}}\right), \tag{2.5}$$

where V is the volume of the system, ϵ_0 is the vacuum permittivity, and $a^\dagger_{\mathbf{k},\boldsymbol{\epsilon}}$ and $a_{\mathbf{k},\boldsymbol{\epsilon}}$ are creation and annihilation operators, respectively. The total Hamiltonian H of the system is split into a noninteracting term, H_0, and an interacting term, H_{int}:

$$H = H_0 + H_{int}. \tag{2.6}$$

H_0 involves the electron kinetic and potential energies, whereas H_{int} is the electron-photon interaction term. H_{int} is much smaller than H_0, and treated as a perturbation to H_0:

$$H_0 = \sum_j \frac{1}{2m}\mathbf{p}_j^2 + \sum_{jj'} V(\mathbf{r}_{jj'}) \tag{2.7a}$$

$$H_{int} = \sum_j -\frac{e}{mc}\mathbf{A}(\mathbf{r}_j)\cdot\mathbf{p}_j + \sum_j \frac{e^2}{2mc^2}\mathbf{A}^2(\mathbf{r}_j), \tag{2.7b}$$

where the sum runs over all the electrons j in the system, $\mathbf{p}_j$ is the electron momentum operator, m and e are the electron mass and charge, and c is the speed of light. The spin-dependent terms are neglected here, as they are smaller by a factor of $\frac{\hbar}{mc^2}$. The $\mathbf{A}\cdot\mathbf{p}$ term in Equation 2.7b is the photoelectric process, which entails different phenomena, such as photoemission and X-ray absorption spectroscopy to first-order of perturbation, and resonant inelastic X-ray scattering (RIXS) to second order of perturbation. The Coulomb gauge ($\nabla\cdot\mathbf{A} = 0$) is used in Equation 2.7b so that $\mathbf{p}\cdot\mathbf{A} = \mathbf{A}\cdot\mathbf{p}$.

The electron-photon interaction may excite the system from the ground state $|i\rangle$ to a final state $|f\rangle$ with energies E_i and E_f, respectively. This transition probability W is given by

$$W = \frac{2\pi}{\hbar}\left|\langle f|H_{int}|i\rangle + \sum_n \frac{\langle f|H_{int}|n\rangle\ \langle n|H_{int}|i\rangle}{E_n - E_i - \hbar\omega_i}\right|^2 \delta(E_f + \hbar\omega_f - E_i - \hbar\omega_i), \tag{2.8}$$

where $\hbar\omega_i$ and $\hbar\omega_f$ are the energies of the incident and scattered photons, and $|n\rangle$ denotes the intermediate state with energy E_n. The first term corresponds to Fermi's golden rule. The first-order term is usually much larger than the second-order term, which yields regular non-resonant scattering. When the energy of incident X-rays is tuned to a specific transition ($\hbar\omega_i = E_n - E_i$), the second term dominates, giving rise to resonant X-ray scattering.

A general concept in scattering is the scattering cross section σ, which corresponds the total number of scattered particles $\Phi\sigma$ per time unit, where Φ is the incident particle flux. The double-differential scattering cross section $\frac{\mathrm{d}\sigma}{\mathrm{d}\Omega\mathrm{d}\omega_f}$ specifies particles scattered into the solid angle $\mathrm{d}\Omega$ with final energy $\mathrm{d}\omega_f$. $\frac{\mathrm{d}\sigma}{\mathrm{d}\Omega\mathrm{d}\omega_f}$ is proportional to the transition probability W:

$$\frac{\mathrm{d}^2\sigma}{\mathrm{d}\Omega\mathrm{d}\omega_f} = \frac{W\rho(\hbar\omega_f)}{\Phi} = \frac{WV^2\omega_f^2}{8\pi^3\hbar c^4}, \tag{2.9}$$

where $\rho(\hbar\omega_f) = \frac{V\omega_f^2}{8\pi^3\hbar c^3}$ is the density of final photon states and $\Phi = \frac{c}{V}$ is the incident particle flux [89].

In order to calculate the double-differential scattering cross section, it is useful to classify H_{int} by powers of $\mathbf{A}$. To first order, only the terms to order $\mathbf{A}^2$ are taken into account, because they contain contributions proportional to $a^\dagger_{\mathbf{k}'\epsilon'}a_{\mathbf{k}\epsilon}$ and $a_{\mathbf{k}\epsilon}a^\dagger_{\mathbf{k}'\epsilon'}$. This includes the second term in H_{int} that accounts for non-resonant X-ray scattering. Although the interaction term linear in $\mathbf{A}$ (the first term in H_{int}) does not contribute to first order, its square contributes to the second order, yielding resonant X-ray scattering. The double-differential scattering cross section $\frac{\mathrm{d}^2\sigma}{\mathrm{d}\Omega\mathrm{d}\omega_f}$ derived from the interaction Hamiltonian to the second order is known as Kramers-Heisenberg formula [90], and it is discussed in more detail in the following Sections.

2.3.2 Non-Resonant Inelastic X-ray Scattering

Cross Section

To the first-order of perturbation, when the incident photon energy $\hbar\omega_i$ is far from the

resonant energy $(E_n - E_i)$, $\frac{\mathrm{d}^2\sigma}{\mathrm{d}\Omega\mathrm{d}\omega_f}$ in IXS arises from the $\mathbf{A}^2$ term in H_{int} and reads as:

$$\frac{\mathrm{d}^2\sigma}{\mathrm{d}\Omega\mathrm{d}\omega_f} = \frac{\omega_f}{\omega_i}\big(\frac{e^2}{mc^2}\big)^2\big(\epsilon_i \cdot \epsilon_f^*\big)^2 \sum_f \left| \langle f|\sum_j \exp\big(\mathrm{i}\mathbf{q}\cdot\mathbf{r}_j\big)|i\rangle \right|^2 \times \delta\big(E_f - E_i - \hbar\omega\big), \quad (2.10)$$

We introduce free-electron Thomson scattering,

$$\big(\frac{\mathrm{d}\sigma}{\mathrm{d}\Omega}\big)_{Th} = \frac{e^2}{mc^2}\big(\frac{\omega_f}{\omega_i}\big)\big|\epsilon_i \cdot \epsilon_f^*\big|^2, \quad (2.11)$$

and the dynamical structure factor,

$$S\big(\mathbf{q},\omega\big) = \sum_f \left| \langle f|\sum_j \exp\big(\mathrm{i}\mathbf{q}\cdot\mathbf{r}_j\big)|i\rangle \right|^2 \delta\big(E_f - E_i - \hbar\omega\big), \quad (2.12)$$

to simplify the IXS cross section:

$$\frac{\mathrm{d}^2\sigma}{\mathrm{d}\Omega\mathrm{d}\omega_f} = \big(\frac{\mathrm{d}\sigma}{\mathrm{d}\Omega}\big)_{Th} S\big(\mathbf{q},\omega\big). \quad (2.13)$$

Thomson scattering describes the scattering cross section of a free electron. In the scattering from a crystal with zero energy transfer ($\hbar\omega = 0$), Thomson scattering contributes along with the static structure factor $S\big(\mathbf{q},\omega = 0\big)$, giving rise to Bragg scattering. In the adiabatic approximation, $\frac{\mathrm{d}^2\sigma}{\mathrm{d}\Omega\mathrm{d}\omega_f}$ can be factorized as:

$$\frac{\mathrm{d}^2\sigma}{\mathrm{d}\Omega\mathrm{d}\omega_f} = \big(\frac{\mathrm{d}\sigma}{\mathrm{d}\Omega}\big)_{Th}\big|f\big(\mathbf{q}\big)\big|^2 S^*\big(\mathbf{q},\omega\big), \quad (2.14)$$

where $f(\mathbf{q})$ is the electronic form factor and $S^*\big(\mathbf{q},\omega\big)$ is the atomic contribution to the total dynamical structural factor. Equation 2.14 is widely used to model phonon excitations measured via IXS [91].

Dynamical Structure Factor

The dynamical structure factor $S(\mathbf{q},\omega)$ (Equation 2.12) describes all possible excitations from an initial state (E_i) to final states (E_f). According to van Hove [92], $S(\mathbf{q},\omega)$ can

also be expressed as the Fourier transform of the electron-pair correlation function:

$$S\big(\mathbf{q},\omega\big) = \frac{1}{2\pi}\int_{-\infty}^{\infty} \mathrm{d}t e^{-i\omega t}\,\langle i|\sum_{jj'} e^{-i\mathbf{q}\cdot\mathbf{r}_{j'}(t)} e^{i\mathbf{q}\cdot\mathbf{r}_{j}(0)}|i\rangle\,, \tag{2.15}$$

where $|i\rangle$ is the initial state of the system, and $\mathbf{r}_j(0)$ and $\mathbf{r}_{j'}(t)$ are the positions of electron pairs at times zero and t. The equivalence between Equations 2.12 and 2.15 is a manifestation of the fluctuation-dissipation theorem: the excitations of the system (dissipation) are connected to the scattering due to density fluctuations in the initial state. Using the fluctuation-dissipation theorem, the dynamical structure factor is related to the imaginary part of electronic polarization function $\chi(\mathbf{q},\omega)$:

$$S\big(\mathbf{q},\omega\big) = -\frac{1}{\pi}(1+n_B)\mathrm{Im}\big[\chi\big(\mathbf{q},\omega\big)\big], \tag{2.16}$$

where $n_B = 1/[\exp(\hbar\omega/k_BT) - 1]$ is the Bose factor.

IXS provides information about charge-density fluctuations of the electronic system. In the case of a homogeneous electron system, $S(\mathbf{q},\omega)$ can be further expressed as a function of the macroscopic dielectric function $\epsilon(\mathbf{q},\omega)$, which is the ratio of the electric displacement field $\mathbf{D}$ to the applied electric field $\mathbf{E}$:

$$S(\mathbf{q},\omega) = (1+n_B)\frac{q^2}{4\pi^2e^2}\mathrm{Im}\big[\frac{-1}{\epsilon(\mathbf{q},\omega)}\big] \tag{2.17}$$

This is similar to the cross section in the case of electron energy loss spectroscopy (EELS) [93].

2.3.3 Resonant Inelastic X-ray Scattering

The second term in Equation 2.8 becomes large when the incident photon energy matches the resonant condition, $\hbar\omega_i = E_n - E_i$. The denominator $E_n - E_i - \hbar\omega_i$ is then small, which greatly enhances the cross-section. Removing unimportant factors and neglecting the contributions of the first- and third-order terms, we can obtain the

resonantly-enhanced large RIXS cross section [94]:

$$I(\omega_i, \omega_f, \mathbf{k}_i, \mathbf{k}_f) = \sum_f \left| \sum_n \frac{\langle f|T_f|n\rangle \ \langle n|T_i|i\rangle}{E_n - E_i - \hbar\omega_i + i\Gamma_n} \right|^2 \delta\big(E_f + \hbar\omega_f - E_i - \hbar\omega_i\big), \qquad (2.18)$$

where $T_i = \epsilon_i \cdot \sum_j \mathbf{p}_j e^{i\mathbf{k}_i \cdot \mathbf{r}_j}$ and $T_f = \epsilon_f^* \cdot \sum_j \mathbf{p}_j e^{i\mathbf{k}_f \cdot \mathbf{r}_j}$ represent the transition operators between the electrons and incident/emitted X-rays. Γ_n is introduced to account for the finite lifetime $\hbar/\Gamma_n$ of the intermediate state $|n\rangle$.

In the case of the cuprates, the incoming photon energy can be tuned to different resonant energies, i.e., copper K-, L-, M- or oxygen K-edges, where different incident phonon energies promote different types of core electrons into empty valence shells. The copper atoms in the CuO_2 sheet have a partially filled $3d$ valence shell and the electronic configuration of Cu^{2+} is $1s^2 2s^2 2p^6 3s^2 3p^6 3d^9$. At the Cu K-edge, $1s$ core electrons are excited to the $4p$ valence state, with an energy of about 9,000 eV that lies in the hard X-ray regime. In contrast, the $L_{2,3}$-edge $2p \rightarrow 3d$ ($\sim$ 900 meV) and $M_{2,3}$-edge $3p \rightarrow 3d$ ($\sim$ 80 eV) excitations are in the soft X-ray regime. One can also choose to excite the O atom by promoting a O $1s$ electron to an empty $2p$ valence state (O K-edge) with photon energy $\sim$ 500 eV.

In the RIXS process, the incident photon is first absorbed by a core electron that is promoted to an empty valence shell. This intermediate state is usually highly energetic and unstable because of the presence of the deep electronic core hole. The system then quickly decays from this intermediate state, typically within 1-2 fs. One of the possible decay processes is the Auger process, by which an electron fills the core hole while another electron is simultaneously emitted. The other common decay process is the so-called fluorescent decay: the core hole is filled by a valence electron and at the same time a photon is emitted.

There are two different RIXS mechanisms, namely *direct* and *indirect*. Figure 2.12 and Figure 2.13 represent these two different types of processes. The classification of RIXS as either *direct* or *indirect* is useful, as the two mechanisms have rather different cross sections. The details of *direct* and *indirect* RIXS are discussed briefly below, using Cu L-and K-edge scattering as examples. In general, when it is allowed, direct scattering is the dominant inelastic scattering channel. The indirect process usually

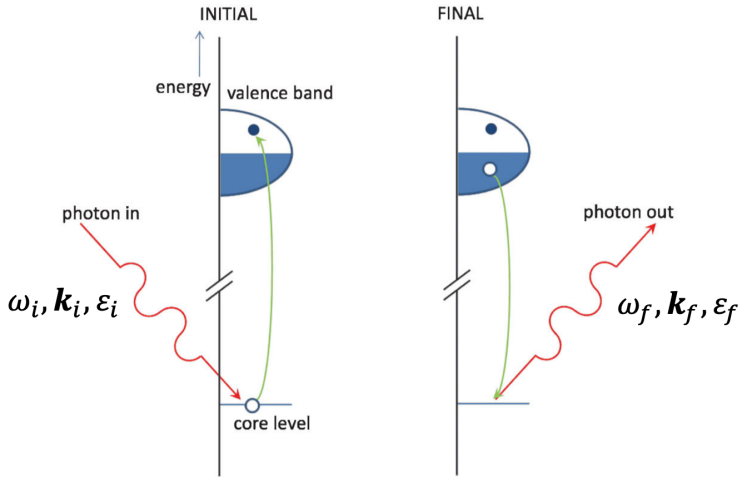

Figure 2.12: Direct RIXS process, adapted from [88]. A core-level electron absorbs energy from an incident photon and is promoted into an empty valence band state. The empty core hole is then filled by an electron from the occupied valence states, while a photon is emitted. This RIXS process creates a valence excitation with momentum $\hbar\mathbf{k}_i - \hbar\mathbf{k}_f$ and energy $\hbar\omega_i - \hbar\omega_f$.

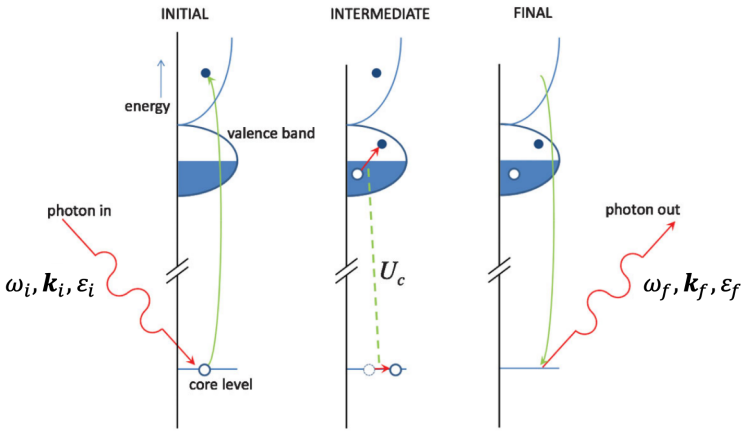

Figure 2.13: Indirect RIXS process, adapted from [88]. In indirect RIXS, an electron is excited from a deep-lying core level into the valence band. Additional charge excitations occur in the intermediate state through the Coulomb interaction U_c between the core hole and valence electrons. The final state then features an excitation in the valence band with momentum $\hbar\mathbf{k}_i - \hbar\mathbf{k}_f$ and energy $\hbar\omega_i - \hbar\omega_f$.

contributes only at higher order. However, for the large class of experiments for which direct scattering is forbidden, RIXS relies exclusively on indirect scattering channels [88].

The discussion of RIXS presented here follows the reviews [88] and [94], and the interested reader is encouraged to read the original articles for more details.

Cu L-edge RIXS

For direct RIXS, both the initial photoelectric transition from core to valence state and the succeeding decay from the conduction state to fill the core hole should be possible. Cu L-edge RIXS is a typical direct scattering process through $2p$ to $3d$ excitation and subsequent $3d$ to $2d$ decay. Since empty $3d$ states in the cuprates lie at the Fermi level, RIXS therefore directly probes the valence and conduction states.

Since the electrons in the $2p$ orbitals experience considerable spin-orbit coupling, the wave function at site i is usually represented by the total angular momentum J and its z component J_z: $|2p; JJ_z\rangle = \Psi_{2p,J,J_z}(\mathbf{r} - \mathbf{R}_i)$. In the case of the Cu L-edge, it is possible to tune the energy either to the L_2-edge ($J = 1/2$) or the L_3-edge ($J = 3/2$). The atomic wave function for the $3d$ orbital can be expressed as $|3d; \mu\sigma\rangle = \Psi_{3d,\mu\sigma}(\mathbf{r} - \mathbf{R}_i)$. Note that the wavelength of the incident photon is ~ 11.2 Å at the L-edge, so that we can take the dipole approximation limit $e^{i\mathbf{k}_i} \cdot (\mathbf{r} - \mathbf{R}_i) = 1$. The transition matrix element then becomes:

$$\begin{aligned} M_i =& \langle 3d; \mu\sigma | (\boldsymbol{\epsilon}_i \cdot \mathbf{p}) \mathrm{e}^{i\mathbf{k}_i \cdot \mathbf{r}} | 2p; JJ_z \rangle \\ =& \frac{i}{\hbar} (\epsilon_{3d,\mu\sigma} - \epsilon_{2p,J,J_z}) \mathrm{e}^{i\mathbf{k}_i \cdot \mathbf{R}_i} \langle 3d; \mu\sigma | \boldsymbol{\epsilon}_i \cdot \mathbf{r} | 2p; JJ_z \rangle \,, \end{aligned} \tag{2.19}$$

where $\epsilon_{3d,\mu}$ and ϵ_{2p,JJ_z} are $3d$ and $2p$ atomic energy levels. By introducing the $2p$ core hole creation operator $P^\dagger_{\mathbf{k},J,J_z}$ and the $3d$ electron creation operator $d^\dagger_{\mathbf{k},\mu,\sigma}$, summing over all sites, and removing unimportant factors, we can write the dipole operator as:

$$D^{L\dagger}_{i(f)} = \sum_{\mu,\sigma,J_z} c^{JJ_z}_{\mu\sigma}(\boldsymbol{\epsilon}_i) \sum_k d^\dagger_{\mathbf{k},\mu,\sigma} P^\dagger_{\mathbf{k}-\mathbf{k}_{i(f)},J,J_z}, \tag{2.20}$$

where the coefficient $c^{JJ_z}_{\mu\sigma}$ can be calculated using atomic wave functions:

$$c^{JJ_z}_{\mu\sigma}\left(\epsilon_i\right) = \langle 3d; \mu\sigma | \boldsymbol{\epsilon}_i \cdot \mathbf{r} | 2p; JJ_z \rangle \,. \tag{2.21}$$

Up to now, the Hamiltonian of the system with initial state $|i\rangle$, final state $|f\rangle$, and intermediate state $|n\rangle$ has not been introduced. There are several representative models that describe $3d$ electrons, including the one-band Hubbard model, the three-band Hubbard model ($d-p$ model), and the $t-J$ model. The Hamiltonians of these models give the energy states, *i.e.*, $H_{3d}\,|g\rangle = E_g\,|g\rangle$ for the ground state $|g\rangle$. In the Cu L-edge RIXS process, in addition to H_{3d}, the energy level of the $2p$ core hole, H_p, as well as the Coulomb interaction between the $2p$ core hole and $3d$ electrons, H_c, should also be considered in the intermediate state.

With the total Hamiltonian $H = H_{3d} + H_p + H_c$, the transition matrix element of Cu L-edge RIXS from the ground state $|g\rangle$ to the final state $|f\rangle$ reads

$$F_{gf}^{L} = \langle f|D_f^L \frac{1}{H - E_g - \hbar\omega_i + i\Gamma} D_i^{L^\dagger}|g\rangle\,. \tag{2.22}$$

Note that it is possible to excite a $2p$ electron to various spin components of $3d$ orbitals, and for the electron to return to the $2p$ orbital with opposite spin. The combination of the two dipole operators D_f^L and $D_i^{L^\dagger}$ in Equation 2.22 makes it possible to induce spin-flip excitations in the $3d$ electron system. Therefore, Cu L-edge RIXS can detect not only spin-conserved charge and magnetic excitations, but also spin-flip excitations. This renders Cu L-edge RIXS complementary to traditional neutron scattering for magnetic excitation measurements.

Cu K-edge RIXS

In the Cu K-edge RIXS process, a core level electron in the $1s$ orbital absorbs the energy of the incident photon and is excited to the $4p$ orbital. The intermediate state is energetic and highly unstable, causing the $3d$ electrons to interact with the $1s$ core hole and the photo-excited $4p$ electron through Coulomb interactions. The $4p$ electron then returns to the $1s$ orbital and a photon is simultaneously emitted. The energy and momentum differences between incident and emitted photons are thus transferred to the $3d$ band. Therefore, Cu K-edge RIXS is an indirect probe of $3d$ electrons.

The $4p$ electrons in the conduction band can be expressed as the Bloch state $|4p\rangle = \exp(i\mathbf{k}_0\cdot\mathbf{r})u_{\mu\mathbf{k}_0}(\mathbf{r})$, where $u_{\mu\mathbf{k}_0}$ is the periodic lattice function. The core level $1s$ electrons at site i can be expressed as the atomic wave function: $|\psi_{1s}\rangle = \psi_{1s}(\mathbf{r}-\mathbf{R}_i)$. The

transition-matrix element from the $1s$ orbital to the conduction band then reads as:

$$\begin{aligned} M_i &= \langle 4p|(\boldsymbol{\epsilon}_i \cdot \mathbf{p})\mathrm{e}^{i\mathbf{k}_i\mathbf{r}}|\psi_{1s}\rangle \\ &= \mathrm{e}^{-i\mathbf{k}_0\cdot\mathbf{R}_i}\mathrm{e}^{i\mathbf{k}_i\cdot\mathbf{R}_i} \times \int \mathrm{d}\mathbf{r}'\mathrm{e}^{-i\mathbf{k}_0\cdot\mathbf{r}'}u_{\mu\mathbf{k}_0}(\mathbf{r}')(\boldsymbol{\epsilon}_i \cdot \mathbf{p})\mathrm{e}^{i\mathbf{k}_i\cdot\mathbf{r}'}\psi_{1s}(\mathbf{r}'), \end{aligned} \tag{2.23}$$

where $\mathbf{r}' = \mathbf{r} - \mathbf{R}_i$. Given that the wavelength of the incident photon is ~ 1.4 Å at the Cu K-edge ($\hbar\omega_i \approx 9$ keV), much larger than the extent of the $1s$ wave function calculated as a_B/Z, with the Bohr radius a_B ($= 0.529$ Å) and the atomic number Z, we can take the dipole approximation, $\mathrm{e}^{i\mathbf{k}_i\cdot\mathbf{r}'} \approx 1$. On the other hand, the length scale of $\mathbf{k}_0$ is the lattice constant, so it is also safe to consider $\mathrm{e}^{i\mathbf{k}_0\cdot\mathbf{r}'} \approx 1$. Taking the dipole approximation, Equation 2.23 then becomes:

$$M_i = \mathrm{e}^{-i\left(\mathbf{k}_0-\mathbf{k}_i\right)\cdot\mathbf{R}_i}\boldsymbol{\epsilon}_i \cdot \mathbf{P}_{\mu,1s} \tag{2.24}$$

where

$$\mathbf{P}_{\mu,1s} = \langle u_{\mu\mathbf{k}_0}|\mathbf{p}|\psi_{1s}\rangle\,. \tag{2.25}$$

Let's introduce a creation operator of a $4p$ Bloch electron with spin σ: $p^\dagger_{\mathbf{k}_0,\sigma}$, and a creation operator of the $1s$ hole at site i: $S^\dagger_{i,\sigma}$. After summing M_i in Equation 2.24 over all sites, the K-edge dipole transition operator from the ground state $|g\rangle$ to the intermediate state $|n\rangle$, or from the intermediate state $|n\rangle$ to the final state $|f\rangle$ is:

$$D^{K\dagger}_{i(f),\sigma} = p^\dagger_{\mathbf{k}_0,\sigma}S^\dagger_{\mathbf{k}_0-\mathbf{k}_{i(f)},\sigma} \tag{2.26}$$

where

$$S^\dagger_{\mathbf{k},\sigma} = N^{-1/2}\sum_i S^\dagger_{i,\sigma}\exp(-i\mathbf{k}\cdot\mathbf{R}_i), \tag{2.27}$$

and N is the total number of sites.

Back to Equation 2.18, we obtain the Cu K-edge RIXS cross section for $1s \rightarrow 4p$ transitions:

$$\begin{aligned} I(\omega_i,\omega_f,\mathbf{k}_i,\mathbf{k}_f) = &\left|(\boldsymbol{\epsilon}^*_f \cdot \mathbf{P}_{4p,1s})(\boldsymbol{\epsilon}_i \cdot \mathbf{P}_{4p,1s})\right|^2 \\ &\sum_f \left|\sum_{n,\sigma}\frac{\langle f|D^K_{f,\sigma}|n\rangle\ \langle n|D^{K\dagger}_{i,\sigma}|g\rangle}{E_n - E_i - \hbar\omega_i + i\Gamma_n}\right|^2 \delta\big(E_f + \hbar\omega_f - E_i - \hbar\omega_i\big). \end{aligned} \tag{2.28}$$

Here, the momentum difference $\hbar\mathbf{k}_i - \hbar\mathbf{k}_f$ and energy difference $\hbar\omega_i - \hbar\omega_f$ are transferred to the final state $|f\rangle$, making RIXS a powerful probe for momentum- and energy-resolved measurements.

Similar to the considerations for the Cu L-edge, the total Hamiltonian of the system includes the energy of the $3d$ electrons, H_{3d}, $1s$-core hole, H_s, $4p$ electron, H_{4p}, and the Coulomb interaction between the $1s$-core hole, $4p$ electron, and $3d$ electrons, H_c. Note that the $4p$ electron is delocalized in the conduction band, so that the interactions related to the $4p$ electrons are usually neglected for simplicity. Thus, the dominant term in H_c is the attractive interaction between the $1s$-core hole and $3d$ electrons. With $H = H_{3d} + H_s + H_c$, it is then possible to calculate the K-edge RIXS intensity either numerically for finite-size lattice systems [94], or analytically via perturbative treatment [88].

Chapter 3

Dynamic Charge-Density-Wave Correlations in Hg1201

The temperature-doping phase diagram of the cuprates was briefly discussed in Chapter 1. Among the different ordering tendencies in the pseudogap part of the phase diagram, the charge-density-wave (CDW) instability in the underdoped cuprates, which tends to compete with the superconducting order, has been a major recent research focus. However, measurements of dynamic, energy-resolved CDW correlations are still in their infancy. In this Chapter, I present a systemic study of the dynamic charge correlations in the model cuprate $HgBa_2CuO_{4+\delta}$ (Hg1201, $T_c = 70$ K). Using RIXS with very high energy resolution (60 meV) and a new analysis method, dynamic charge correlations with characteristic scales of about 40 meV and 150-200 meV are revealed. The possible connection among these two charge scales, the magnetic excitations, and the superconducting glue function is discussed.

3.1 CDW Correlations in Cuprates

In the cuprates, superconductivity emerges upon modifying of the chemical composition via chemical substitution or the introduction of excess oxygen. The dome-shaped superconducting phase (Figure 1.4) can be approximately described by a parabola: $\frac{T_c}{T_c^{max}} = 1 - 82.6(x - 0.16)^2$, where the maximum transition temperature T_c is reached at the optimal hole doping level $x \approx 16\%$ [95]. It is not clear why superconductivity is

weakened as the doping concentration deviates from this optimal value. One possibility is the presence of a coexisting order which competes with superconductivity in the underdoped regime [7, 96].

The CDW in the cuprates exhibits a periodic, incommensurate modulation of charge along the Cu-O bond direction. Initial evidence for charge order came in 1995, from neutron scattering work on $La_{1.48}Nd_{0.4}Sr_{0.12}CuO_4$, where a superstructure peak indicative of a four-unit-cell periodic spatial charge modulation was observed through the associated lattice distortion [97]. Approximately a decade later, quantum-oscillation [98] and Hall-effect [98,99] measurements of Y-based cuprates hinted at Fermi-surface reconstruction under high magnetic fields. A natural origin of the reconstruction is band-folding induced by an ordered state. Therefore, these experiments are indirect evidence for the presence of CDW oder in the underdoped cuprates. Further evidence for CDW correlations came from STM work (in the absence of an applied magnetic field) of $(Bi,Pb)_2(Sr,Ca)_2CuO_{6+\delta}$ [100] and NMR measurements of $YBa_2Cu_3O_{6+\delta}$ (YBCO) in high magnetic fields [101].

More recently, X-ray scattering experiments, which are directly sensitive to charge order, revealed incommensurate CDW correlations in various cuprate materials [20, 21, 69, 70, 102–114], including our group's contributions for $HgBa_2CuO_{4+\delta}$ (Hg1201) [69, 106], $HgBa_2CaCu_2O_{6+\delta}$ (Hg1212) [71], and $Nd_{2-x}Ce_xCuO_4$ (NCCO) [21, 70]. The CDW is generally seen to have a reduced wave vector in the $q_{CDW} \sim 0.25 - 0.33$ rlu range, which corresponds to a spatial modulation of 3-4 lattice constants. The CDW intensity and correlation length are often found to decrease in the superconducting state, and therefore it is thought that the CDW competes with superconductivity [102]. This conclusion is supported by the observed enhancement of the CDW intensity when the superconductivity is suppressed by a magnetic field in YBCO [103, 104, 111]. Whereas initial measurements focused on underdoped compounds, similar behavior has recently been observed in optimally-doped samples [109,112] and in one overdoped cuprate [114].

However, key questions remain unresolved. The mechanism of CDW formation could be related to Fermi-surface nesting (i.e., a reciprocal-space mechanism) [115,116], or to strong electronic correlations that lead to charge separation (i.e., a real-space mechanism) [97, 117]. Furthermore, the relation between CDW correlations and the pseudogap is far from understood, with suggestions that either one is the underlying

phenomenon [113,118–121]. Finally, the short correlation lengths indicate that disorder might play an important role, but it is still unknown how the CDW in the cuprates becomes static on cooling and what the pinning mechanism is.

3.2 Previous CDW Measurements in Hg-based cuprates

Hg1201 is a single-layer compound, with a simple tetragonal crystal structure and an optimal T_c of nearly 100 K [85,120,122–132]. The model nature of Hg1201 is exemplified, e.g., by the observations that the normal-state magnetoresistance in the pseudogap state exhibits Kohler scaling [127] and low-temperature transport measurements reveal Shubnikov-de-Haas oscillations due to Fermi-surface reconstruction associated with the CDW order [125, 130]. Therefore, Hg1201 is perhaps the most ideal cuprate to study CDW correlations and related phenomena. In 2014 [106] and 2017 [69], we published our initial findings for Hg1201, using RXS. Recently, we extended our RXS work to the CDW correlations in Hg1212, the double-layer sister compound of Hg1201 [71].

3.2.1 CDW Temperature Dependence

As described in Chapter 2, resonant X-ray scattering, whereby the incident photon energy is tuned to the Cu L_3 edge to enhance the scattering cross-section, is a direct probe of CDW correlations. The scattered photons can be directly measured in energy-integrated mode (conventional RXS), or additionally analyzed by a spectrometer in energy-resolved inelastic mode (RIXS). Conventional RXS has the benefit of relatively short counting times and enabled the efficient exploration of the doping and temperature dependence of CDW correlations in many cuprates, including Hg1201 [69, 106]. Figure 3.1 shows a RXS measurement of CDW correlations in Hg1201 with different doping levels [69]. In the doping range from about $p = 0.064$ to $p = 0.115$ ($T_c = 55$ K to 88 K), a net CDW signal is observed after subtracting the high-temperature data. The intensity of the CDW peak decreases upon heating above T_c and saturates at the doping-dependent characteristic temperature T_{CDW}. Unlike for YBCO, where the CDW response exhibits its maximum intensity at $T = T_c$, in Hg1201 the intensity remains unchanged in the superconducting state. The CDW correlation length in Hg1201 ($\sim$ 4-6 planar lattice units, calculated from the FWHM of the peak) is much smaller than

that in YBCO. Similar temperature-dependent CDW correlations were also observed in Hg1212 via RXS (Figure 3.2) [71].

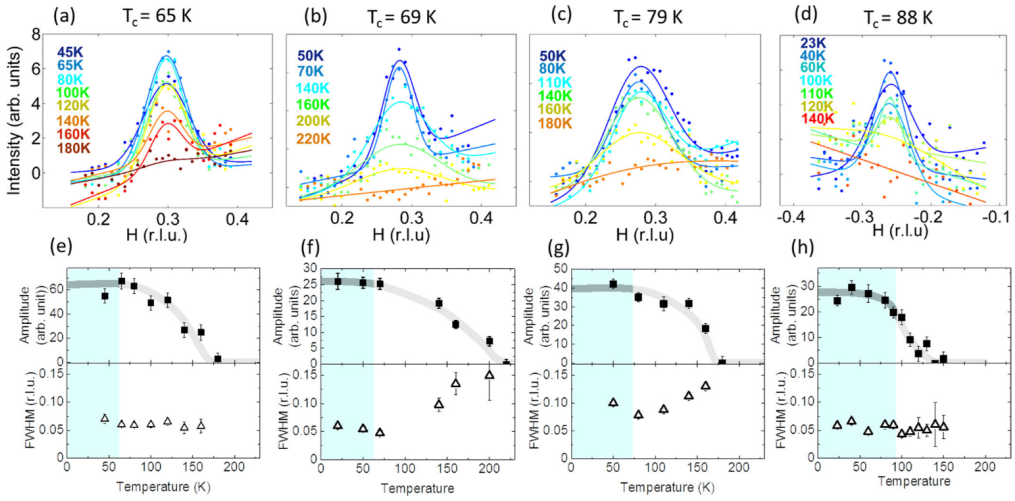

Figure 3.1: Temperature dependence of CDW correlations in Hg1201 measured by conventional RXS, reproduced from [69]. (a)-(d) Temperature dependence of the background-subtracted CDW peak for four Hg1201 samples. The peak intensity decrease upon heating above T_c and saturates at the doping-dependent characteristic temperature T_{CDW}. The solid lines are fits to Gaussian functions on top of an assumed linear background. (e)-(h) Temperature dependence of the peak amplitude and width (FWHM). Blue areas indicate the superconducting state for each sample. The thick gray lines are guides to the eye.

3.2.2 Revised Phase Diagram

As shown in Figure 3.3, the temperature T_{CDW} determined from RXS is in very good agreement with the characteristic temperature T_{OPT} obtained from pump-probe optical measurements [133]. The doping dependence of these characteristic temperatures forms a dome shape, with a maximum that corresponds to the center of the $T_c(p)$ plateau, where the deviation from the interpolated parabolic $T_c(p)$ dependence is the largest. This is indirect evidence for the competition between CDW order and superconductivity.

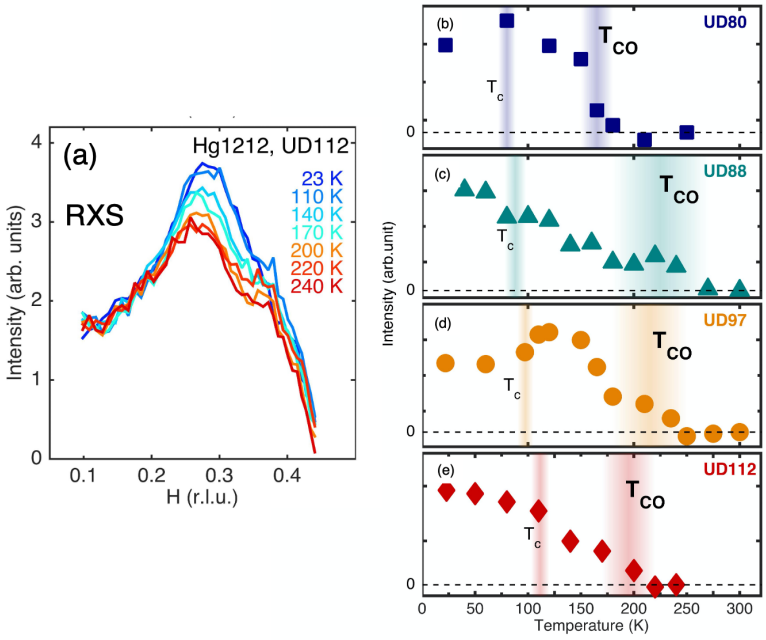

Figure 3.2: Temperature dependence of CDW correlations in Hg1212 measured by RXS, reproduced from [71]. (a) RXS spectra of the Hg1212 UD112 sample measured at different temperatures. (b)-(e)Temperature dependence of CDW intensity of different Hg1212 samples after the subtraction of the data obtained at the highest measured temperature. The intensities here are amplitudes of fits to a Gaussian function. The narrow vertical lines indicate the superconducting transition temperature T_c of each sample, and the wide vertical lines indicate T_{CDW}, the onset of the observed temperature dependence.

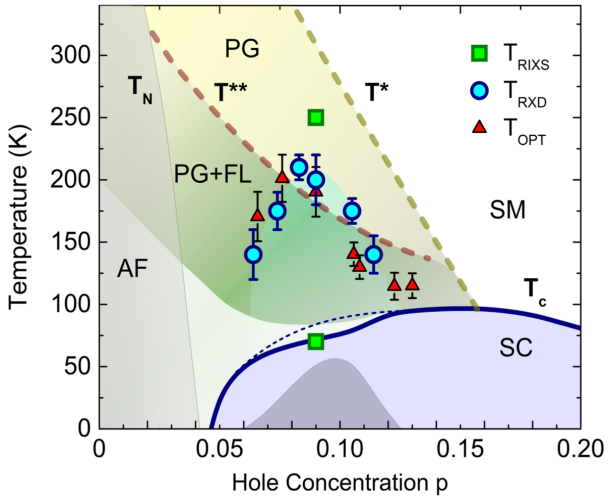

Figure 3.3: Hg1201 phase diagram ($p > 0.04$), extrapolated to $p = 0$ based on results for other cuprates [7]. Solid blue line: Doping dependence of the superconducting (SC) transition temperature $T_c(p)$ [134]. Dark gray region: Deviation (not to scale) of $T_c(p)$ from the estimated "ideal" parabolic dependence (dashed blue line). T^*: Pseudogap (PG) temperature, estimated from the deviation from strange-metal (SM) T-linear resistivity behavior [124,128]. T^{**}: Temperature below which Fermi-liquid (FL) behavior is observed in the PG state [124,126–128]. T_{RXD}: Onset of short-range CDW correlations estimated from RXS measurements [69,106]. T_{OPT}: Characteristic temperature observed in time-resolved optical reflectivity measurements [133]. T_{RIXS}: Temperatures at which the Hg1201 sample ($T_c = 70$ K, $p \sim 0.086$) was measured in this Thesis work.

3.3 Cu L-edge RIXS Measurement of Hg1201

The CDW order determined by RXS exhibits short in-plane correlation lengths, and there is no evidence for a phase transition in the absence of an applied c-axis magnetic field [69, 106]. Gaining further understanding of these emergent correlations and their connection with the pseudogap phenomenon is the primary focus of this Chapter. The comparatively high onset temperatures, reduced dimensionality, and short length scales suggest that significant dynamic CDW correlations might be present, in analogy with well-known systems such as $NbSe_2$ in the presence of point disorder [135]. On the other hand, the CDW phenomenology in the cuprates is quite different from conventional systems, as it occurs in the part of the phase diagram that is dominated by the highly unusual pseudogap phenomenon.

3.3.1 Experimental Setup

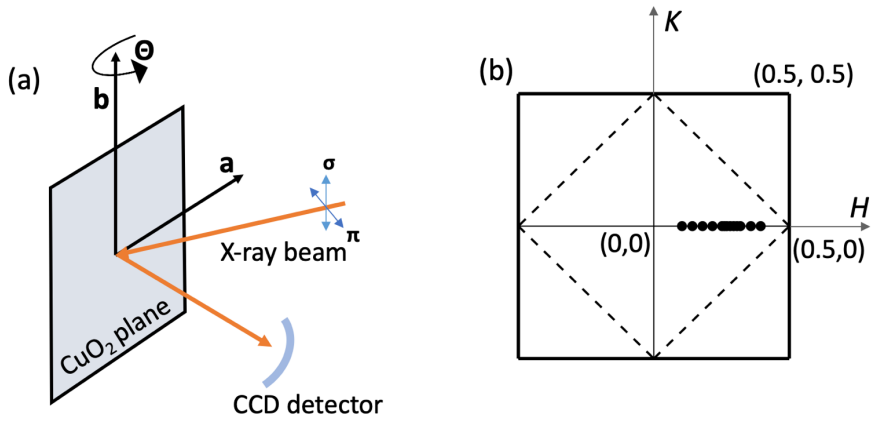

Figure 3.4: Cu L-edge RIXS scattering geometry. (a) Scattering geometry with two different incident photon polarizations: parallel (π) and perpendicular (σ) to the ($H0L$) scattering plane. (b) Reciporcal-space schematic with first nuclear and antiferromagnetic Brillouin zones (solid and dashed lines, respectively). Circles: H values accessed in the experiment.

RIXS is a unique probe to study dynamic charge correlations. The measurements were performed with the ERIXS spectrometer at beam line ID32 of the European Synchrotron Radiation Facility (ESRF), Grenoble, France. The incident X-ray energy was

tuned to the maximum of the Cu L_3 absorption peak around 932 eV, and the X-ray polarization was set either parallel (π) or perpendicular (σ) to the scattering plane. The scattered photons were analyzed without considering the final-state polarization. The energy resolution was approximately 60 meV, as determined from the full width at half maximum (FWHM) of the non-resonant spectrum of a standard polycrystalline silver sample. In order to prepare a clean and high-quality surface, the Hg1201 single crystal ($T_c = 70$ K, $p \sim 0.086$) was cleaved *ex situ* to reveal a face parallel to the CuO_2 planes. Momentum scans were performed by rotating the sample about the axis perpendicular to the scattering plane, and the detector angle was set to $2\theta = 150^\circ$. The scattering geometry is shown in Figure 3.4.

The intensity of the RIXS spectra was normalized to the integrated intensity of *dd*-excitations, following prior work [136]. Energy calibration (determination of zero energy transfer) was performed at each momentum transfer by measuring the non-resonant spectrum of standard polycrystalline silver located near the sample. As a consistency check, the energy of *dd*-excitations was examined and not found to drift with temperature. Figure 3.5 shows the raw RIXS spectra measured at 70 K and 250 K with σ- and π-polarized incident photons.

3.3.2 Dynamic Charge Correlations

Figure 3.6 show RIXS intensity contour plots at $T = 70$ K and 250 K, respectively, as a function of H and energy transfer ω (negative ω corresponds to energy loss), obtained with σ-polarized incident X-rays directly from individual energy scans such as those shown in Figure 3.5. The maps clearly display signal around $\boldsymbol{q}_{CDW} \approx (0.28, 0)$, consistent with prior RXS work [69,106]. Whereas the dominant signal at 70 K is elastic, at 250 K ($> T_{\mathrm{CDW}}$) the response is dynamic and centered in the optic phonon range. Due to the larger phonon contribution, the 250 K spectra exhibit higher intensity away from $\boldsymbol{q}_{CDW}$ than the 70 K data. Although weaker, as expected, charge correlations are also observed in π polarization (Figure 3.5).

A more detailed data analysis reveals additional information. Figure 3.7(a-d) shows the momentum dependence of RIXS signal (obtained from energy scans such as those in Figure 3.6(c), with σ polarization) integrated over the FWHM energy resolution (60 meV) with different energy ranges: quasi-elastic (-30, +30) meV; inelastic (-90, -30)

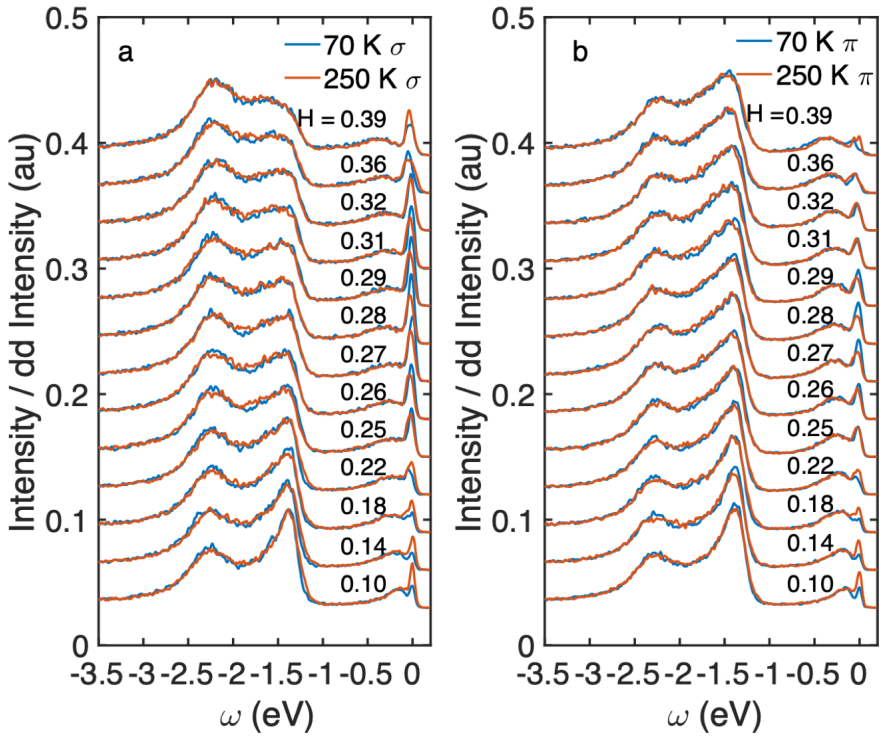

Figure 3.5: Cu L-edge RIXS spectra measured at 70 K and 250 K with (a) σ- and (b) π-polarized incident photons.

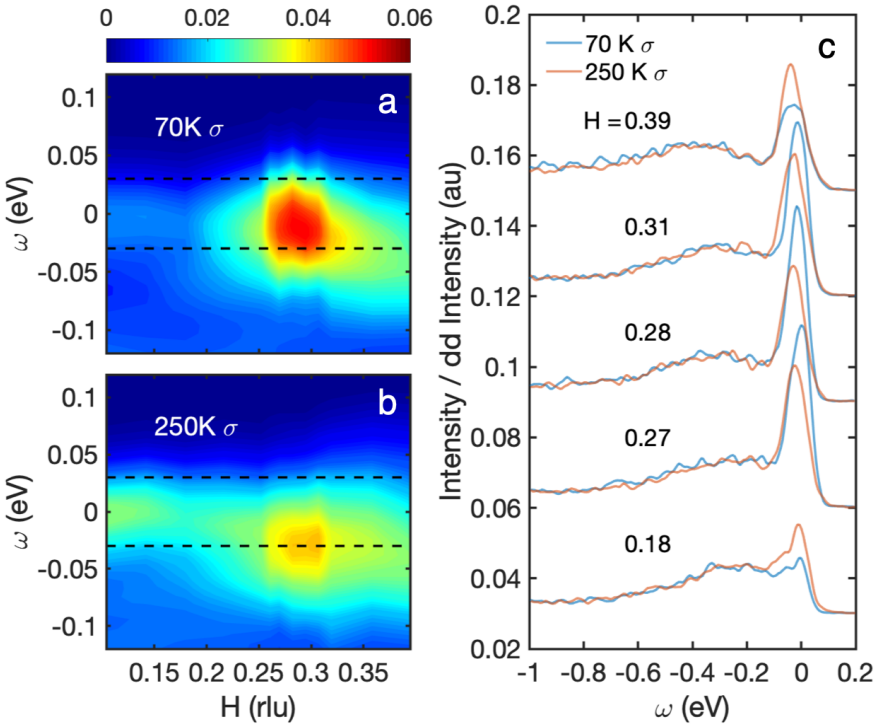

Figure 3.6: (a) and (b): Momentum-energy contours of RIXS spectra at 70 K and 250 K, obtained with σ polarization. Dashed lines: full-width-at-half-maximum (FWHM) energy resolution of 60 meV. (c) Spectra at select H values, obtained with σ polarization; data vertically shifted for clarity.

meV, (-150, -90) meV and (-210, -150) meV. In order to arrive at a systematic estimate of the q-integrated signal strength, we perform a heuristic fit of the data to a Gaussian peak, with fixed center ($\boldsymbol{q}_{CDW}$) and width ($\sim$ 0.075 rlu), plus a concave, polynomial contribution. For Hg1201, the optic phonon range extends to about 75 meV [137–139], and for energy transfers in this range the 'background' contribution invariably includes phonon scattering; for all energy-integration ranges, this smoothly-varying contribution is indistinguishable at 70 K and 250 K.

Figure 3.8(a,b) shows the energy dependence of the Gaussian amplitude obtained in this manner for σ- and π-polarization, respectively. As expected for charge scattering, the signal is weaker for π-polarization. The 250 K results show broad peaks centered at $\sim$ 40 meV and no evidence for elastic scattering, as the energy dependence of the amplitude is fully captured by the sum of Stokes and anti-Stokes scattering. The peaks are considerably broader than the 60 meV energy resolution. Assuming a heuristic intrinsic Gaussian profile, we estimate an intrinsic width of at least 50 meV (FWHM) after resolution deconvolution. The RIXS signal may be interpreted either as a single charge mode, with a width that is comparable to its characteristic energy, or as the result of a large distribution of charge modes. We note that our analysis removes *featureless* phonon contributions. Whereas the broad peak in Figure 3.6(b) contains low-energy excitations, especially phonons, those at $\sim$ 40 meV in Figure 3.8 (a,b) are either directly or indirectly associated with enhanced charge correlations at $\boldsymbol{q}_{CDW}$. As discussed in detail below, the latter may in principle include anomalous phonon scattering.

At 70 K, the dominant charge response is quasi-elastic. The width of this peak is larger than the energy resolution, consistent with a dynamic contribution at $\sim$ 40 meV that is unchanged from the response at 250 K. This distinct possibility is highlighted for both polarizations in the (Bose-factor-corrected) intensity difference plots in Figure 3.8(c,d), which reveal resolution-limited elastic peaks centered, within error, at $\omega = 0$.

Interestingly, at 70 K we also observe dynamic CDW signal above the optic phonon range. This is *directly* seen from Figure 3.7, especially Figure 3.7(e), where the large binning range (-280,-120) meV was chosen in order to optimize signal-to-background. These data, obtained with σ-polarization, are contrasted in Figure 3.7(f) with the equivalent result with π-polarization, which is more sensitive to magnetic scattering. The convex momentum dependence can be attributed to paramagnons, which become prominent

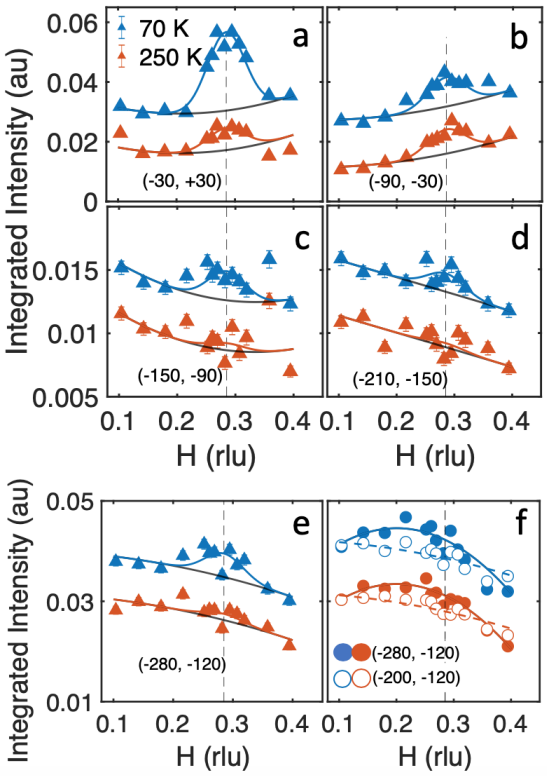

Figure 3.7: RIXS intensity integrated over different energy ranges. (a-d) σ-polarized RIXS intensity spectra at 70 K and 250 K, integrated over the 60 meV FWHM instrument resolution, centered at zero, 60, 120 and 180 meV energy loss. (e) σ and (f) π-polarized RIXS spectra at 70 K and 250 K, integrated over larger energy windows, as indicated. In all cases, the 70 K curves are vertically shifted for clarity. The black lines in (a-e) are polynomial momentum dependences, and the same in each case at low and high temperature. Blue and red lines in (a-e): fits to Gaussian profiles plus a smoothly varying contribution at 70 K and 250 K, respectively. Blue and red lines in (f): guides to the eye. Vertical dashed grey lines indicate $\boldsymbol{q}_{CDW}$. The errors are one standard deviation (square root of total photon count).

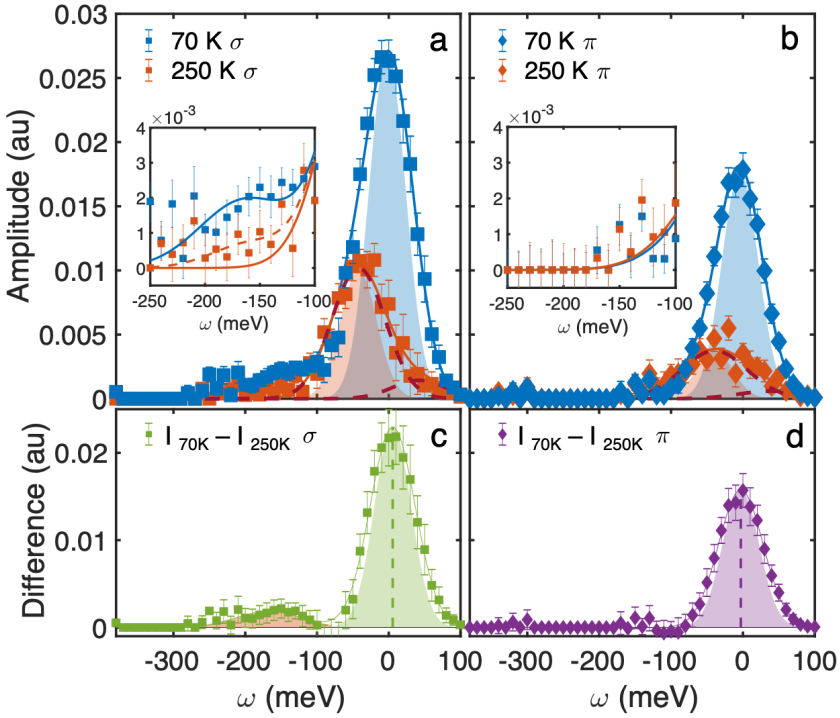

Figure 3.8: Energy- and temperature-dependence of charge response at $\boldsymbol{q}_{CDW}$ for (a) σ- and (b) π-polarization from fitted Gaussian amplitude in Figure 3.7(a-d). The error bars indicate fit errors. Insets: zoom of the range (-250, -100) meV; the dashed red line in the inset to (a) indicates the possibility of non-zero charge scattering in this energy range at 250 K. Blue and red shaded areas indicate the instrument resolution 60 meV (FWHM). Gaussian fits to Stokes and anti-Stokes scattering at 250 K (dashed red lines; sum: solid red lines) yield 41(4) meV and 64(12) meV (FWHM) for the peak position and intrinsic (de-convoluted) peak width. Gaussian fits to three peaks at 70 K (blue lines) capture (1) quasi-elastic, (2) low-energy ($\sim$ 40 meV), and (3) high-energy (peak at 163(12) meV, intrinsic width of 77(16) meV (FWHM)) contributions to the CDW response; the latter is not discerned in π-polarization, for which the overall charge response is expected and seen to be weaker. (c) and (d): difference in amplitude between 70 K and 250 K from (a) and (b), respectively, after correcting the 250 K data for the Bose factor. Green and purple shaded areas indicate the instrument resolution; vertical dashed lines indicate peak centers obtained from fits to Gaussian profiles, which are consistent with zero energy transfer. The orange shaded area in (c) indicates the net signal centered at 160(6) meV.

above $|\omega| \sim 200$ meV at $\boldsymbol{q}_{CDW}$ (see below). This is seen from the comparison in Figure 3.7(f) with the result obtained with narrower (-200,-120) meV integration, which yields an approximately linear background, consistent with the σ-polarization result in Fig. 2(e). From Figure 3.8(a), the high-energy charge signal is seen to be peaked at about 165 meV; it is not discerned in π-polarization (Figure 3.8(b,d)) due to the higher background level (proximity to paramagnon excitations; Figure 3.7(f)) and lower expected charge scattering cross section (by a factor of two). We note that the 250 K data in Figure 3.7 and 3.8(a) are consistent with non-zero high-energy charge signal, although with a smaller amplitude and potentially larger momentum width than at 70 K.

Note that the dynamic charge response can be equally well modeled as a distribution of modes of different energies. Such an analysis is shown in Figure 3.9, where a log-normal distribution is assumed at zero temperature. Unlike the fit to the heuristic Gaussian form in Figure 3.8, which yielded a large intrinsic width, the log-normal distribution is zero in the $\omega = 0$ limit. The high-temperature (250 K) data can be modeled using Bose-Einstein statistics and detailed balance. The line shape is further convoluted with the Gaussian resolution function.

3.3.3 Paramagnon Excitations

Figure 3.6(c) reveals an additional broad, dispersive peak in the 0.15 to 0.4 eV range. This feature, which has been observed in a number of cuprates, signifies paramagnon scattering that evolves from well-defined antiferromagnetic excitations in the undoped parent compounds [140, 141]. These excitations are more prominent in π- than in σ-polarization in the present scattering geometry, as expected for magnetic scattering [142, 143].

In order to extract the paramagnon response, we decompose the mid-infrared region of the RIXS spectra into three components using the heuristic form [142, 144]:

$$\frac{I}{I_{dd}}(\omega) = G(\omega) + n_B L(\omega) + n_B \chi''(\omega), \tag{3.1}$$

where $n_B = [1 - \exp(-\hbar\omega/k_B T)]^{-1}$ is the Bose factor, $G(\omega)$ a resolution-limited Gaussian function that captures the elastic peak, $L(\omega)$ a resolution-limited Lorentzian profile used to effectively capture the phonon contribution, and the paramagnon is fit to a

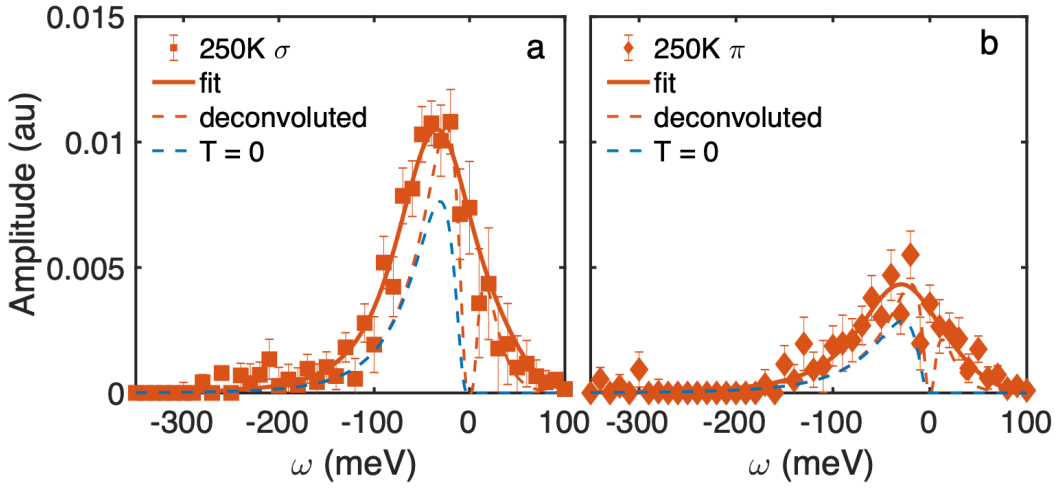

Figure 3.9: Dynamic charge correlations at 250 K modeled with a log-normal distribution in (a) σ- and (b) π-polarization. The data (filled square and diamond symbols) are the same as in Figure 3.8 (a,b). The solid red lines are the results of fits to a resolution-convoluted log-normal distribution with a mean energy of 49(2) meV. The dashed red lines indicate the deconvoluted charge response at 250 K. The blue dashed line is the Bose-corrected charge susceptibility at zero temperature.

damped harmonic oscillator form:

$$\begin{aligned}\chi''(\omega) &= \chi_0'' \frac{\gamma\omega}{\left[\omega^2 - \omega_0^2\right]^2 + \omega^2\gamma^2} \\ &= \frac{\chi_0''}{2\omega_1}\Big[\frac{\gamma/2}{(\omega-\omega_1)^2 + (\gamma/2)^2} - \frac{\gamma/2}{(\omega+\omega_1)^2 + (\gamma/2)^2}\Big],\end{aligned} \tag{3.2}$$

with damping coefficient $\frac{\gamma}{2} = \sqrt{\omega_0^2 - \omega_1^2}$. In addition, a linear background is assumed. In order to model the RIXS spectra, $G(\omega)$, $L(\omega)$ and $\chi''(\omega)$ are further convoluted with the instrument resolution function. Figure 3.10 shows the fits to the 70 K RIXS spectra measured in π-polarization.

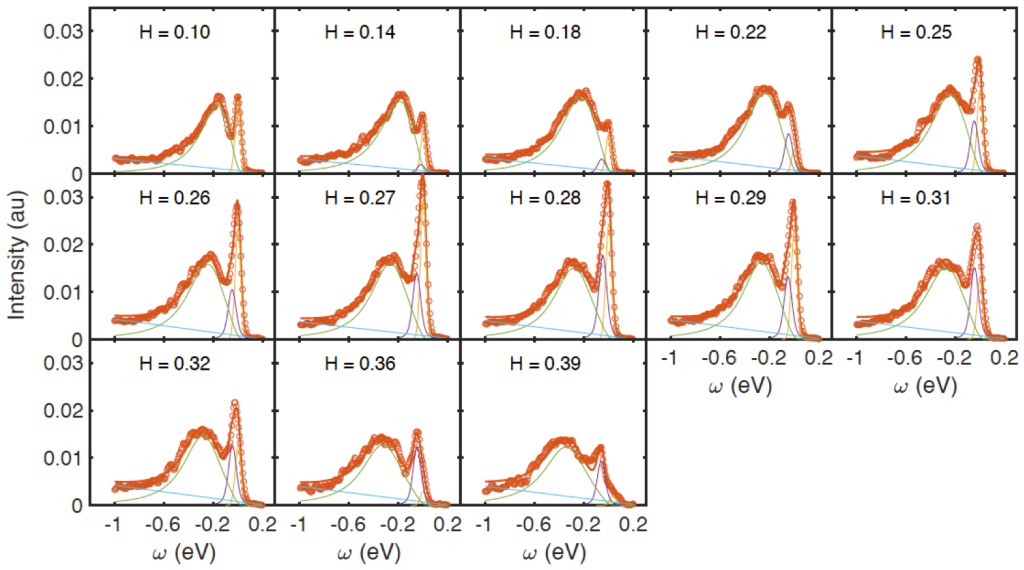

Figure 3.10: Heuristic fits to RIXS data taken at 70 K in π geometry, in which the paramagnon response is strongest, with in-plane momentum transfer H indicated. The spectra are decomposed into three components plus a linear background (blue): a resolution-limited elastic peak (yellow), a resolution-limited effective phonon peak (purple), and a damped paramagnon excitation (green).

Figure 3.11 summarizes our result for the paramagnon dispersion along [1,0] at 70 K. We compare the RIXS data with magnetic neutron scattering data near the antiferromagnetic wave vector for two Hg1201 samples (one with essentially the same doping level and $T_c = 71$ K [129], and the other with $p \approx 0.064$ and $T_c = 55$ K [82]) and

find that these results are highly consistent and complementary. From a heuristic fit of the combined neutron and X-ray data above $H = 0.1$ rlu to simple linear spin-wave theory, we obtain an effective nearest-neighbor exchange of 123(3) meV. The relatively large uncertainty and limited data near the zone boundary prevent a more detailed analysis [145, 146].

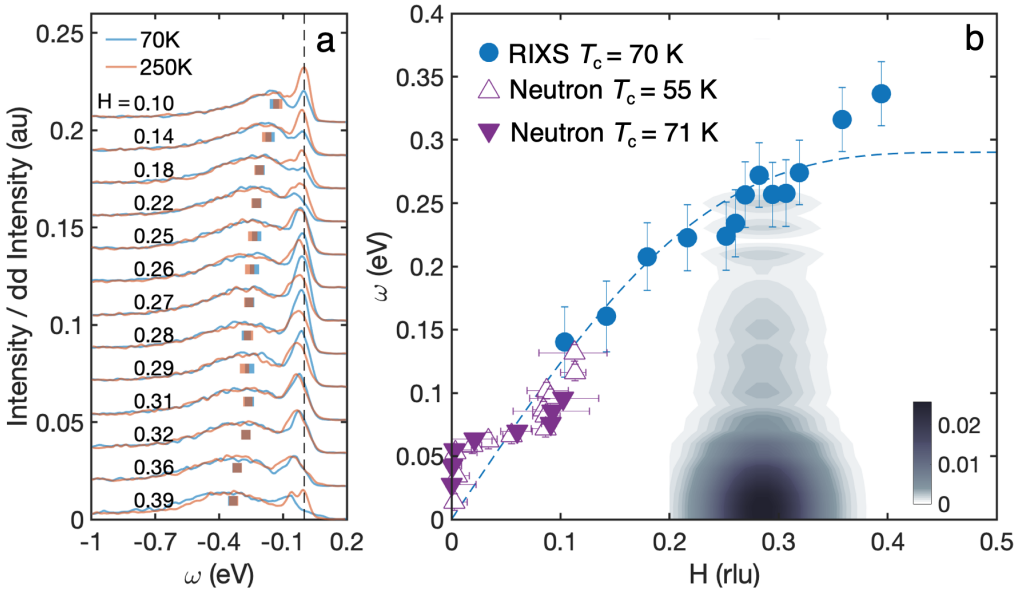

Figure 3.11: Paramagnon dispersion. (a) RIXS spectra for Hg1201 at numerous wave vectors along [1,0], obtained in π-polarization. Data are vertically shifted for clarity. Blue and red bars indicate the paramagnon energy obtained from fits to a damped harmonic oscillator form. (b) Dispersion of magnetic excitations in Hg1201 measured by RIXS (this work; $p = 0.086, T_c = 70$ K) and neutron scattering for two Hg1201 samples: one with nearly the same doping level and $T_c = 71$ K [129], and the other with a slightly lower doping level $p \approx 0.064$ and $T_c = 55$ K [82]. Blue dashed line: heuristic fit to nearest-neighbor spin-wave theory. Error bars for RIXS data are set to 30 meV, i.e., half of the FWHM energy resolution. The contour indicates the CDW intensity at 70 K (Figure 3.8(a)).

Figure 3.12 compares the magnetic dispersion along $[1, 0]$ with results for doped and undoped $La_{2-x}Sr_xCuO_4$ [145–148]. The paramagnon dispersions for LSCO ($p = x = 0.11$) [147] and Hg1201 ($p \approx 0.086$) agree within error up to at least $H = 0.35$ rlu.

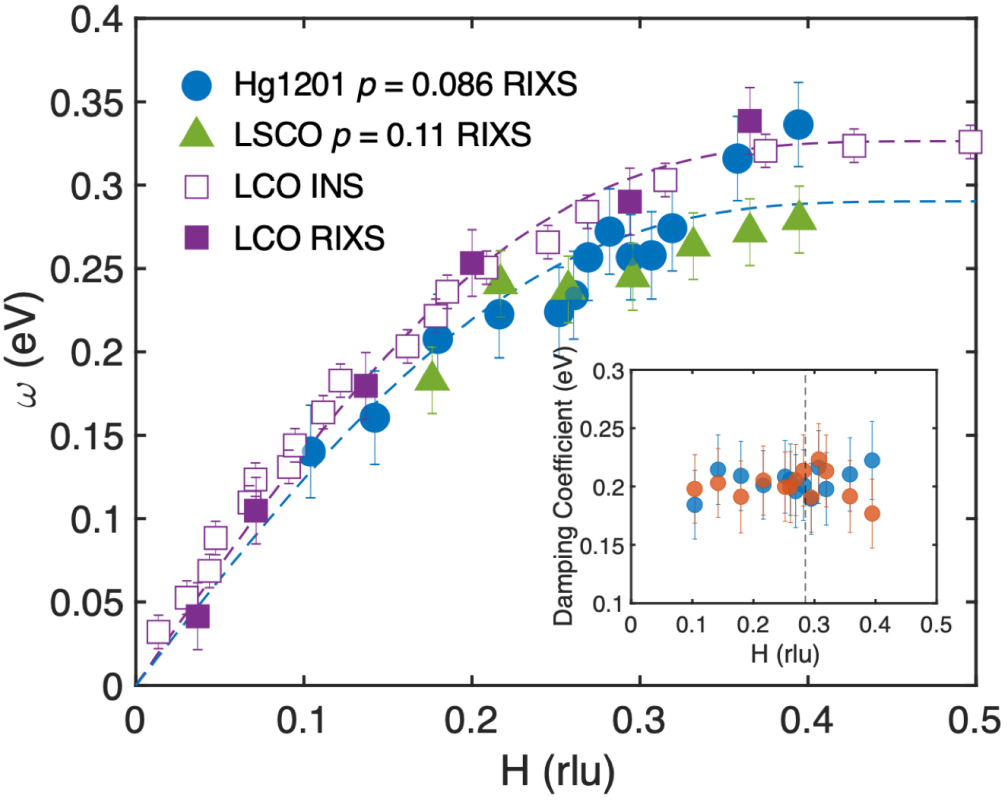

Figure 3.12: Dispersion of magnetic excitations in Hg1201 ($p \approx 0.086$) at $T = 70$ K, compared with undoped antiferromagnetic La_2CuO_4 (LCO) [145, 146, 148] and 11% Sr-doped $La_{2-x}Sr_xCuO_4$ (LSCO) [147]. Blue and purple dashed lines are simple fits to nearest-neighbor spin wave theory for Hg1201 and LCO, respectively. Inset: damping coefficient for Hg1201 at 70 K and 250 K, with error bars set to the energy resolution (30 meV - HWHM). Neither the paramagnon dispersion nor the damping coefficient shows anomalous behavior at $\mathbf{q}_{CDW}$.

3.4 Discussion

We observe charge signal in three different energy ranges: (1) a quasi-elastic response at 70 K; (2) low-energy ($\sim$ 40 meV) signal at 250 K and at 70 K; (3) high-energy fluctuations with a characteristic energy of about 165 meV at 70 K. In this Section, we first discuss how our observations differ from conventional CDW systems. We then consider the possibility that the 40 meV feature signifies a phonon-related effect. Finally, we discuss our findings within the broader context of the cuprate phase diagram and, in particular, the pseudogap phenomenon and the superconducting pairing glue.

3.4.1 Cuprates vs. Conventional CDW Systems

Analogous to conventional superconductors, conventional CDW systems are described by BCS theory [149]. The CDW state is a condensate of electrons and holes, characterized by a complex order parameter, whose net momentum corresponds to the wavelength of the charge order. In clean, weak-coupling systems, macroscopic phase coherence and amplitude formation occur simultaneously at the mean-field transition temperature. In the presence of disorder or at strong coupling, on the other hand, the transition temperature can be significantly depressed, and such systems may exhibit extended pseudogap-like behavior with a gap that persists to high temperature in the absence of long-range order. Such an extended precursor regime has been demonstrated for the canonical CDW compound $2H-NbSe_2$ intercalated with Mn and Co, i.e., in the presence of point disorder [135].

The pseudogap and charge-order behavior of the cuprates is more complex. These compounds transform from Fermi-liquid metal at high doping, with a large Fermi surface that encompasses $1 + p$ carriers, to a Mott insulator at zero doping ($p = 0$) via an intermediate state with carrier density p [124, 150, 151]. This evolution involves the localization of exactly one hole per planar CuO_2 unit and the concomitant opening of a pseudogap on the antinodal parts of the underlying Fermi surface, which leaves ungapped nodal Fermi arcs with carrier density p below T^{**} (Figure 3.3), the lowest of three characteristic pseudogap temperatures (the other two are T^* and T_{hump}, with $T^{**} < T^* < T_{hump}$) [120, 152]. This Mott-pseudogap phenomenon is distinct from the

pseudogap of a canonical CDW system in the presence of strong coupling and/or disorder [135]. In the cuprates, the onset of short-range CDW correlations is generally observed at or below T^{**} (Figure 3.3). Associated with the three characteristic pseudogap temperatures are characteristic energy scales, which at the doping level of the present study are about 40-50, 60-80 and 180-220 meV [152, 153]. The lowest of these energy scales is the value of the pseudogap near the tip of the arcs [153], whereas the largest scale has been associated with the charge-transfer gap of the insulator, renormalized by the itinerant carriers [120]. Since the pseudogap formation is gradual and precedes the CDW order [154, 155], and because the wavevector $\boldsymbol{q}_{CDW}$ appears to connect the tips of the arcs [69, 106, 130], the 40-50 meV pseudogap scale likely sets an upper bound for the CDW gap scale. From the BCS expression $2\Delta = 3.5k_BT_{CDW}$, with $T_{CDW} \sim 200$ K (Figure 3.3), one would expect a gap of $\Delta \sim 30$ meV. Given the considerable point disorder exhibited by the cuprates [122], it is perhaps not surprising to observe CDW correlations over an extended temperature range below T_{CDW}, along with a dynamic signature above this nominal ordering temperature, which in this case most likely represents a pinning temperature rather than a true phase transition.

However, Figure 3.8(c,d) indicates that the elastic and inelastic contributions might have somewhat different physical origins. Taken at face value, these difference plots indicate that the weight of the ~ 40 meV inelastic contribution is temperature-independent, since it cancels out within error for the two temperatures. Equivalently, there seems to be little spectral weight transfer from the ~ 40 meV inelastic to the quasi-elastic contribution on cooling, which is rather unexpected if the CDW were simply pinned below T_{CDW}. In principle, one possibility is that the elastic contribution signifies the interference of Friedel oscillations around impurities, as suggested theoretically [156] and tested in a quasi-one-dimensional CDW system [157]. The 'true' underlying CDW signal would then be inelastic even at T_c, and the CDW correlations would remain dynamic at this temperature. However, as shown most clearly for $NdBa_2Cu_3O_{6+\delta}$ (NBCO) [113], the amplitude and correlation length of the $\omega \approx 0$ signal exhibit temperature dependences below T_{CDW} that point to a gradual build-up of quasi-elastic correlations and to a phase transition below T_c, consistent with direct evidence for three-dimensional CDW order in the presence of a large c-axis magnetic field or in strained epitaxial films [101, 111, 158]. As further discussed in the following subsections, it is therefore a distinct possibility that

the temperature-independent (at least up to 250 K) $\sim$ 40 meV feature is associated with a precursor phenomenon and hence only indirectly related to the CDW: it could be a direct signature of some other bosonic charge modes, or the result of anomalous phonon scattering, and hence an indirect signature of such modes. Moreover, the 100-250 meV range of the broad feature seen at 70 K is consistent with the upper cutoff scale of the bosonic spectrum obtained from infrared spectroscopy [159, 160].

In a conventional system, CDW order involves Fermi-surface nesting. The present data do not allow us to discern if the CDW in the cuprates forms predominantly due to Fermi surface nesting or a real-space mechanism. We can, however, make some inferences at this point. The doping dependence of the CDW wave vector is consistent with a nesting scenario, and quantum oscillation measurements show that the Fermi surface is reconstructed at low temperatures and high magnetic fields, with a resultant electron pocked whose size is consistent with a simple reconstruction scenario [125, 130]. However, the quasistatic zero-field CDW correlations observed here at T_c clearly do not induce a reconstruction, since transport properties are virtually insensitive to the CDW formation at this temperature [161]. Furthermore, the presence of a significant dynamic component with high onset temperature and the emergent high-energy scale, potentially both direct signatures of the pseudogap, suggest a strong-coupling scenario, making an underlying real-space mechanism more likely. This is to be expected if the CDW is indeed an emergent phenomenon, since the correlations that cause the cuprate pseudogap appear to be local in real space, as further discussed below. It seems possible that, effectively, both k- and r-space effects contribute, which could be related to the deeper question of the existence of a well-defined reciprocal space in a material that is inherently inhomogeneous at the nanoscale [120, 162]

3.4.2 Nature of the 40 meV Excitation

The 40 meV scale is consistent with superconducting gap and pseudogap scales for cuprates with a comparable optimal T_c [152, 153], and with the lower bound of $\sim$ 20 meV for the gap between the CDW-reconstructed pockets deduced from quantum oscillation experiments for Hg1201 [130]. This scale lies in the optic phonon range and, in principle, the observed excitation might signify phonon scattering due to enhanced electron-phonon coupling, and thus be an *indirect* signature of significant dynamic

charge correlations. In hole-doped $Bi_2Sr_2CaCu_2O_{8+\delta}$ (Bi2212) [163], dispersive CDW correlations were identified up to about 60 meV and associated with strong Fano interference at the intersection with the Cu-O bond-stretching phonon. At low temperature, a gradual phonon softening near $\boldsymbol{q}_{CDW}$ was observed, with a minimum energy of 40-45 meV and an intrinsic width of 30-40 meV (FWHM). In Hg1201, at $\boldsymbol{q}_{CDW}$, the Cu-O bond-stretching phonon lies in the 55-60 meV range, whereas the Cu-O bond-bending phonon lies in the 40-45 meV range [137–139]. It is therefore possible that a similar anomaly involving predominantly the bond-bending phonon is present in Hg1201.

Alternatively, the 40 meV feature could be a *direct* signature of charge fluctuations, for a number of reasons. Unlike the result for Bi2212 [163], our data indicate no change in the ~ 40 meV charge response (amplitude, characteristic energy and width) between high and low temperatures (Figure 3.8). We estimate the *intrinsic* width of the excitation to be at least 50 meV (FWHM) (Figure 3.8). This value is considerably larger than what might be associated with phonon linewidth broadening, and about 50-100% larger than the width of the peak ascribed to anomalous phonon scattering in Bi2212 [163]. In addition, we note that conventional RXS measurements generally reveal a local intensity maximum at q_{CDW} already at high temperatures [21, 102, 105, 106, 110]. This feature is commonly regarded as a temperature-independent background and subtracted from the low-temperature data to extract the CDW signal, although it also has been associated with charge correlations [21, 163], as clearly supported by our RIXS results in Figures 3.7 and 3.8. By integrating over the whole energy range (-10, 2) eV of our experiment, we demonstrate in Figure 3.13(a,b) that our RIXS data are highly consistent with the previous RXS study of Hg1201 at the same doping level [106]. As seen from Figures 3.7 and 3.8, most of the signal originates from within the (-0.1,0.1) eV energy range.

In Figure 3.13 (c,d), we reproduce the corresponding RXS results for $Bi_2Sr_{2-x}La_xCuO_{6+\delta}$ (Bi2201, $x = 0.115$) [105] and electron-doped $Nd_{2-x}Ce_xCuO_4$ (NCCO, $x = 0.145$) [21], respectively. Like Hg1201, both of these cuprates are single-CuO_2-layer compounds. The chosen doping levels are approximately those at which the CDW phenomenon is most robust. Remarkably, the ratios of the intensity amplitudes at/near T_c and T_{CDW} lie in the narrow 35-50% range for all three single-layer cuprates. This universal behavior, along with the insights gained here for Hg1201 (Figures 3.7 and 3.8),

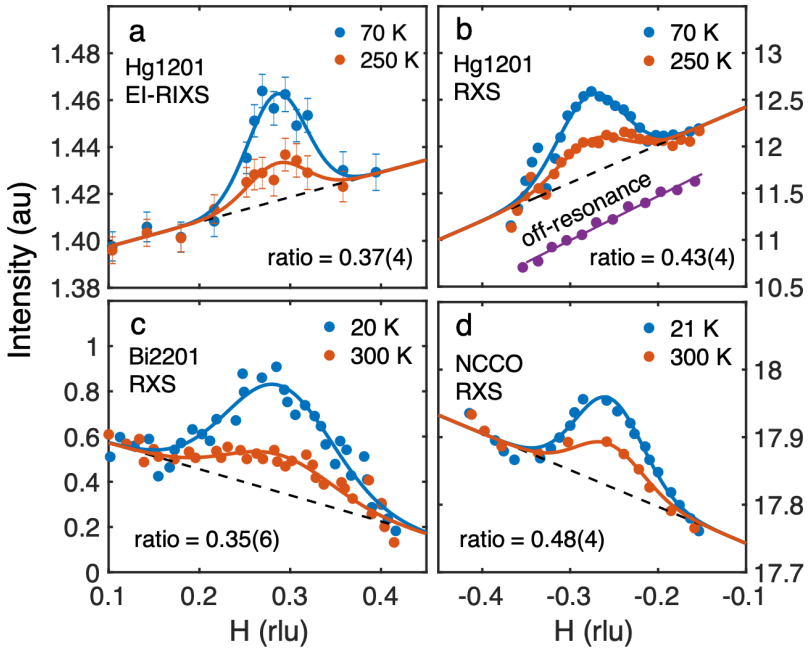

Figure 3.13: (a) Energy-integrated RIXS (EI-RIXS) data for Hg1201, integrated over the entire experimental energy range (-10, 2) eV, both at T_c and 250 K. (b) Prior RXS data for Hg1201 at the same doping level and temperatures as in (a), along with 70 K data taken off resonance with an incident photon energy of 929 eV, reproduced from [106]. (c) RXS measurement of $Bi_2Sr_{2-x}La_xCuO_{6+\delta}$ (Bi2201, $x = 0.115$) at $\sim T_c$ and 300 K, reproduced from [105]. (d) RXS results for superconducting electron-doped $Nd_{2-x}Ce_xCuO_4$ (NCCO, $x = 0.145$) at $\sim T_c$ and 300 K, reproduced from [21]. In all cases, the high-temperature data are vertically shifted for comparison with the low-temperature result. Black dashed lines: assumed linear background. Solid lines: fits to Gaussian peak plus assumed linear background. Estimates of relative peak amplitudes are indicated in all panels.

points to the existence of universal dynamic charge correlations, in addition to quasi-elastic correlations that emerge below T_{CDW}. Since phonon dispersions vary among the cuprates, and because any anomalous electron-phonon coupling can be expected to vary as well, this appears to rule out the possibility that the 40 meV feature we observe for Hg1201 is primarily related to anomalous phonon scattering. Finally, we note that there exists indirect evidence for collective charge modes from neutron and X-ray scattering experiments of phonon anomalies throughout the superconducting doping range [164, 165].

The above observations point to universal dynamic charge correlations that extend to high energy and temperature, and that have little temperature dependence between room temperature and T_c. Moreover, given that prior RXS measurements have revealed a local intensity maximum at/near $\boldsymbol{q}_{CDW}$ even at high and low doping levels where there is no evidence for quasi-critical, low-temperature CDW correlations [108], we conclude that there exist universal dynamic charge correlations in a very large portion of the temperature-doping phase diagram. As discussed in the next subsection, this conclusion is further supported by indications from Raman spectroscopy of underlying dynamic charge modes that may, in fact, extend through the entire Brillouin zone. Therefore, these robust dynamic charge correlations appear to be a precursor to the quasi-critical CDW correlations that gradually develop below the doping-dependent temperature T_{CDW} in a relatively narrow portion of the phase diagram, and that ultimately cause Fermi-surface reconstruction at very low temperatures, once superconductivity is suppressed with a c-axis magnetic field. Time- and frequency-resolved optical spectroscopy measurements support our conclusion that the $\sim$ 40 meV response is of predominantly electronic nature, although it is possible that strongly-coupled phonons and other lattice vibrations contribute as well [166].

3.4.3 Comparison with NBCO

Figure 3.14 compares our result (Figure 3.8) with data for $Nd_{1+x}Ba_{2-x}Cu_3O_{7-\delta}$ [113]. In contrast to our data analysis for Hg1201 (Figures 3.7 and 3.8), which removes featureless phonon contributions from the H-dependent intensity at/near $\boldsymbol{q}_{CDW}$, the NBCO data were analyzed under the assumption that phonon contributions at $\mathbf{q} = (H, 0)$ can be removed by subtracting data at the same $|\boldsymbol{q}|$ along $\boldsymbol{q} = (H, H)$. Although the UD60

(T_c = 60 K) sample studied in [113] has a doping level that is closer to our Hg1201 (T_c = 70 K) sample, we consider the phonon-subtracted NBCO data here, which are only available for the optimally-doped sample NBCO OP90 (T_c = 90 K). The data in Figure 3.14 are scaled to match the low-temperature amplitudes. We observe that the relative strengths of the signal at T_c and 250 K is very similar in both cases. Both compounds show quasi-elastic CDW correlations at T_c. The data analysis of [113] involved theoretical considerations of nearly critical CDW correlations. At 250 K and 150 K, the characteristic energy of dynamic charge correlations for NBCO was estimated to be 15 meV, whereas at T_c a value of 7 meV was obtained [113]. In Figure 3.14, we show that the NBCO OP90 data at 250 K can also be modeled as single-mode Stokes and anti-Stokes excitations with energy 18 ± 3 meV, consistent with [113].

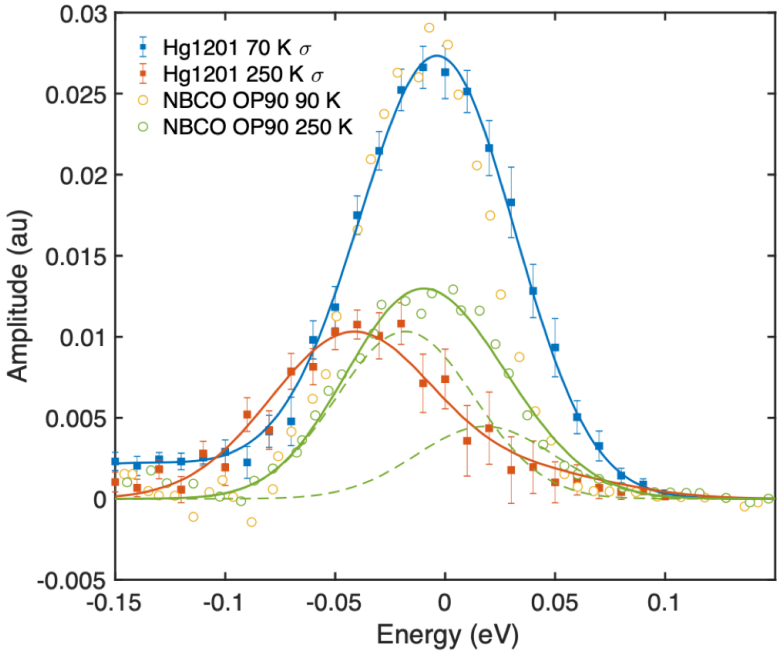

Figure 3.14: Comparison with scattering amplitude for optimally-doped NBCO OP90 (T_c = 90 K) at $\mathbf{q} = (0.31, 0)$, with data obtained at $\mathbf{q} = (0.22, 0.22)$ subtracted [113] (yellow and green circles), with the present result (Figure 3.8) for Hg1201 (T_c = 70 K; blue and red squares). The solid green line is a heuristic fit to the NBCO OP90 250 K data assuming single-mode Stokes and anti-Stokes contributions (dashed lines). The peak is centered at 18 ± 3 meV, consistent with the analysis result of 15 meV in [113].

However, as noted, the analysis of NBCO [113] involved the subtraction of RIXS spectra along $[H, H]$ from the data of interest along $[H, 0]$. We note that phonon scattering along $[H, H]$ and $[H, 0]$ is not necessary equivalent, that the required sample rotation might introduce systematic errors, and that elastic diffuse scattering from the sample surface may have an effective momentum and temperature dependence. In Figure 3.15, we fit the phonon-subtracted RIXS spectra for NBCO OP90 to the sum of a Gaussian quasi-elastic peak (to effectively capture the quasi-elastic CDW response, a possible net low-energy phonon contribution, and spurious elastic diffuse scattering) and a Gaussian excitation profile with Stokes and anti-Stokes components (to capture a dynamic mode, convoluted with the Gaussian energy resolution). The data at 90 K, 150 K and 250 K are *simultaneously* fit, with same excitation energy (ω_0), width (γ_0), and amplitude (A_0, further corrected by the thermal Bose factor). To account for quasi-elastic CDW correlations, we allow the width of quasi-elastic peak (γ_{el}) to be slightly larger than the energy resolution (40 meV). We allow the amplitude of the elastic peaks (A_{el}) to vary with temperature to capture the onset of quasi-elastic CDW correlations. Given the multiple sources of systematic errors noted above, the fits give a rather good description of the NBCO OP90 data, as seen from Figure 3.15. The analysis yields a dynamic charge excitation scale of $\omega_0 = 38 \pm 4$ meV, consistent with our result for the lower of the two dynamic energy scales in Hg1201, and it points to an onset of quasi-elastic CDW correlations between 150 K and 250 K in NBCO OP90.

3.4.4 Comparison with other Results for the Cuprates

High-energy charge correlations above the optic phonon range have been reported so far only for electron-doped NCCO, where they persist up to approximately 0.4 eV [70]. Figures 3.7 and 3.8 demonstrate for hole-doped Hg1201 at the investigated doping level that the full dynamic response is captured by integrating up to about 0.3 eV. We estimate that at least 20% of the dynamic charge response at 70 K originates from above the optic phonon range.

The large ~ 165 meV energy scale identified here for hole-doped Hg1201 is consistent with the high-energy pseudogap ("hump") scale seen in other observables [120, 152]. A recent phenomenological model, rooted in the dual empirical observations of a universal transport scattering rate [128, 167] and inherent inhomogeneity [74, 131, 168], associates

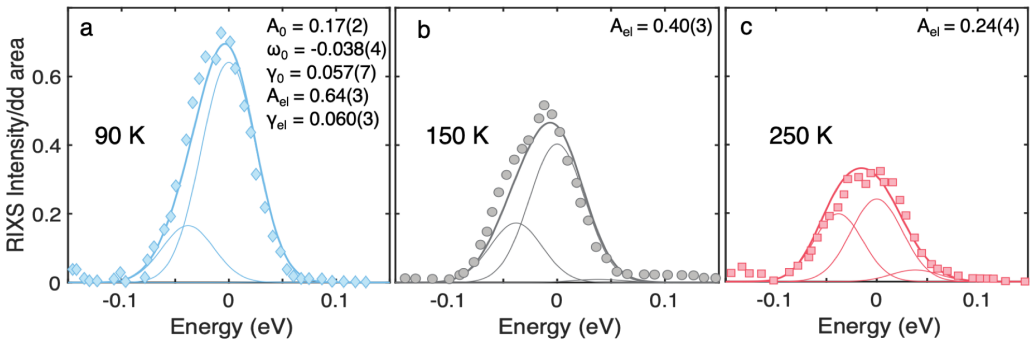

Figure 3.15: Analysis of phonon-subtracted NBCO OP90 RIXS data, as described in the text. The solid lines are fits to an effective Gaussian quasi-elastic peak plus an effective Gaussian excitation profile with Stokes and anti-Stokes components. As seen from the figure, the latter is only relevant at 250 K. No resolution-deconvolution is attempted. Except for the amplitude of the effective quasi-elastic peak (A_{el}), all parameters are globally fit, i.e., the same at all three temperatures. A_0, ω_0 and γ_0 are the amplitude (corrected by the thermal Bose factor), characteristic energy, and FWHM of the dynamic charge mode, respectively; γ_{el} is the FWHM of the effective quasi-elastic peak. The data are reasonably well described with a temperature-independent (up to the thermal Bose factor) dynamic charge response at all temperatures. This analysis yields $\omega_0 = 38(4)$ meV and an intrinsic width of 41(10) meV, consistent with the present work for Hg1201.

this scale with the charge-transfer gap at zero doping and with the delocalization of one hole per planar CuO_2 unit above T^{**} (Figure 3.3) [120, 132]. For Hg1201, at $p \approx 0.09$, the mean (de)localization gap and (Gaussian) gap distribution width that best capture the transport data are $\sim$ 180 meV and $\sim$ 60 meV (FWHM) [120, 132], respectively, consistent with the characteristic CDW scale of 163(12) meV and width of 77(16) meV established in the present work (Figure 3.8(a,c)).

The gradual delocalization of one hole per CuO_2 unit is a large effect that clearly manifests itself in, e.g., the evolution of the Fermi-surface with doping and the strong temperature and doping dependence of the Hall number [120, 132, 151]. In contrast, the CDW order involves a relatively small fraction of one hole per unit cell. While X-ray scattering experiments cannot provide the absolute CDW amplitude, a value of about 0.03 hole per CuO_2 unit was estimated for $La_{2-x}Ba_xCuO_4$ [117]. A separate, consistent estimate can be obtained from NMR: from the universal relation between oxygen hole content and NQR frequency [169] and the ^{17}O NQR line broadening in the CDW phase [170], we estimate 0.028 hole in the Cu $3d$ orbital for Hg1201 [171]. It therefore seems likely that the CDW phenomenon in the cuprates is a secondary, emergent phenomenon related to the strong correlations that underlie the hole localization. This is supported by STM evidence for a qualitative change in the CDW form factor of Bi2212 at a characteristic scale comparable to the pseudogap scale [121]. Furthermore, it is known that the cuprates are intrinsically inhomogeneous, with local gaps that vary at the nanoscale and persist well above the PG temperature [154]. Puddles of localized charge that sustain significant dynamic correlations thus may already exist outside of the nominal pseudogap region (above $T^{**}(p)$). This could account for the present observation for Hg1201 at 250 K and for the similar result for NBCO [113].

We have argued that the high-temperature peak at/near q_{CDW} seen universally in the cuprates is dominated by dynamic charge fluctuations, which for Hg1201 at the studied doping level have a characteristic energy of $\sim$ 40 meV. Although not apparent from the data summarized in Figure 3.13, there exists evidence from RXS that dynamic charge correlations centered at/near q_{CDW} extend throughout a much larger portion of the Brillouin zone, with real-space correlations no larger than 1-2 lattice constants and little doping and temperature dependence (unlike the quasi-elastic CDW signal). This is perhaps most clearly seen from RXS measurements of $YBa_2Cu_3O_{6+\delta}$ [108],

for which we estimate the approximately doping-independent 2D-integrated strength of the high-temperature signal to be at least an order of magnitude larger than the strongly temperature-dependent quasi-critical CDW signal (at the doping level where CDW correlations are strongest), consistent with a separate estimate based on recent RIXS data for NBCO [113]. In other words, whereas it appears from data such as those in Figure 3.13 that the energy-integrated high-temperature signal is about 35-50% of the low-temperature response, it may in fact be dramatically larger. This signal might be a direct signature of the fluctuations associated with the localized hole [120, 132], and the characteristic wavevector may correspond to the distance between the antinodal regions of the Fermi surface on which the pseudogap develops, and hence be somewhat smaller than q_{CDW}. The 2D-integrated strength of the signal is still considerably smaller than what would be expected if it were fully associated with the localization of one hole per CuO_2 unit: naively, given that the CDW amplitude amplitude corresponds to about 0.03 hole per CuO_2 unit, one might expect this signal to be $(1/0.03)^2 \sim 10^3$ times larger than the quasi-critical CDW response. It is possible that there exists a considerable incoherent contribution to the charge response up to 0.3 eV and even higher energies that is not captured by RXS and RIXS experiments. Similarly, the $\sim$ 165 meV scale might not be seen at 250 K in our experiment because the high-energy charge fluctuations are incoherent at high temperatures. We note that recent momentum-resolved electron-scattering measurements of the charge fluctuations in $Bi_{2.1}Sr_{1.9}CaCu_2O_{8+\delta}$ revealed a featureless continuum up to $\sim$ 1 eV [172] for a wide range of hole concentrations from underdoped to overdoped, consistent with the existence of significant local excitations.

The above considerations are supported by neutron scattering, Raman scattering, infrared spectroscopy, and tunneling results. First, we note that evidence for an underlying collective charge mode has been deduced from anomalies in the Cu-O bond-stretching vibration in the 65-85 meV range single-layer $La_{2-x}Sr_xCuO_4$ (LSCO) in the superconducting doping range [165]. An anomalous line-width broadening was observed in the entire momentum range from the 2D zone center to the 2D zone boundary at (0.5,0) rlu. Given the large intrinsic width of the $\sim$ 40 meV feature in Hg1201, these findings for LSCO are consistent with anomalous electron-phonon coupling and a potentially universal spectrum of bosonic charge modes. Second, the $\sim$ 165 meV feature seen in our experiment appears to be related to features seen in Raman spectra with B_{1g} [173]

and B_{2g} symmetry [174]. Raman scattering probes large portions of the Brillouin zone, with distinctly different form factors in B_{2g} and B_{1g} symmetry. In B_{1g} symmetry, a broad feature with characteristic energy of $\sim$ 200 meV ($\sim$ 1700 cm^{-1}) was identified for a Hg1201 sample with a slightly larger doping level ($p \approx 0.11$, $T_c = 77$ K) and associated with the two-magnon excitations of the undoped antiferromagnetic parent compounds. We note that both paramagnon and charge correlations might contribute to this feature. While a clear temperature dependence was observed below $\sim T^*$, this feature was seen to persist to higher temperatures [173]. In B_{2g} symmetry, a feature of width $\sim$ 60 meV centered at $\sim$ 150 meV ($\sim$ 1250 cm^{-1}) was observed for Hg1201 with $T_c = 72$ K, i.e., at nearly the same doping level as the present study, and interpreted as a CDW energy scale [174]. These values are remarkably close to the intrinsic width of 77(16) meV (FWHM) and peak of 163(12) meV that we extract and associate with charge fluctuations (Figure 3.8).

We note that infrared spectroscopy efforts to extract the bosonic pairing glue revealed a robust peak around 50-60 meV and a second feature in the 100-300 meV range for a number of cuprates, including optimally-doped Hg1201 [160, 166, 175, 176]. Given that optical spectroscopy yields an average over the Brillouin zone, whereas our RIXS experiment focuses on the vicinity of $\boldsymbol{q}_{\mathrm{CDW}}$, this result is consistent with an interpretation of our data in terms of charge modes that contribute to the pairing glue. This is demonstrated in Figure 3.16, which compares the glue function extracted at 100 K for Hg1201 ($T_c = 97$ K) with our RIXS result for the dynamic response at $T = T_c = 70$ K. As noted in the previous Section, the results in Figure 3.8(a,b) are equally well captured by intrinsic heuristic Gaussian and log-normal functional forms, and the latter is used for the comparison. Also shown in Figure 3.16 is our result for the energy dependence of the strength of the paramagnon response at 70 K, as well as the momentum-integrated, dynamic magnetic susceptibility obtained from neutron measurements near the antiferromagnetic wavevector for an underdoped sample with nearly the same doping level [129]. Assuming azimuthal symmetry, the former is proportional to the 2D momentum-integrated paramagnon strength. The neutron data are available in absolute units, and the RIXS paramagnon result is scaled to match the neutron data just below 100 meV. The RIXS data for the charge response in turn are scaled up by a factor of 10 for ease of comparison and, as noted above, because

the fully-2D-integrated dynamic charge response may indeed be an order of magnitude larger than what we observe in the immediate vicinity of $\boldsymbol{q}_{\mathrm{CDW}}$ [113]. We also note that up to about 20% of the nominal paramagnon signal could be dynamic charge correlations. As seen from Figure 3.16, there exists an intriguing connection between the charge and magnetic scales obtained from our RIXS experiment and those of the pairing glue function extracted via inversion of optical spectroscopy data for Hg1201 [160]. Qualitatively similar results have been obtained from Raman scattering and Figure 3.16 includes a result for Bi2212 [177]. An analysis of Raman spectra for LSCO revealed a relatively narrow peak in the glue function below ~ 100 meV, and a broad hump up to ~ 500 meV, seen in both B_{2g} and B_{1g} symmetry channels [178]. It was concluded that, in B_{1g} symmetry, spin modes contribute more strongly and at all frequencies, whereas charge modes are particularly prevalent at low/intermediate frequency in the B_{2g} channel. Tunneling data for optimally-doped Bi2212 ($T_c = 95$ K), the lowest doping level investigated, indicate a strong local maximum at ~ 40 meV and a weaker, broad feature peaked just above 100 meV [179]. RIXS has a key advantage over these and other techniques, as it is a rather direct, momentum- and energy-resolved probe of the charge and magnetic response. The above observations point to the distinct possibility that our RIXS experiment has revealed bosonic modes that contribute to the superconducting pairing glue in the cuprates. RIXS experiments as a function of doping, and with even better energy resolution, are highly desirable to further test this intriguing possibility.

Finally, we note that a recent RIXS study of electron-doped $\mathrm{Nd}_{2-x}\mathrm{Ce}_x\mathrm{CuO}_{4+\delta}$ suggests a coupling between dynamic magnetic and charge-order correlations [70]. For the hole-doped cuprates, on the other hand, there is no clear evidence for such a coupling, except for the special case of the La-based "214" materials that exhibit charge-spin stripe order [116]. Although we can not rule out a small (20% or less) charge contribution to the nominal paramagnon response, the absence of a significant coupling is supported by the insensitivity of the paramagnon energy and width around $\boldsymbol{q}_{CDW}$ observed here for underdoped Hg1201 (Figures 3.11 and 3.12).

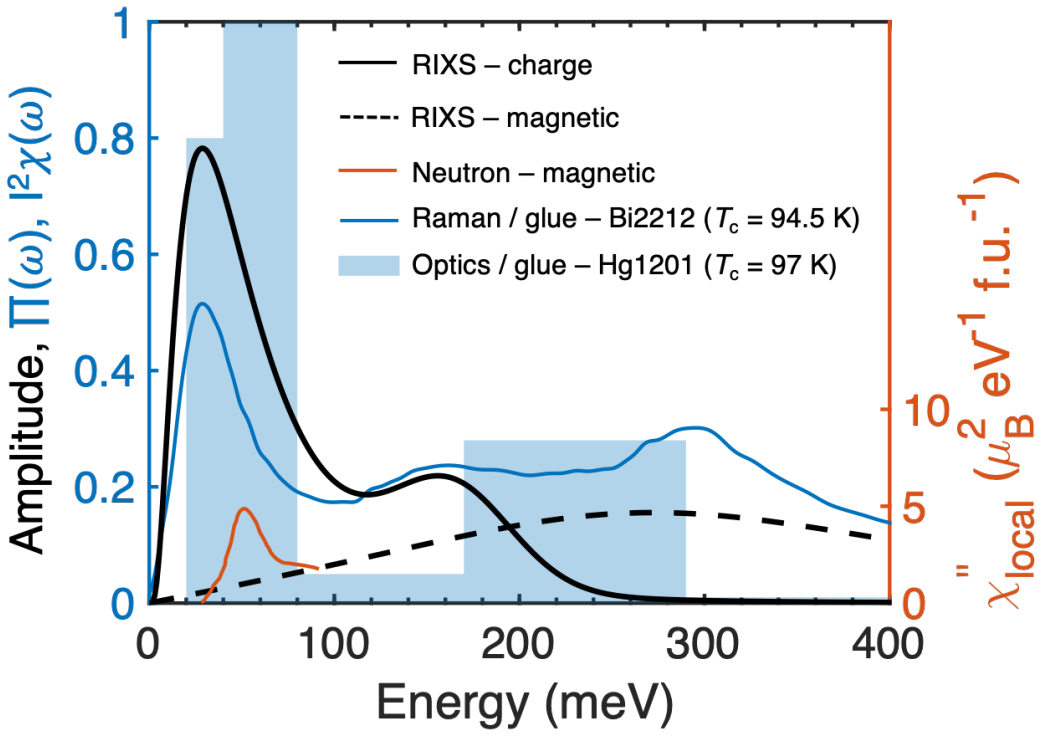

Figure 3.16: Comparison of RIXS results for dynamic charge and paramagnon response in Hg1201 with estimates for the superconducting pairing glue. The black solid and dashed lines are the charge and magnetic excitations in Hg1201 at $T = T_c = 70$ K determined in the present work. As discussed in the text, the charge signal is multiplied by a factor of 10. The red solid line indicates the local magnetic susceptibility of Hg1201 measured by neutron scattering at nearly the same doping level [129]. The blue shaded area is the bosonic glue function extracted from optical measurements of optimally-doped Hg1201 ($T_c = 97$ K) at 100 K [160]; in this work, the glue function was not extracted for underdoped Hg1201, but it was established from analysis of other cuprates that the two characteristic energy scales are rather robust in the relevant doping range. The solid blue line is a glue function estimate for Bi2212 from Raman spectroscopy [177], again at optimal doping; results in B_{1g} and B_{2g} symmetry are weighted 2:1 to best highlight the close correspondence of energy scales with the RIXS result.

Chapter 4

Phonon Anomalies

The universal charge-density-wave (CDW) order in the cuprates and the observation of dynamic charge correlations in $HgBa_2CuO_{4+\delta}$ are discussed in Chapter 3. The dynamic charge correlations potentially manifest themselves as a broadening and anomalous softening of phonon modes. In this Chapter, I discuss IXS measurements of the Cu-O bond-stretching phonon modes in both electron- and hole-doped cuprates.

4.1 Introduction

The possible roles of dynamic charge correlations and of electron-phonon coupling in driving high-temperature superconductivity in the lamellar cuprates continue to be debated [7, 164, 180]. The observation of CDW correlations in numerous cuprates via hard X-ray and soft resonant X-ray scattering constitutes a significant development in this regard, as it demonstrates a universal tendency toward some form of charge order [20, 21, 69, 102–114] (see also Chapter 3). Driven by these direct observations of charge correlations, recent phonon studies have mainly focused on low-energy phonon modes (< 10 meV) near $\boldsymbol{q}_{CDW}$ [181–184]. Due to the formation of static CDW order below T_{CDW}, a large low-energy phonon softening and broadening have been observed to occur in $YBa_2Cu_3O_{6+\delta}$ (YBCO) [181, 182] and $La_{2-x}Ba_xCuO_4$ (LBCO) [183] at low temperatures.

On the other hand, early works examining phonon anomalies in the cuprates focused on the Cu-O bond-stretching phonon modes at higher energies, in the 60-90 meV

range. This was first reported for optimally-doped $La_{2-x}Sr_xCuO_4$ (LSCO) via inelastic neutron scattering (INS), where a strong softening and broadening was observed near $\boldsymbol{q} = (0.25, 0, 0)$ [185], the wave vector associated with charge-spin stripe correlations [97]. Subsequent work indicated that the phonon softening is strongest at optimal doping ($x = 0.15$), where T_c is optimized, somewhat weaker for underdoped LSCO ($x = 0.07$), and absent in an overdoped, nonsuperconducting sample with $x = 0.30$; these results suggest a connection between phonon anomaly and superconductivity [164,186]. Similar anomalous phonon softening and broadening was subsequently observed in other hole-doped cuprates [187–189] as well as in electron-doped $Nd_{2-x}Ce_xCuO_4$ (NCCO) [137]. These phonon anomalies have been argued to signify a coupling to dynamic charge correlations [164, 165]. A recent resonant inelastic X-ray scattering study of underdoped $Bi_2Sr_2CaCu_2O_{8+\delta}$ (Bi2212) provided direct evidence for a coupling between CDW correlations and Cu-O bond-stretching phonons [163]. Therefore, the phonon anomaly can be regarded as an indirect probe of such charge correlations. More importantly, unlike the anomalous low-energy phonon modes, which are confined to the CDW phase, the anomalous Cu-O bond-stretching phonons appear to be particularly sensitive to dynamic charge correlations, as they have been observed at higher temperature and doping levels than the charge order itself [107, 164, 190, 191].

4.2 Experimental Setup

We measured Cu-O bond-stretching phonons in two different compounds: hole-doped LSCO and electron-doped NCCO. For LSCO, we measured the temperature dependence of the phonon energy and lineshape at two doping levels: underdoped ($x = 0.125$), where the CDW measured with hard X-rays is particularly robust [107], and overdoped ($x = 0.20$), where pseudogap related effects are expected to be relatively weak. For NCCO, both underdoped ($x = 0.078$) and nearly-optimal doped ($x = 0.145$) samples were measured. In order to minimize systematic errors in the comparison with prior results, we measured pieces of the very same NCCO crystals used in our recent doping-dependent study of CDW correlations [21]. The CDW is very robust in nearly-optimal doped NCCO and persists even at the highest measured temperature (380 K), whereas CDW correlations were observed to be much weaker for $x = 0.078$ and to completely

disappear at high temperature.

We employed non-resonant inelastic X-ray scattering (IXS) to characterize the phonon spectra. The IXS measurements were carried out at the ID28 beamline of the European Synchrotron Radiation Facility (ESRF) with 17.794 keV incident photons. The Si(999) reflection of the backscattering monochromator was used to achieve an energy resolution of approximately 3.0 meV (FWHM). Figure 4.1 shows a schematic of the experimental setup. In order to access a large portion of the Brillouin zone, the IXS experiments were performed in transmission geometry. In addition, the single crystals were polished to a thickness of ~ 30 μm to maximize the transmitted intensity. Energy-transfer spectra in the range -5 to 90 meV were simultaneously recorded with nine analyzers. The momentum transfer $\mathbf{Q} = (H, K, L)$ is specified in tetragonal unit cell notation, without further differentiating the low-temperature orthorhombic (LTO) phase of LSCO.

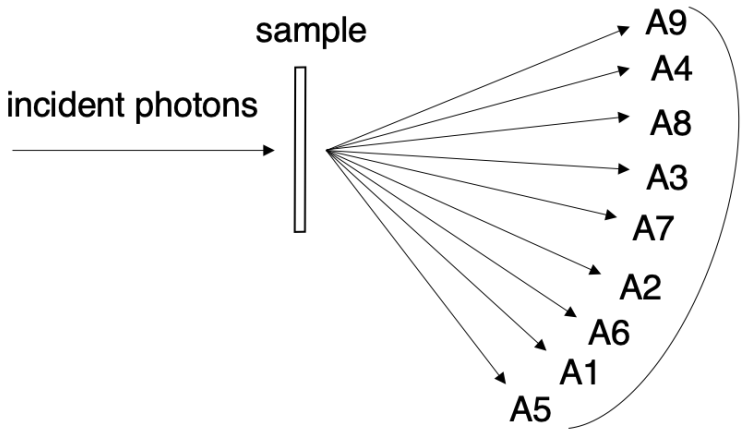

Figure 4.1: Schematic of IXS experimental setup. In order to access a large Brillouin zone volume, the IXS measurements were performed in transmission geometry. The energy of the incident photons was fixed at 17.794 keV, which resulted in an energy resolution of approximately 3.0 meV (FWHM). The IXS spectra were simultaneously recorded with nine analyzers (A1-A9).

In the IXS measurements, the phonon intensity depends on the structure factor, and thus is correlated with the total momentum transfer $\mathbf{Q}$ rather than the reduced momentum $\mathbf{q} = \mathbf{Q} - \mathbf{G}$, where $\mathbf{G}$ is a reciprocal lattice vector. We measured phonons around $\mathbf{Q} = (3 - q, 0, -5.5 \pm 0.2)$ for LSCO and around $\mathbf{Q} = (3 - q, 1, 0)$ for NCCO, as both phonon and CDW intensities are large in these Brillouin zones. Note that in both

cases, the data have mixed longitudinal and transversal phonon components.

4.3 Results

In this Section, I present the IXS measurements of the Cu-O bond stretching phonons in LSCO and NCCO. In LSCO, a clear temperature-dependent linewidth broadening is observed in the CDW-ordered $x = 0.125$ sample, whereas the effect is significantly smaller in the overdoped $x = 0.20$ sample. The observed phonon anomaly therefore appears to be related to dynamic CDW correlations or lattice distortions. In NCCO, on the other hand, the observed phonon softening and linewidth broadening are rather independent of temperature and doping, and we consider the possibility of an anti-crossing between the bond-stretching and O(2) modes.

4.3.1 Phonon Anomaly in LSCO

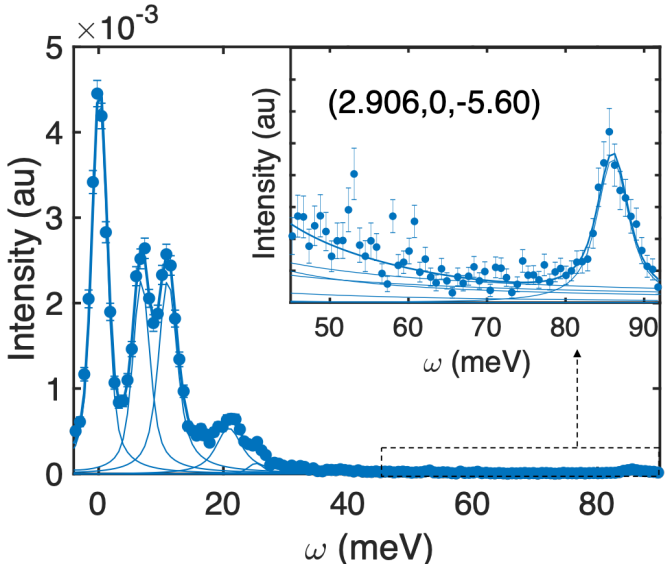

Figure 4.2: IXS phonon spectrum of LSCO ($x = 0.125$) at $\mathbf{Q} = (2.906, 0, -5.60)$ measured at $T = 20$ K. The thick solid line is the result of a fit to a sum of resolution-convoluted Lorentzian functions. The thin solid lines indicate elastic and individual phonon peaks. Inset: magnified view of the high-energy region, including the Cu-O bond-stretching phonon around 85 meV.

Figure 4.2 shows an example phonon spectrum at $\mathbf{Q} = (2.906, 0, -5.60)$. Six features can be distinguished: the peak at 0 meV, which is elastic diffuse scattering as a result of chemical disorder; low-energy phonons around 8, 12, 20, and 25 meV; and the Cu-O bond stretching phonon around 85 meV, which is the focus of the present work (highlighted in the inset of Figure 4.2). No distinct phonon peaks were resolved in the intermediate energy range from 30 to 80 meV. To extract quantitative information about the phonon energies and widths, the IXS spectra were fit to a series of resolution-convoluted Lorentzian functions with Bose factor correction. The energy resolution of each analyzer was known from prior experiments and well-described by a pseudo-Voigt function. The phonon linewidths discussed in the present work are all resolution-decconvoluted intrinsic energy widths.

In Figure 4.3, we show the spectra for $x = 0.125$ taken along $\mathbf{Q} = (3-q, 0, -5.5\pm0.2)$ at three temperatures: 20, 150 and 300 K (20 K $< T_c < T_{CDW} <$ 150 K $< T_s <$ 300 K $< T^*$, where $T_c \sim 30$ K is the superconducting transition temperature, $T_{CDW} \sim 80$ K is the onset temperature of CDW correlations at this doping level determined by hard X-ray diffraction [107], $T_s \sim 240$ K is the structural transition temperature [192], and $T^* \sim 450$ K is the pseudogap temperature [124]). Close to the zone center, at $q = 0.03$ rlu, the highest phonon energy is observed at about ~ 86 meV. The phonon energy decreases toward the zone boundary and reaches ~ 72 meV at $q = 0.38$ rlu. At 300 K, due to increased anharmonicity, a slight softening is observed at all momenta. Interestingly, at all three temperatures, a robust broadening of the phonon linewidth was observed at $q_{ph} = 0.23$ rlu, the wave vector associated with static CDW order [107].

The temperature dependence of the anomalous phonon behavior at q_{ph} is shown in Figure 4.4. The IXS spectra were fit to a single phonon mode with anomalous linewidth broadening (solid lines in Figure 4.4a), with the largest linewidth at 20 K. In addition, as noted in [186, 193], we find that the 20 K spectrum at q_{ph} can also be described by two separate phonon modes (Figure 4.4a, b); at higher temperatures, fits to two separate modes did not converge. Figure 4.4b shows that the bond stretching phonon disperses downward from the zone center to the zone boundary, following an approximately sinusoidal behavior, consistent with theoretical prediction [164]. The anomalous softening at q_{ph} observed in previous measurements [164, 165, 185, 186] is not seen, probably due to the admixture of longitudinal and transversal components as a

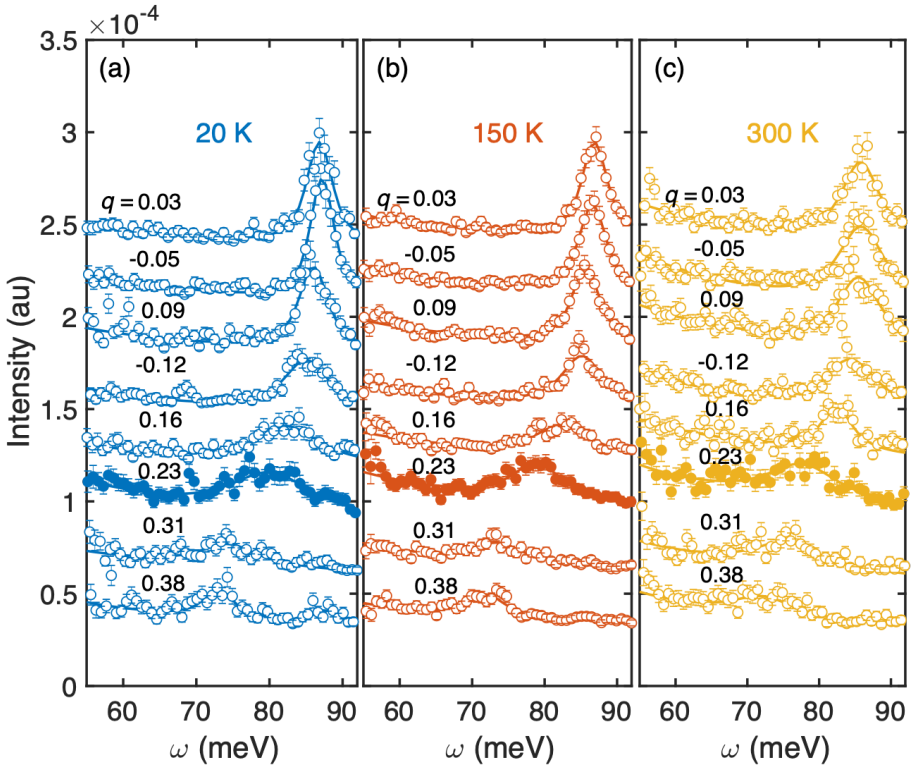

Figure 4.3: LSCO ($x = 0.125$) Cu-O bond-stretching phonon in the $\mathbf{Q} = (3-q, 0, -5.5\pm 0.2)$ Brillouin zone measured at (a) 20 K, (b) 150 K and (c) 300 K. The reduced wave vector q is indicated for each spectrum. The curves are vertically shifted for clarity. The spectra at $q_{CDW} = 0.23$ rlu are highlighted by the filled symbols.

result of the fact that $L = -5.5 \pm 0.2$, i.e., nonzero in the present work. In addition, it was noted that the phonon softening only occurs in the range $K \approx 0 \pm 0.08$ rlu [194]. The open vertical slits used in current setup result in a rather poor resolution of about 0.09 rlu (FWHM) along K, and therefore an average over phonon modes with different K values and a somewhat reduced expected softening effect compared to $K = 0$. However, this effect can not fully explain the observed lack of a softening. Nonetheless, the large linewidth broadening at q_{ph} is well reproduced in our work, as shown in Figure 4.4c. It was discussed in earlier works that the overall linewidth increase toward the zone boundary can be ascribed to inhomogeneous doping [165, 195], whereas the maximum at q_{ph} is indicative of novel charge collective modes. The amplitude of the anomalous width was found to follow the dome-like doping dependence of T_c [165].

Assuming an underlying linear linewidth increase from the zone center to the zone boundary, we obtained information on the temperature dependence of the anomalous linewidth broadening by integrating the excess linewidth above the estimated baseline (Figure 4.4c and Figure 4.5). The broadening effect is most robust at the lowest temperature (20 K), reduced (but still visible) at 150 K, and finally significantly weakened at 300 K. We note that below the structural transition (for $x = 0.125$, $T_s \sim 240$ K), the observed effect may in part be the result of the unit-cell doubling. Alternatively, dynamic translational symmetry breaking caused by incommensurate dynamic charge correlations may be the origin of this phonon anomaly. The fact that the phonon anomaly is seen above the characteristic temperature for static charge order ($T_{CDW} \sim 80$ K [107]) would then indicate that the charge fluctuations, which are difficult to probe directly (due to the relatively small cross section in IXS and the relatively poor energy resolution in RIXS), exist above T_{CDW} and potentially persist to room temperature.

With one notable exception [114], CDW order occurs in the pseudogap region of the doping-temperature phase diagram, and the characteristic temperature T_{CDW} is comparable to (not smaller than) the pseudogap temperature T^* (Figure 1.4) [69, 102–110]. In order to establish the connection between CDW and pseudogap phenomena, and also to test the extent of dynamic charge correlations, we performed similar phonon measurements on an overdoped LSCO $x = 0.20$ sample. At this doping level, we estimate $T^* < 100$ K [120] and $T_s \sim 80$ K [192]. Figure 4.6 shows the Cu-O bond-stretching

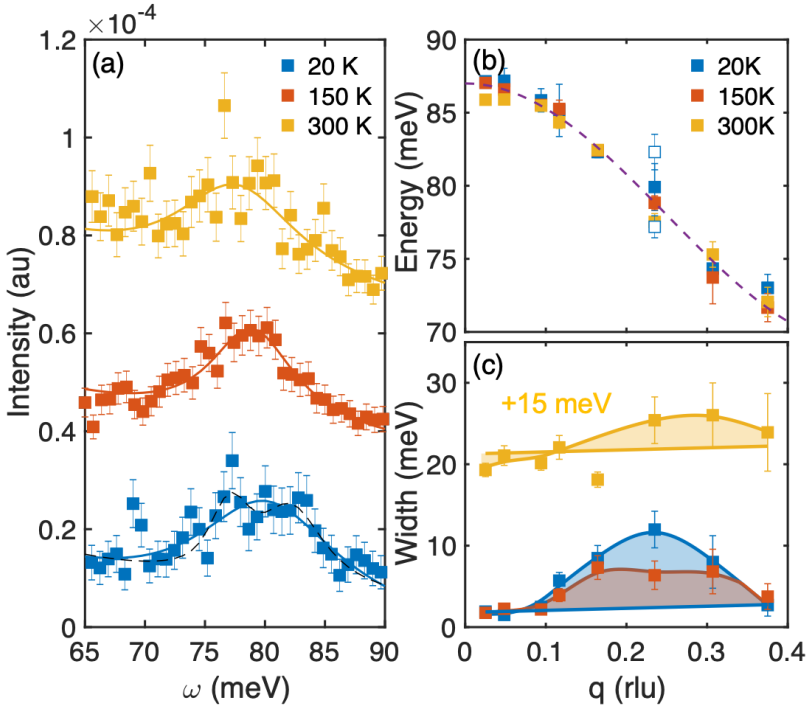

Figure 4.4: Temperature and momentum dependence of anomalous phonon in LSCO ($x = 0.125$). (a) IXS spectra at $\mathbf{Q} = (2.765, 0, -5.5)$ with fits to a degenerate phonon mode (solid line) and, at 20 K, also to two modes (black dashed line). The 150 K and 300 K data are vertically shifted for clarity. (b) Phonon dispersion along $\mathbf{Q} = (3 - q, 0, -5.5 \pm 0.2)$ at the measured temperatures. At 20 K, the filled squares correspond to fits with one mode, whereas open squares represent fits with two modes. (c) Momentum dependence of intrinsic phonon linewidth obtained from single-mode fits. Straight solid lines indicate estimated baseline width that smoothly increases toward the zone boundary. The baselines are set to be the same at all three temperatures. The shaded areas indicate the estimated anomalous linewidth above the baseline. Note that the 300 K data are shifted upward by 15 meV for clarity.

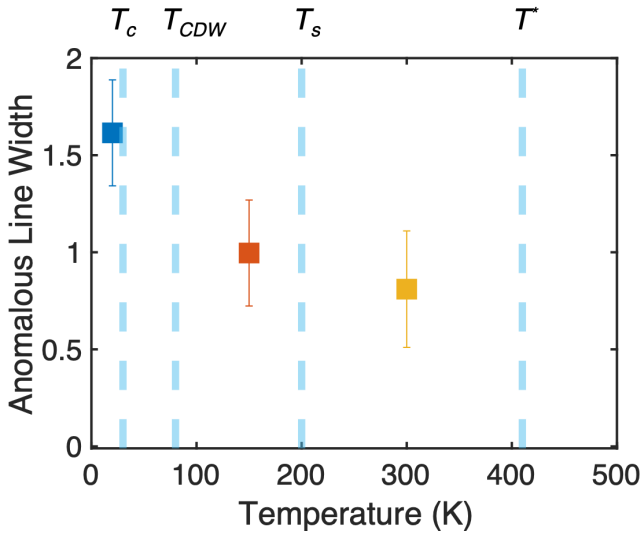

Figure 4.5: Temperature dependence of anomalous phonon linewidth for LSCO ($x = 0.125$) integrated between $q = 0.1$ and 0.37 rlu after baseline subtraction. The baseline is assumed to be linear from zone center to zone boundary [165,195], as shown in Figure 4.4c.

phonon spectra along $\mathbf{Q} = (3 - q, 0, -5.5 \pm 0.2)$. Linewidth broadening is clearly discernible at $q_{ph} \sim 0.25$ rlu and 20 K. Similar to the $x = 0.125$ sample, the linewidth is largest at 20 K and narrowers at higher temperatures (Figure 4.6b). In contrast to this, the 'normal' phonon response (e.g., Figure 4.6c at $\mathbf{Q} = (2.82, 0, -5.61)$) features a slight broadening at 300 K, as expected due to thermal lifetime effects.

The temperature dependence of the phonon dispersion and linewidth are shown in Figure 4.7. The phonon dispersion follows the expected cosine functional form at all three temperatures, with an overall softening at 300 K. The linewidth broadening is most evident at 20 K, reduced slightly at 100 K, and mostly absent at 300 K. Although the effect is weaker in overdoped LSCO, the data at/below 100 K may still be interpreted as anomalous broadening at q_{ph} due to dynamic charge correlations. However, as for LSCO ($x = 0.125$), we can not rule out the possibility of an effective broadening due to the structural phase transition. Further quantitative measurements across T_s and at even higher doping levels are required to fully resolve this question.

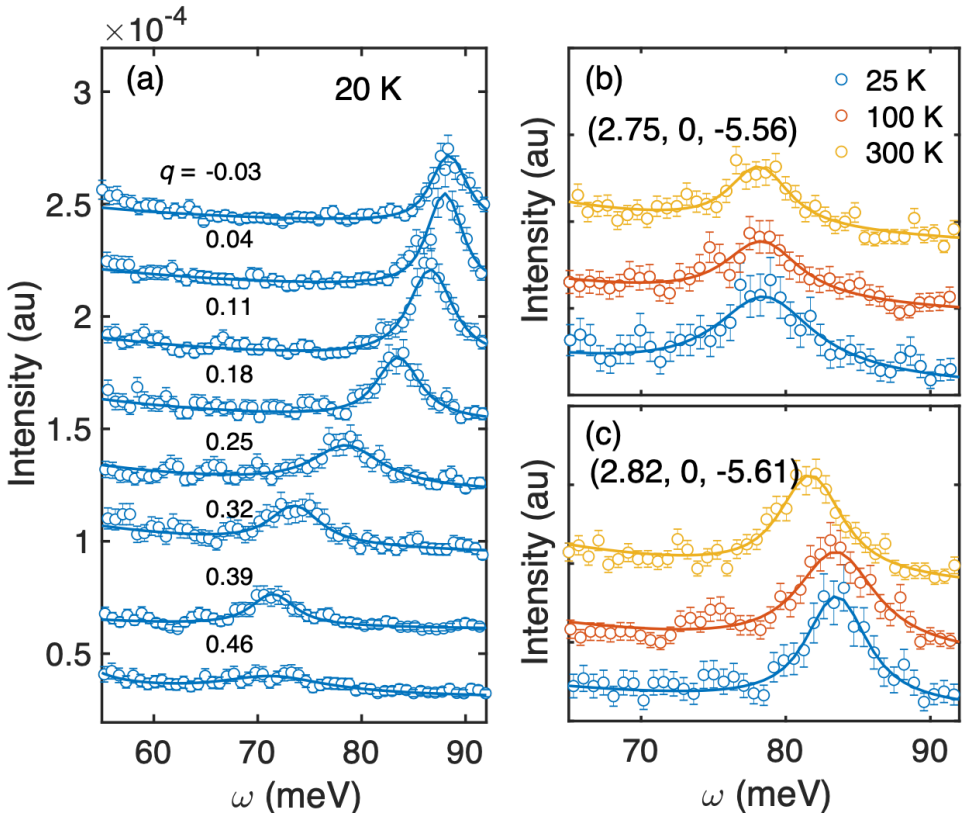

Figure 4.6: (a) Cu-O bond-stretching phonon for LSCO ($x = 0.20$) measured along $\mathbf{Q} = (3 - q, 0, -5.5 \pm 0.2)$ at 20 K, with propagation vector q indicated. The curves are vertically shifted for clarity. Temperature dependence of spectra at (b) $\mathbf{Q} = (2.75, 0, -5.56)$ and (c) $\mathbf{Q} = (2.82, 0, -5.61)$.

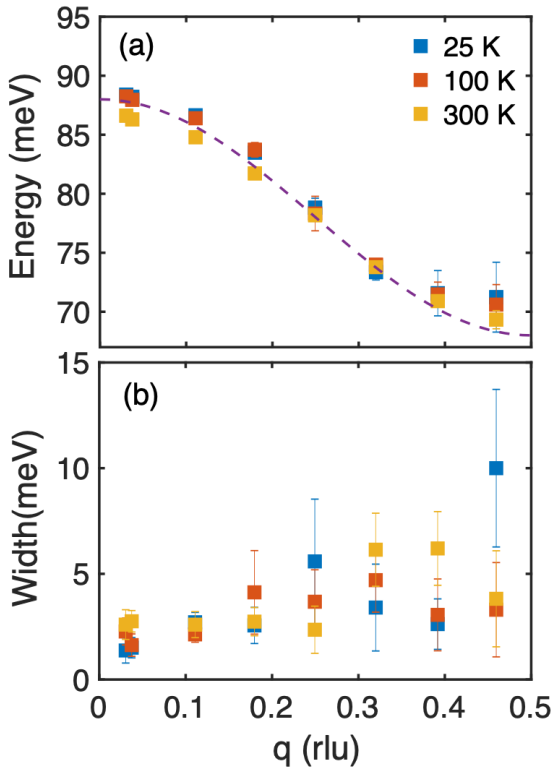

Figure 4.7: Temperature dependence of the (a) dispersion and (b) linewidth of the Cu-O bond-strentching phonon in overdoped LSCO ($x = 0.20$). Dashed line in (a) indicates the expected cosine-shaped dispersion [164].

4.3.2 Phonon Anomaly in NCCO

In order to establish a universal connection between CDW and phonon anomaly, we also performed IXS measurements of the archetypal electron-doped cuprate NCCO. The CDW in NCCO appears to be more robust than in the hole-doped cuprates, as it spans a wider doping and temperature region of the phase diagram [21]. We studied a nearly optimally-doped sample with $x = 0.145$, where CDW correlations persist up to 380 K [20, 21] and a phonon anomaly was observed at 15 K [196], and an underdoped sample with $x = 0.078$, where the CDW amplitude was found to be much weaker and to completely disappear at high temperature [21].

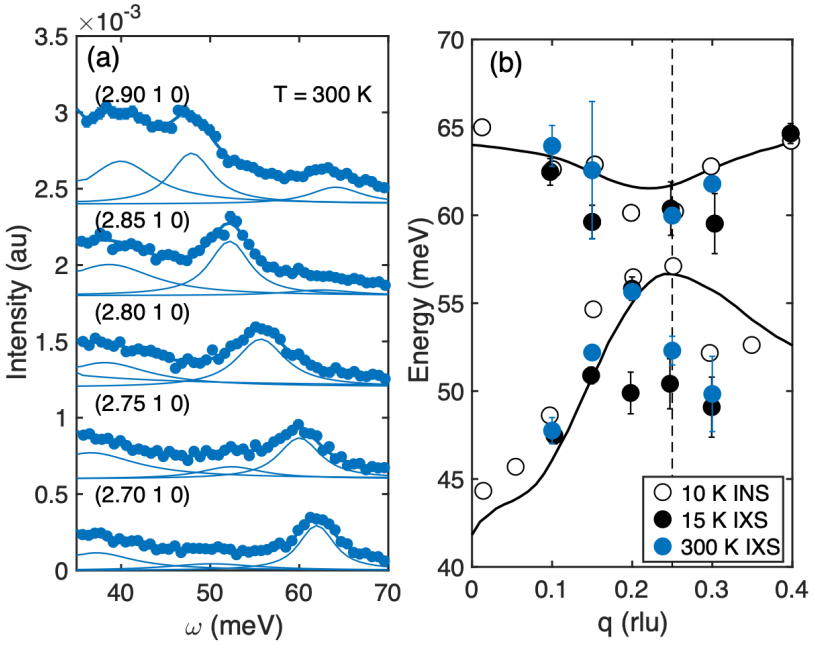

Figure 4.8: High-energy phonons in nearly optimally-doped NCCO ($x = 0.145$). (a) IXS spectra between 35-70 meV taken along $\mathbf{Q} = (3-q, 1, 0)$ at $T = 300$ K with $\mathbf{Q}$ indicated for each spectrum. The curves are vertically shifted for clarity. The data (circles) are shown together with fits to resolution-convoluted Lorzentian functions (thin blue lines: individual phonon modes; thick blue line: the sum of all modes). (b) Dispersion of the two highest-energy modes at 300 K (blue circles) compared with the prior 15 K IXS data (filled black circles) [196], and 10 K INS data (open black circles) [197] at the same doping level. The black lines are the results of a shell-model calculation [197] and the vertical dashed line indicates q_{CDW} at this doping level [20, 21].

Figure 4.8a shows IXS spectra measured along $\mathbf{Q} = (3-q, 1, 0)$ in nearly optimally-doped NCCO at 300 K. Consistent with a shell model calculation [196,197], three phonon modes can be distinguished between 35-70 meV at all momenta. Given the absence of other high-energy modes, the highest-energy mode here is identified to be the Cu-O bond-stretching phonon, and the second highest-energy mode to be the O(2) vibration mode [196, 198]. Close to the zone center, at $q = 0.1$ rlu, the highest mode is observed around 64 meV. This mode is found to decrease as q increases, and to reach a minimum energy around 55 meV at $q = 0.2$ rlu. At larger q, the energy of this mode recovers, and is found around 62 meV at $q = 0.3$ rlu. The IXS spectra were modeled as the sum of resolution-convoluted Lorentzian functions with Bose-factor corrections. The extracted peak positions at 300 K of the two highest-energy modes are shown in Figure 4.8b. Comparing to prior 10 K INS data [197] and 15 K IXS data [196], we show that the previously reported phonon softening at $q_{ph} = 0.2$ rlu persists at 300 K. Note that q_{ph} is slightly smaller than the CDW wave vector q_{CDW} determined via RXS [20, 21].

The temperature dependence of the phonons around $q_{CDW} \sim 0.25$ rlu and $q_{ph} \sim 0.2$ rlu was examined between 100 K and 500 K (Figure 4.9). If the phonon anomaly is directly associated with the CDW as in the case of low-energy phonons in YBCO [181], one would expect the soft phonon to gradually harden upon heating. However, as shown in Figure 4.9, the phonon energy remains unchanged between 100 K to 500 K.

Figures 4.10 and 4.11 show our results for the lightly-doped, non-superconducting sample ($x = 0.078$), for which only weak CDW was previously detected at low temperatures, and no CDW correlations were observed at room temperature [21]. Interestingly, the phonon softening occurs at this doping level as well, and even persists at 300 K. Figure 4.11 shows that the phonon dispersions at 20 K and 300 K are nearly indistinguishable.

Given the pronounced CDW peaks observed via RXS near optimal doping even at the highest measured temperature (380 K) [20, 21], it is in principle possible that the anomalous phonon softening at q_{ph} in NCCO is due to the coupling between dynamic charge correlations and optic phonons. In this scenario, the softening at and above 300 K indicates the existence of significant dynamic charge correlations at high temperatures. This possibility is highlighted as yellow bands in Figures 4.11 and 4.12.

However, the observation of a temperature-insensitive phonon dispersion tends to

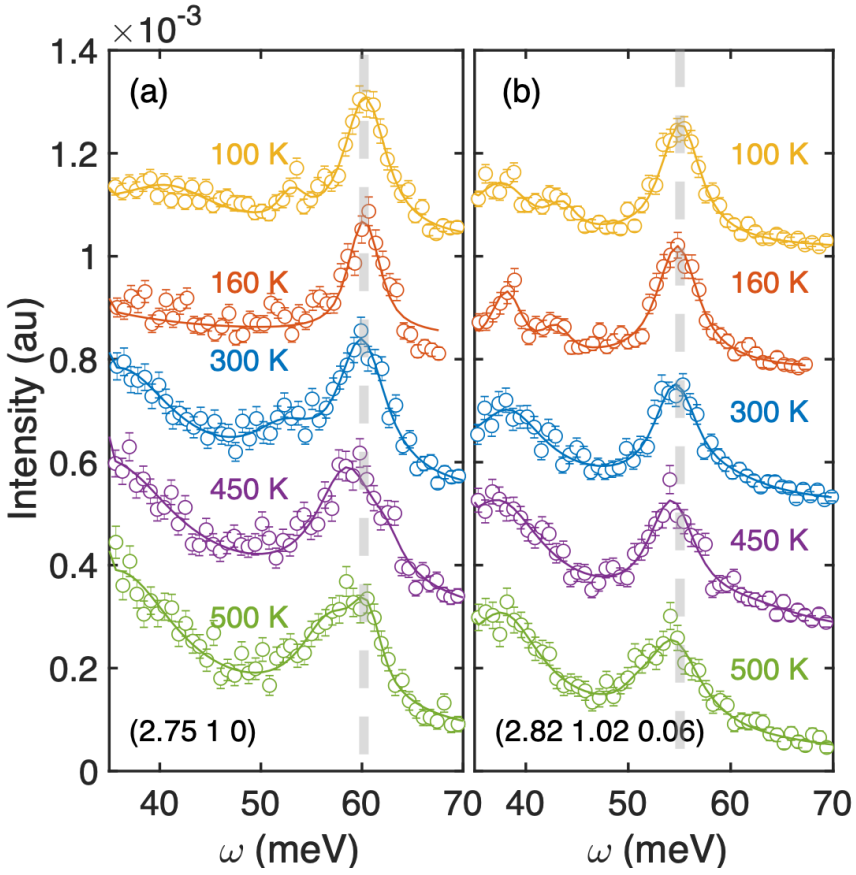

Figure 4.9: Temperature dependence of the highest-energy phonon peaks in NCCO ($x = 0.145$) around (a) the CDW wavevector $\mathbf{Q}_{CDW} = (2.75, 1, 0)$ and (b) phonon anomaly wavevector $\mathbf{Q}_{ph} = (2.82, 1.02, 0.05)$. The dashed lines indicate the phonon energy at 100 K. The solid lines are fits to resolution-convoluted Lorentzian functions. The phonon energy is nearly temperature-independent.

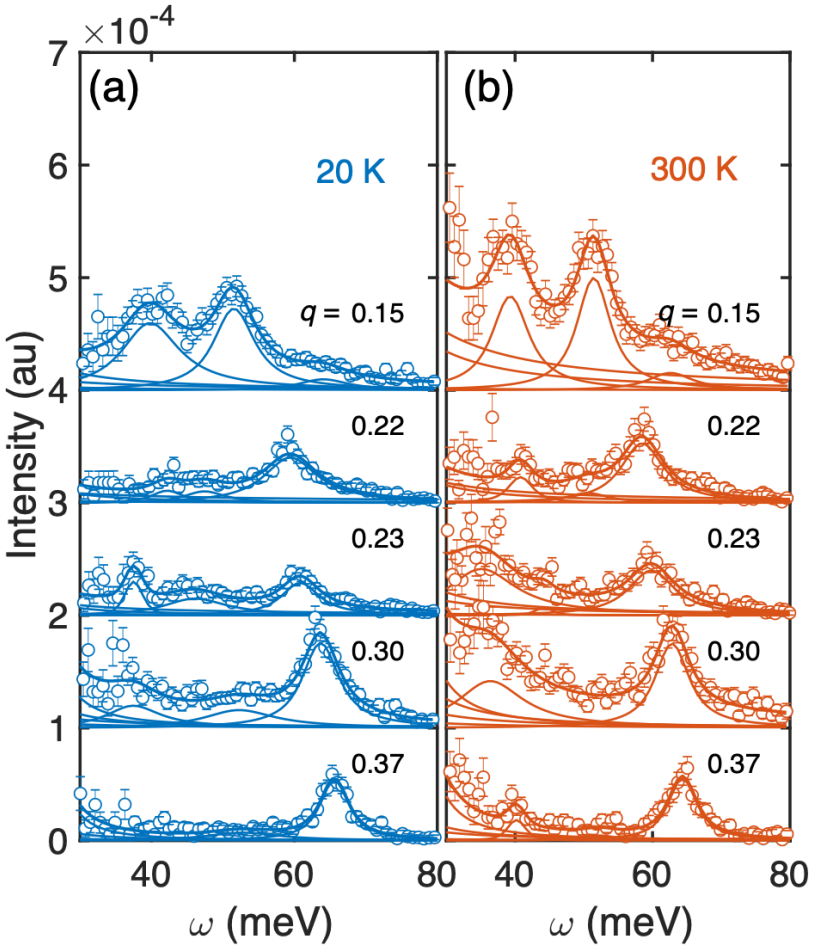

Figure 4.10: High-energy phonons in underdoped NCCO ($x = 0.078$) measured at (a) 20 K and (b) 300 K along $\mathbf{Q} = (3 - q, 1, 0)$, with q indicated for each spectrum. The solid lines are the results of corresponding fits.

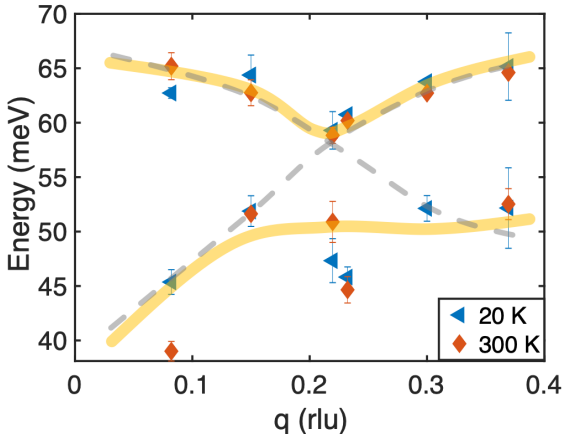

Figure 4.11: Dispersion of the two highest-energy modes in NCCO ($x = 0.078$) at 20 K and 300 K. Yellow bands: anomalous bond-stretching mode at higher energy and O(2) vibration mode at lower energy. Grey dashed lines: anti-crossing between two phonon modes.

disfavor the above scenario. Actually, as discussed in [196, 197], the phonon softening in NCCO may also be attributed to an anti-crossing between the two highest-energy modes (grey dashed lines in Figures 4.11 and 4.12), i.e., an exchange of character of the two branches occurs near q_{ph}. This is further supported by the fact that q_{ph} (~ 0.2 rlu) and q_{CDW} (~ 0.25 rlu) are inequivalent. In addition, it is known from previous RXS measurements that q_{CDW} increases with increasing doping [21]. However, as shown in Figure 4.12, the dispersions of two highest-energy modes are indistinguishable for $x = 0.078$ and $x = 0.145$, and the anomalous softening occurs at $q_{ph} \sim 0.2$ rlu in both cases. This suggests that the phonon softening at q_{ph} is not directly related to the charge instability at q_{CDW} in NCCO. Moreover, in Figure 4.13, we show the intensities of the two modes for the underdoped sample: a clear intensity exchange is observed at q_{ph}, indicative of an exchange of character between the two branches. Though, at this point, we are not able to go beyond qualitative statements, we hope to have collaborative theoretical calculation in the near future to address the underlying mechanism of phonon softening in NCCO.

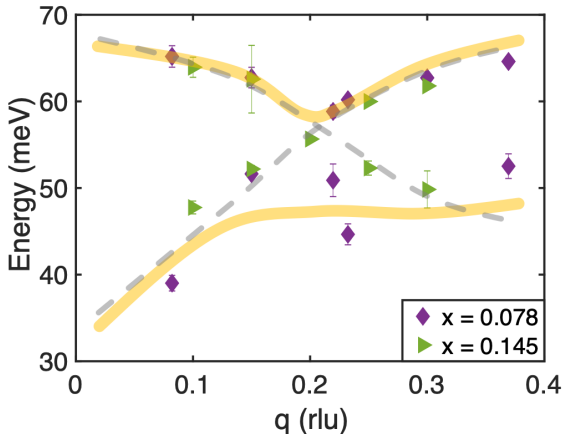

Figure 4.12: Doping dependence of the phonon dispersion in NCCO. Despite the large doping difference, the dispersions of the two highest-energy modes are almost the same for $x = 0.078$ and $x = 0.145$. Yellow bands: anomalous bond-stretching mode and a normal O(2) vibration mode. Grey dashed lines: anti-crossing between two phonon modes.

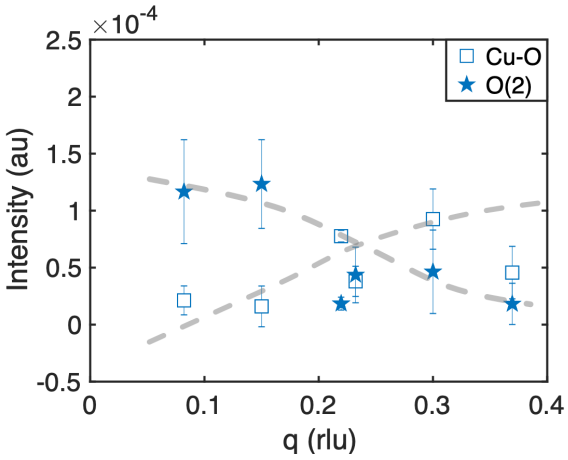

Figure 4.13: Intensity of the two highest-energy phonon modes in NCCO ($x = 0.078$). The intensity is taken to be the product of the fitted phonon amplitude and width. Evidence for an "intensity exchange" between the two modes is observed at q_{ph}.

Chapter 5

Charge-Transfer Excitations

In this Chapter, I focus on a recent Cu K-edge RIXS study of two cuprates: hole-doped $La_{2-x}Sr_xCuO_4$ (LSCO) and electron-doped $Nd_{2-x}Ce_xCuO_4$ (NCCO). The measurements, which range from low temperature (15 K) to very high temperature (1200 K), indicate distinct spectral weight changes upon heating. A detailed comparison of the temperature-dependent charge-transfer excitations in the electron- and hole-doped cuprates is presented.

5.1 Motivation

Understanding the effects of strong electronic correlations of doped Mott insulators, as highlighted by the complex phase diagram of the cuprates, is a pivotal challenge in condensed matter physics [7]. A common theoretical starting point is the Hubbard model (described in Section 1.1.3 and Figure 1.3), which features the upper Hubbard band above the Fermi level, the lower Hubbard band below the Fermi level, and the hybridized Zhang-Rice singlet state [16] near the Fermi level. Experimentally, the electronic band structure of the cuprates below the Fermi level has been well characterized by angle-resolved photoemission spectroscopy (ARPES) [199–201]. At low temperatures, the highly overdoped materials behave as conventional Fermi-liquid (FL) metals, with a large Fermi surface that corresponds to $1+p$ holes per CuO_2 unit [199,201]. The underdoped region features an unusual Fermi-arc topology as a result of the opening of the pseudogap (PG) on parts of the underlying Fermi surface [7].

Recent transport and optical conductivity measurements have revealed FL behavior in the PG part of the phase diagram as well, including the transport scattering rate $1/\tau \propto T^2$, Kohler-scaling of the magnetoresistance, and frequency-dependent scaling of the optical conductivity [124, 126–128, 167, 202]. These measurements also indicate an itinerant carrier density equal to the nomial concentration p [128,202]. A key question is if this PG/FL regime is somehow related to the FL regime at high hole concentrations. If a (hidden) FL is present in the intermediate strange-metal (SM) regime, using the Drude formula for the planar resistivity ($\rho = m^*/(ne^2\tau)$; effective mass m^*, carrier density n, electron charge e), the mysterious extended $\rho \propto T$ behavior in the SM region would then simply be the result of a temperature-independent effective mass, a T-linear carrier density, and a universal FL scattering rate $1/\tau \propto T^2$. There exists distinct evidence for this possibility [128, 167].

A recent phenomenological model, developed by our group, wherein exactly one hole per CuO_2 unit is delocalized with increasing doping and temperature, highlights the above possibility [120, 132]. The model assumes that the total itinerant carrier density (p_{eff}) is the sum of the doped carriers and of a temperature and doping dependent fraction of the holes that are fully Mott-localized at zero doping and temperature (one localized hole per CuO_2 unit): $p_{eff}(p,T) = p + \int_{-\infty}^{\infty} g(\Delta) e^{-\Delta/2kT} \mathrm{d}\Delta$, where p is the density of doped carriers and $g(\Delta)$ is the doping-dependent normalized activation-gap distribution function. The two key ingredients of the model are the experimentally-determined universal transport scattering rate [128,167] and the inherent inhomogeneity exhibited by the cuprates [74, 162, 203, 204]. Using a simple Gaussian function for the distribution of local activation energies, a doping-independent distribution width δ, and a mean Δ_p that decrease linearly with doping, $\Delta_p = \Delta_0(1 - p/p_c)$, the model successfully captures the temperature and doping dependence of the PG phenomenon, the linear temperature dependence of the planar resistivity, and the temperature-doping dependence of the Hall constant (Figure 5.1) [120, 132].

An additional test of this picture would be to observe similar doping and temperature dependences of charge excitations. The doping dependence of the dynamic charge degrees of freedom has been characterized via various techniques, e.g., optical conductivity [205–208], electron-energy-loss spectroscopy [209], and RIXS [210–218]. A famous early contribution is an optical conductivity study of LSCO that covers the full doping

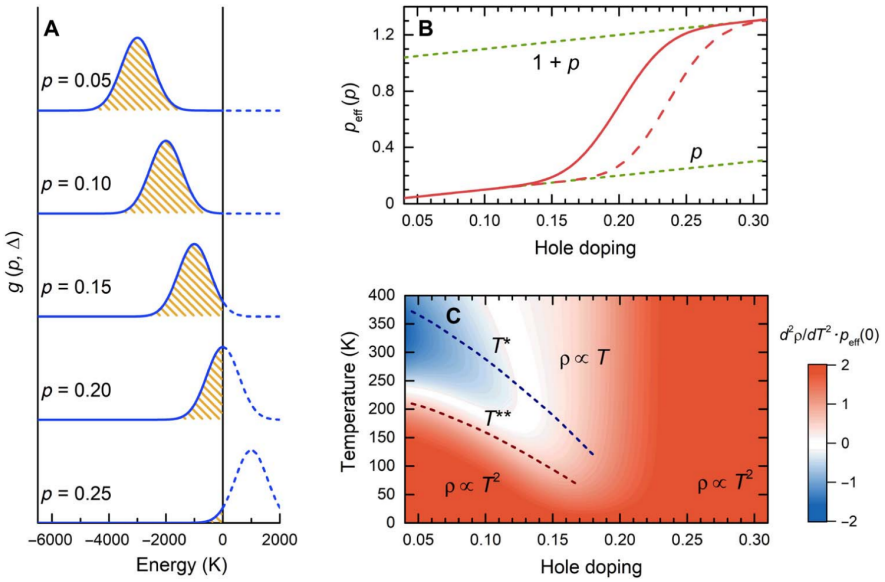

Figure 5.1: Heterogeneous charge localization model, reproduced from [120]. (A) Gaussian gap distribution function g at several doping levels. The energy scale is represented in temperature units (K). (B) Effective density p_{eff} of carriers per CuO_2 unit at $T = 0$, obtained as the sum of the doped hole concentration p and the delocalized holes from the distribution shown in (A). The dashed line corresponds to a slightly different distribution than in (A) that best describes charge-transport data for LSCO. (C) Second derivative of the normal-state resistivity, multiplied by p_{eff} at $T = 0$. The characteristic features of the phase diagram include quadratic resistive regimes at both low and high doping, the pseudogap temperatures T^{**} and T^{*}, and the linear-T-like regime around optimal doping.

range from the insulator to the FL metal ($0 \leqslant x \leqslant 0.34$) [205], as shown in Figure 5.2. The parent compound La_2CuO_4 is a charge-transfer (CT) insulator, with a CT gap in the 1-2 eV range. Upon doping, spectral weight is transferred from above the CT gap to a Drude peak, and to a broad peak in the mid-infrared range (at ~ 0.5 eV for $x = 0.02$), and a near-infrared peak at ~ 1.5 eV. The broad mid-infrared peak decreases in energy with increasing doping (Figure 5.2) and corresponds to the gap Δ of the phenomenological model (Figure 5.1). Remarkably, the spectral weight integrated to ~ 2.5 eV, just above the CT gap, approaches $1 + p$ for all doping levels [126].

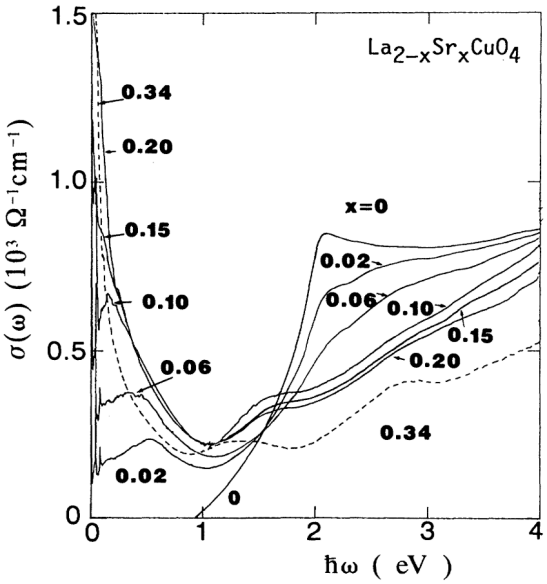

Figure 5.2: Room-temperature planar optical conductivity for LSCO ($0 \leqslant x \leqslant 0.34$), reproduced from [205].

The doping dependence of CT excitations has also been systematically studied in LSCO via Cu K-edge RIXS, as shown in Figure 5.3 [217]. Similar to the observations from optical conductivity, the CT gap was observed around 2 eV in the undoped compound, and the spectral intensity below the CT gap was found to increase upon hole doping. It was also demonstrated that the spectral weight transfer from high energy ($>$ 2 eV) to lower energy (1-2 eV) is most pronounced at the zone boundary $\boldsymbol{q} = (0.5, 0)$ and nearly linear in x.

On the other hand, the temperature dependence of the CT excitations is usually

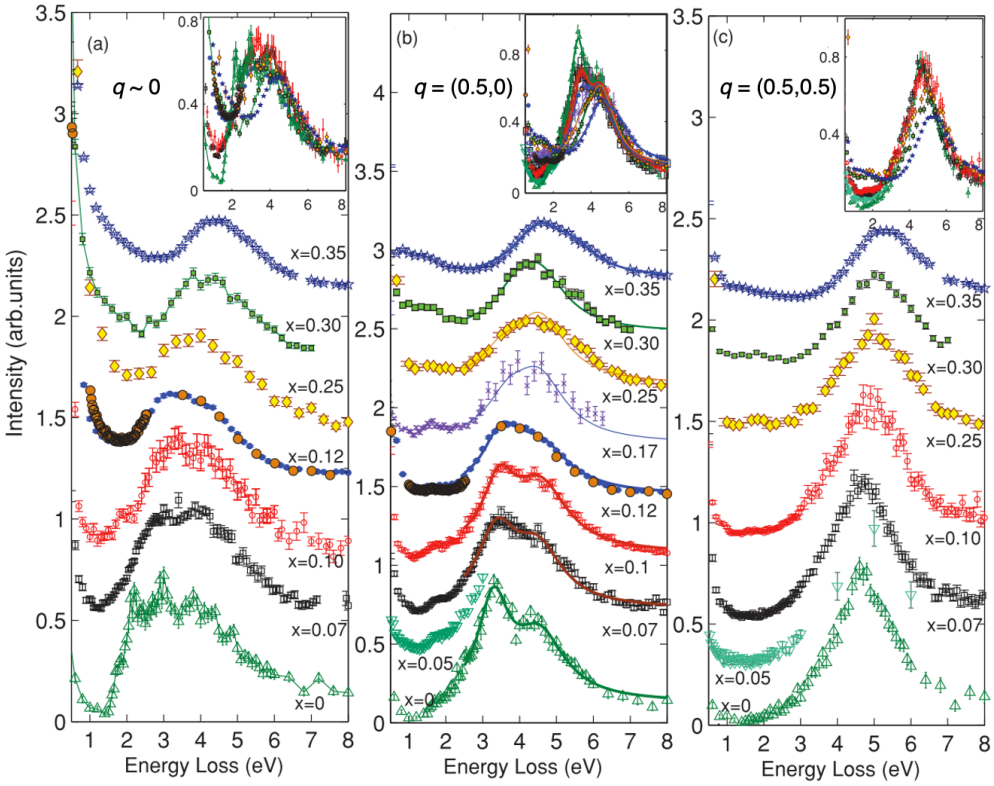

Figure 5.3: Doping-dependent Cu K-edge RIXS spectra for LSCO at different momentum transfers: (a) $\boldsymbol{q} \sim 0$, (b) $\boldsymbol{q} = (0.5, 0)$, and (c) $\boldsymbol{q} = (0.5, 0.5)$, adapted from [217]. The curves are vertically shifted for clarity, and the doping levels x are indicated for each spectrum. Inset: combined, unshifted curves overlayed with each other. All data were normalized at 10 eV.

studied only up to room temperature [205–218], which is a very low temperature scale given the large CT energy scale. Therefore, high-temperature measurements close to the decomposition point of the material are highly desirable.

5.2 Experimental Procedure

We performed a Cu K-edge RIXS study of the archetypal hole-doped cuprate LSCO and of the electron-doped cuprate NCCO. RIXS is capable of measuring element-specific electronic excitations. At the Cu K-edge, core-level electrons undergo the transition $1s \rightarrow 4p$, leaving a hole in the core level. In the intermediate state, the $3d$ electrons interact with the $1s$ core hole, causing charge-transfer excitations in the $3d$ band. Unlike optical conductivity measurements, which correspond to a correlated average over the Brillouin zone at effectively zero momentum transfer ($q = 0$), RIXS allows access to particle-hole excitations throughout the entire Brillouin zone and thus can provide valuable energy- and momentum-dependent information. In this Chapter, we follow standard RIXS notation and denote the incident photon energy as E_i; this notation differs from that in Chapter 2.

Since our goal was to measure to high temperatures, the studied materials were required to be chemically stable at these temperatures. As-grown LSCO and NCCO samples are usually subjected to an anneal process at ~ 1100 K to remove thermal stress (in both cases) and to induce superconductivity (in the case of NCCO), so meaningful experiments should be doable up to this temperature. In addition, it has proven possible to reproducibly obtain charge transport data up to at least 1000 K [219]. Nevertheless, prior to our high-temperature RIXS measurements, we performed a heat-treatment study to ensure sample stability.

5.2.1 Heat-Treatment Study

In order to ensure sample stability, a sequence of heat-treatment tests were carried out, i.e., crystals were heated at high temperatures in air at atmospheric pressure for a prolonged period of time, and the bulk superconducting properties were measured both before and after the heat treatment to ensure the robustness of the sample. Figure 5.4 shows SQUID magnetization measurements of a superconducting LSCO $x = 0.07$ sample

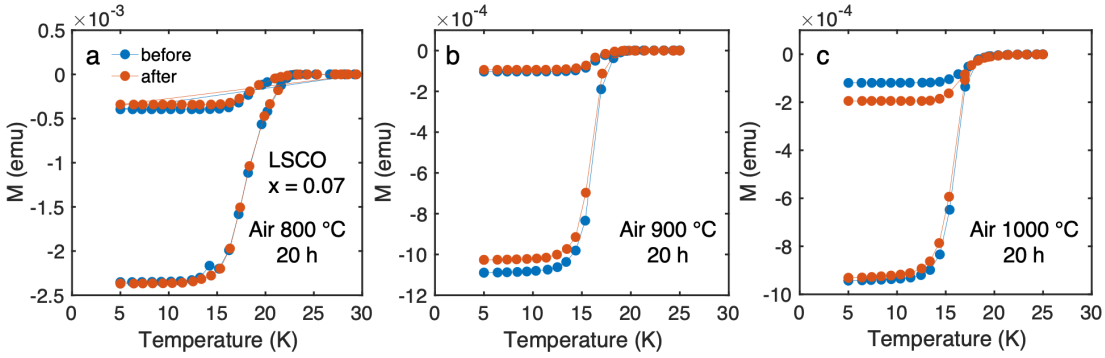

Figure 5.4: Heat treatment of a LSCO $x = 0.07$ sample at (a) 800 °C, (b) 900 °C and (c) 1000 °C for 20 hours in air at atmospheric pressure leaves the bulk superconducting properties unaffected. No significant changes in the field-cooled/zero-field-cooled diamagnetic response are discernible.

upon cycling to high temperatures. The same sample was kept at 800 °C, 900 °C and 1000 °C in air at atmospheric pressure for nearly one day (the typical RIXS measurement time at each temperature). No significant changes in the field-cooled/zero-field-cooled diamagnetic response were discernible.

In addition, during the RIXS measurement, we confirmed that the RIXS spectra remained the same before and after high-temperature measurements. Figure 5.5 shows RIXS spectra (obtained with incident photon energy $E_i = 8991.3$ eV) for a LSCO $x = 0.07$ sample at 450 K before and after having been measured at 1000 K for more than one day. No significant changes are discernible, indicative of a high level of sample stability.

A similar heat-treatment study was performed for NCCO. It was found that NCCO is stable in air up to 800 °C. Higher temperatures resulted in a lower T_c and a broader superconducting transition.

5.2.2 Cu K-edge RIXS

The RIXS measurements of LSCO and NCCO were carried out at the BL11XU beamline of SPring-8 and the ID-27-C beamline of the Advanced Photon Source (APS). The scattering geometry for all RIXS measurements is schematically shown in Figure 5.6(a). The scattering plane is the ac-plane of the crystal lattice in tetragonal notation. Due to

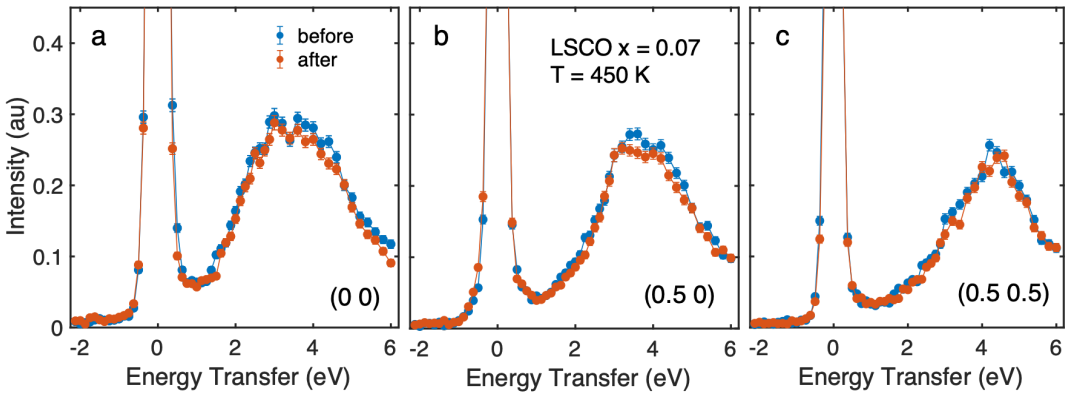

Figure 5.5: Cu K-edge RIXS spectra for a LSCO $x = 0.07$ sample at (a) (0, 0), (b) (0.5, 0) and (c) (0.5 0.5) measured at 450 K before and after a measurement at 1000 K that lasted more than one day. No significant changes are observed.

the quasi-2D nature of the cuprates, the L dependence of the cross section is expected to be small, if not negligible, so we quote the 2D reduced wave vector $\boldsymbol{q} = (H, K)$. The RIXS measurements were performed along both nodal $[H, H]$ and anti-nodal $[H, 0]$ directions. In order to better access low-energy excitations, we kept the scattering angle 2θ at $\sim 90^\circ$ (by adjusting L) to reduce the elastic scattering component. The overall energy resolution was 250 meV at SPring-8 and 100 meV at the APS, respectively. High temperatures were achieved with either a custom-designed high-temperature furnace or a commercially available Linkam stage.

We studied a number of LSCO and NCCO samples between zero ($x = 0$) and optimal ($x = 0.15$) doping. All crystals were cut into square shapes with the c-axis normal to the surface. All NCCO samples and the LSCO $x = 0.02$ sample were initially annealed in reduced atmosphere to remove excess oxygen. The superconducting LSCO samples ($x = 0.07, 0.125, 0.15$) were annealed in air at 800 °C for 40 hours to reduce thermal stress. Table 5.1 summarizes all the samples and corresponding experimental conditions used in this study.

X-ray absorption spectroscopy (XAS) measurements were subsequently carried out to check the resonant energy for each sample. Figure 5.6(b) and (c) shows the XAS results for LSCO and NCCO, respectively. Since the XAS features are only slightly doping-dependent, we used the same incident photon energy (E_i) for all samples. For

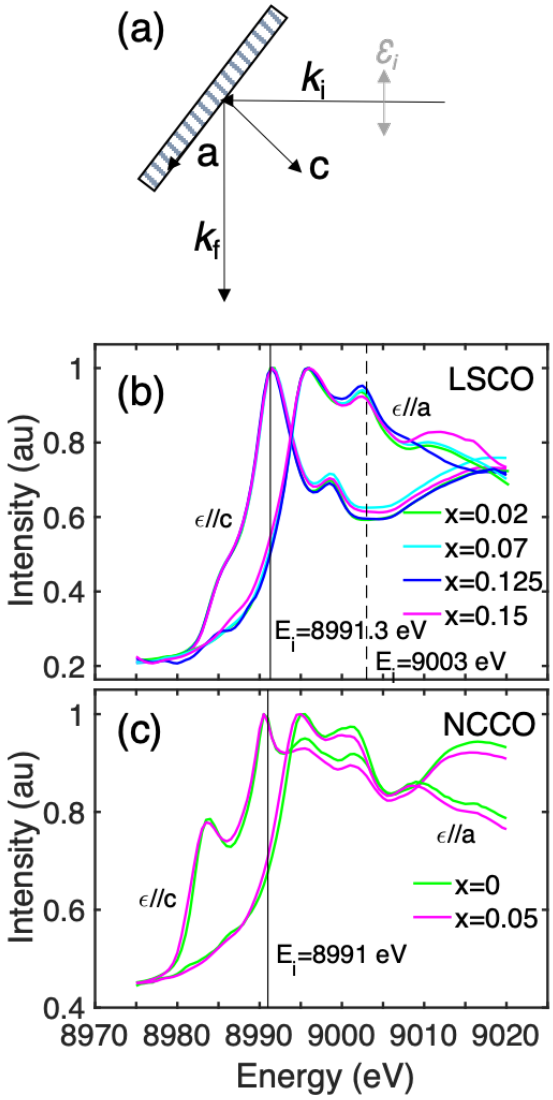

Figure 5.6: Cu K-edge RIXS setup and XAS measurements. (a) Scattering geometry used in the present study, where **a** and **c** denote the lattice axes in tetragonal notation. The scattering angle 2θ was kept at 90° by adjusting the L value to ensure that the scattered photon direction was parallel to the incident photon polarization ϵ. (b) X-ray absorption spectroscopy (XAS) spectra for (a) LSCO and (b) NCCO. XAS was measured under two different conditions: $\epsilon//a$ and $\epsilon//c$. The vertical lines indicate the incident energies E_i = 8991.3 eV and E_i = 9003 eV for LSCO and E_i = 8991 eV for NCCO.

measurements of LSCO, E_i was either 8991.3 eV or 9003 eV, whereas for NCCO, a slightly lower value of $E_i \sim 8991$ eV was used.

Composition	x	E_i (eV)	Temperature (K)
LSCO	0.02	8991.3	15-1000
LSCO	0.07	8991.3	15-1000
LSCO	0.125	9003	300 - 1200
LSCO	0.15	9003	300 - 1200
NCCO	0	8991	10 - 400
NCCO	0.05	8991	10 - 400
NCCO	0.13	8991	300 - 800
NCCO	0.16	8991	10 - 400

Table 5.1: Table of samples measured in this RIXS study. Listed from left to right: sample composition (LSCO or NCCO), dopant concentration x, incident X-ray energy E_i (eV), and the studied temperature range (K).

The synchrotron radiation experiments of LSCO and NCCO ($x = 0, 0.05, 0.16$) were performed at the BL11XU of SPring-8 with the approval of the Japan Synchrotron Radiation Research Institute (JASRI) (Proposal No. 2016B3552, 2017A3552, and 2017B3552). The measurements of NCCO ($x = 0.13$) were carried out at ID-27-C beamline of Advanced Photon Source (APS), Argonne National Laboratory.

5.3 Results

5.3.1 LSCO measurements with $E_i = 8991.3$ eV

Figure 5.7 shows RIXS spectra for a LSCO $x = 0.02$ sample, measured along $[H, 0]$ and $[H, H]$ with $E_i = 8991.3$ eV, over a wide temperature range (15 K - 1000 K). The spectra were normalized at 6 eV.

In the $\boldsymbol{q} = (0, 0)$ spectra shown in Figure 5.7(a), a sharp peak at 2.2 eV was observed at $T = 15$ K, and the intensity of the peak was found to decrease significantly upon heating. Similar behavior was observed in a prior doping-dependence study (Figure 5.3) [217] performed at $T = 25$ K, where this peak was seen to dramatically decrease with increasing doping. Interestingly, this peak is found to be associated with disorder, as it decreases in Ni-doped samples as well (the Ni dopants act as magnetic impurities

and are thought not to introduce charge carriers) [217].

Along $[H, 0]$, a prominent peak at ~ 3.3 eV is present at $T = 15$ K at all momenta (Figure 5.7 (a)-(c)). The intensity of this peak decreases as well from 15 K to 1000 K. Unlike the doping dependence, where a clear spectral weight transfer from high to low (< 2 eV) energy is observed (Figure 5.3) [217], the temperature dependence below 2 eV is overall subtle. Nevertheless, a clear effect is seen at the zone center. Another broad peak at ~ 4.5 eV is observed at $\boldsymbol{q} = (0.5, 0)$ at $T = 15$ K. This peak merges with the ~ 3.3 eV peak above 350 K, and only one broad peak is observed at high temperatures. The temperature dependence of these features is highlighted in Figure 5.8, which highlights the net intensity change compared to 1000 K.

As shown in Figure 5.7 (a), (d)-(e), away from $\boldsymbol{q} = (0, 0)$, the spectra only feature one peak along $[H, H]$. At (0.25,0.25) and 15 K, the peak is located at ~ 4 eV, and it slightly shifts to lower energies at higher temperatures. This effect is more pronounced at (0.5,0.5). As a result of the shift, the spectral weight below 4 eV monotonically increases with increasing temperature.

Figures 5.9 and 5.10 show the same measurements for a LSCO sample with a higher doping level of $x = 0.07$. The sharp peak at 2.2 eV observed at $q = (0, 0)$ for the $x = 0.02$ sample is absent in the $x = 0.07$ sample. Instead, a small intensity enhancement around ~ 2.7 eV is observed at low temperature. Overall, the temperature dependence of the RIXS spectra is quite similar to that for $x = 0.02$ at all the measured momenta.

In order to quantify the temperature dependence, the spectral weight in the energy ranges 0.75-1.75 eV, 2-4 eV, and 3.5-5.5 eV is shown in Figure 5.11 (a) and (b) for $\boldsymbol{q} = (0, 0)$ and (0.5,0.5), respectively. At the zone center, for $x = 0.07$, the intensity in the intermediate-energy range 0.75-1.75 eV remains the same even at the highest measured temperature, whereas for $x = 0.02$ a slight intensity enhancement is observed at 700 K and 1000 K. For both doping levels, the spectral weight significantly decreases upon heating in the 2-4 eV range. For 3.5-5.5 eV, it remains almost the same up to 750 K, and a slight decrease is observed at 1000 K. Different behavior is observed at (0.5,0.5): the integrated intensity in the ranges 0.75-1.75 eV and 3.5-5.5 eV is almost temperature independent, whereas it monotonically increases for 2-4 eV. In addition, the leading edge of the peak observed at (0.25,0.25) and (0.5,0.5) are shown in Figure 5.11 (c) and (d). The leading edge is determined as the energy at which the intensity is the

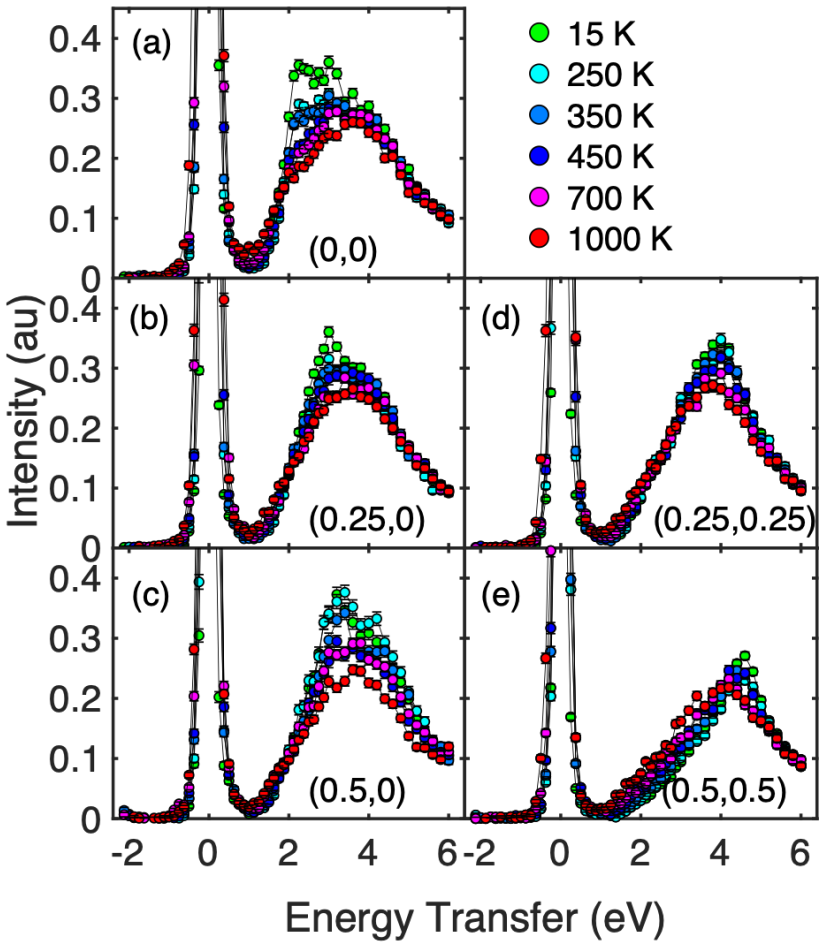

Figure 5.7: RIXS spectra for LSCO ($x = 0.02$) at (a) (0,0), (b) (0.25,0), (c) (0.5,0), (d) (0.25,0.25), and (e) (0.5,0.5), measured with $E_i = 8991.3$ eV. Data were obtained from base temperature (15 K) to high temperature (1000 K). The spectra were normalized at 6 eV.

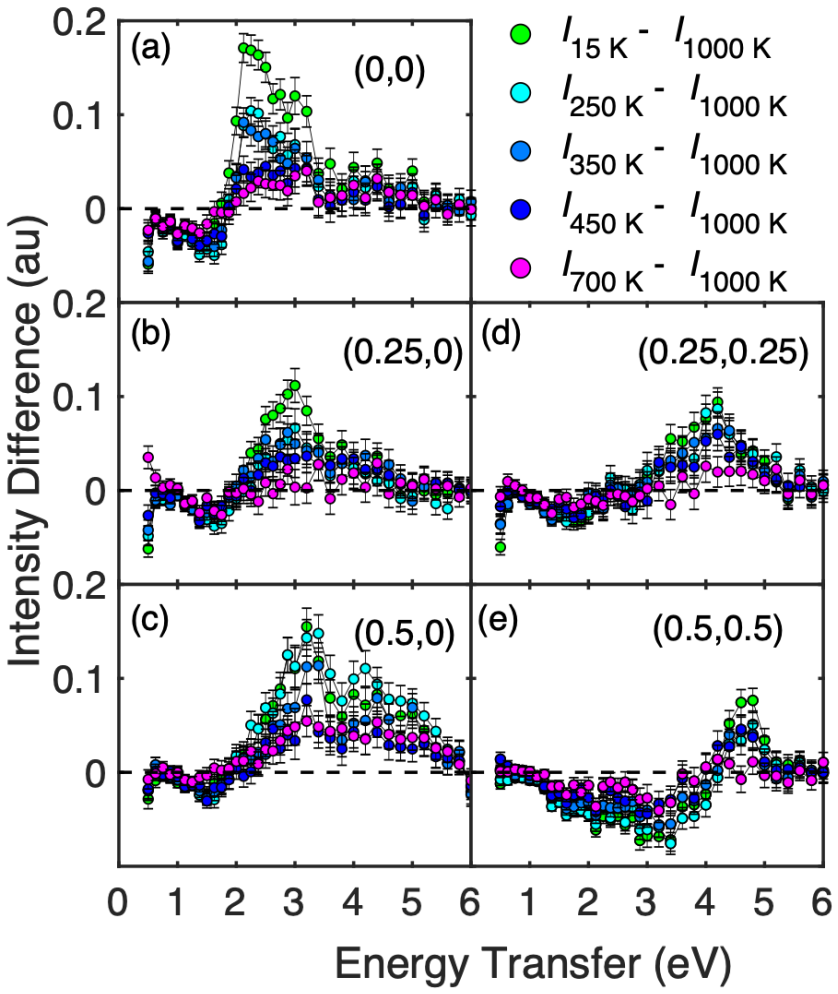

Figure 5.8: Net RIXS intensity for LSCO ($x = 0.02$) after subtracting the 1000 K spectra at (a) (0,0), (b) (0.25,0), (c) (0.5,0), (d) (0.25,0.25), and (e) (0.5,0.5). Horizontal dashed lines indicate zero difference. The data are those shown in Figure 5.7, obtained with $E_i = 8991.3$ eV. The intensity difference could only be reliably established above ~ 0.5 eV.

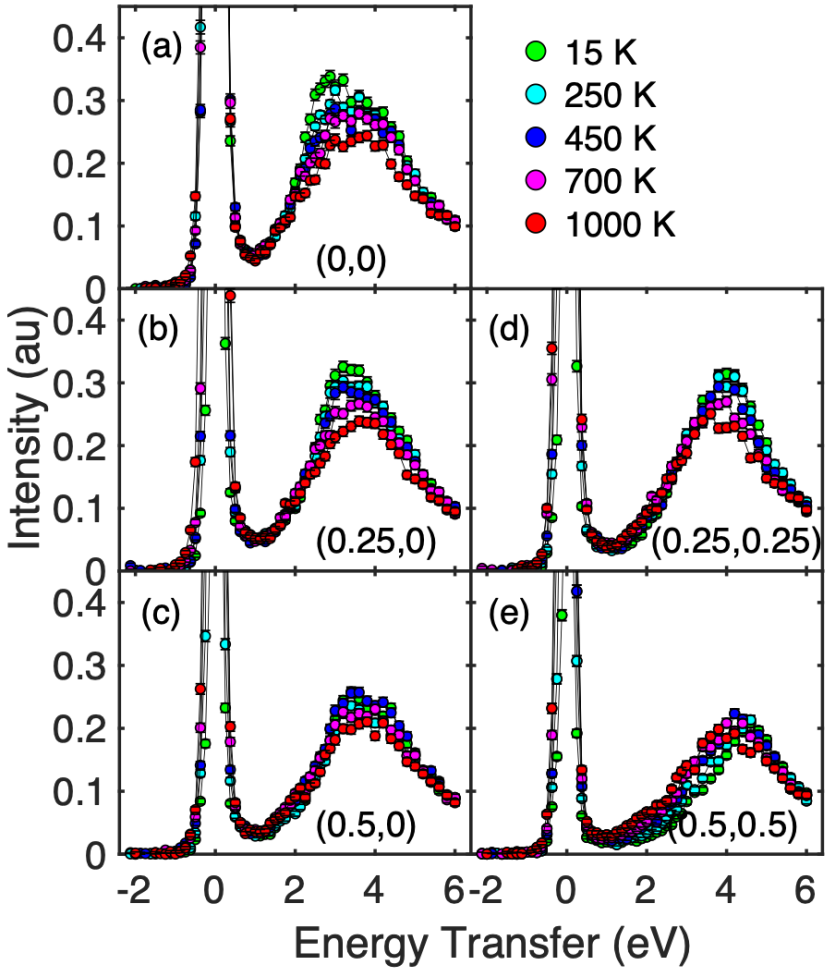

Figure 5.9: RIXS spectra for LSCO $x = 0.07$ at (a) (0,0), (b) (0.25,0), (c) (0.5,0), (d) (0.25,0.25) and (e) (0.5,0.5), measured with $E_i = 8991.3$ eV. Data were obtained from base temperature (15 K) to high temperature (1000 K). The spectra were normalized at 6 eV.

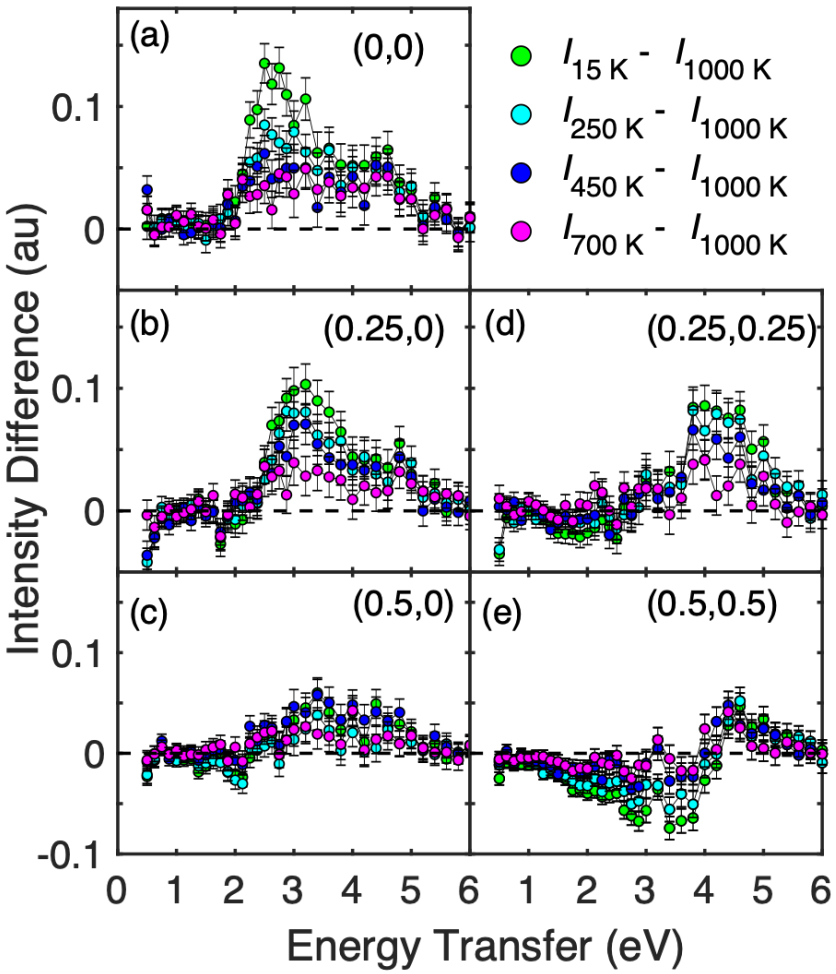

Figure 5.10: Net RIXS intensity for LSCO ($x = 0.07$) after subtracting the 1000 K spectra at (a) (0,0), (b) (0.25,0), (c) (0.5,0), (d) (0.25,0.25), and (e) (0.5,0.5). Horizontal dashed lines indicate zero difference. The data are those shown in Figure 5.9, obtained with $E_i = 8991.3$ eV. The intensity difference could only be reliably established above ~ 0.5 eV.

half of the peak intensity. A significant redshift is observed at (0.5,0.5) for both doping levels. An interesting question, to be addressed in future research, is how the changes seen at the antiferromagnetic wavevector (0.5,0.5) are associated with the build-up of spin correlations with decreasing temperature [192]. Furthermore, in order to better connect with optical spectroscopy work (in particular, the mid-infrared feature and the Drude peak, see Figure 5.2), RIXS data with improved energy resolution are required.

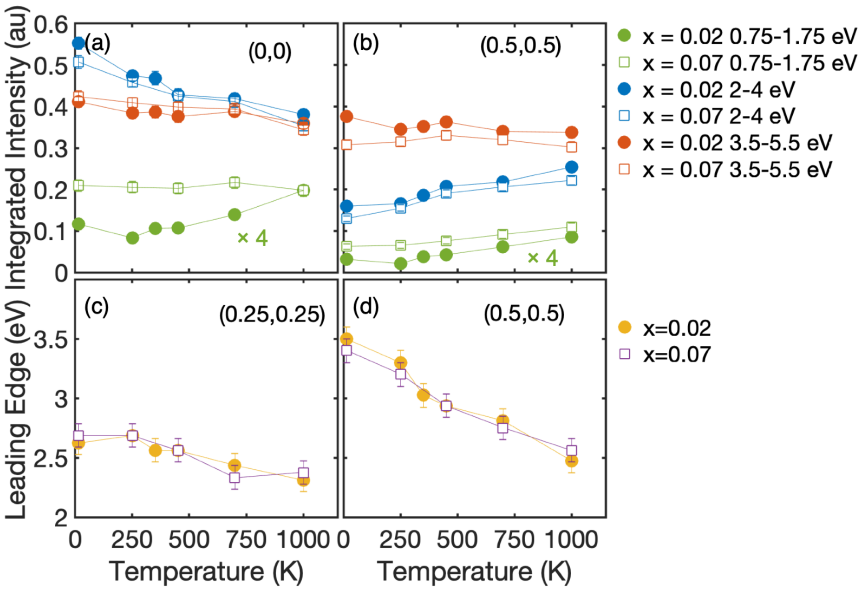

Figure 5.11: Temperature dependence of the spectral weight at (a) (0,0) and (b) (0.5,0.5) in the energy ranges 0.75-1.75 eV (green, multiplied by a factor of 4), 2-4 eV (blue) and 3.5-5.5 eV (red). Shifts of the leading edge for (c) (0.25,0.25) and (d) (0.5,0.5). The leading edge is defined as the energy transfer at which the intensity is half of the peak intensity.

5.3.2 LSCO measurements with $E_i = 9003$ eV

The first RIXS observation of intraband excitations below the CT gap in the cuprates was for electron-doped NCCO [220]. It was suggested that, when the incident X-ray energy is tuned to transitions into orbitals in which doped electrons/holes are located, intraband excitations become dominant in RIXS spectra [221]. In the electron-doped system, this incident energy is located slightly below the well-screened condition (the

$1s$ core-hole potential is well-screened by the doped $3d$ electrons), whereas in the hole-doped case, it is located slightly above the poorly-screened condition (the $1s$ core-hole is poorly screened due to the the doped holes in the $3d$ orbitals). It was found that this resonance energy is ~ 9003 eV in hole-doped systems, and intraband excitations below ~ 3 eV were successfully probed in overdoped LSCO and $Bi_{1.76}Pb_{0.35}Sr_{1.89}CuO_{6+\delta}$ [218].

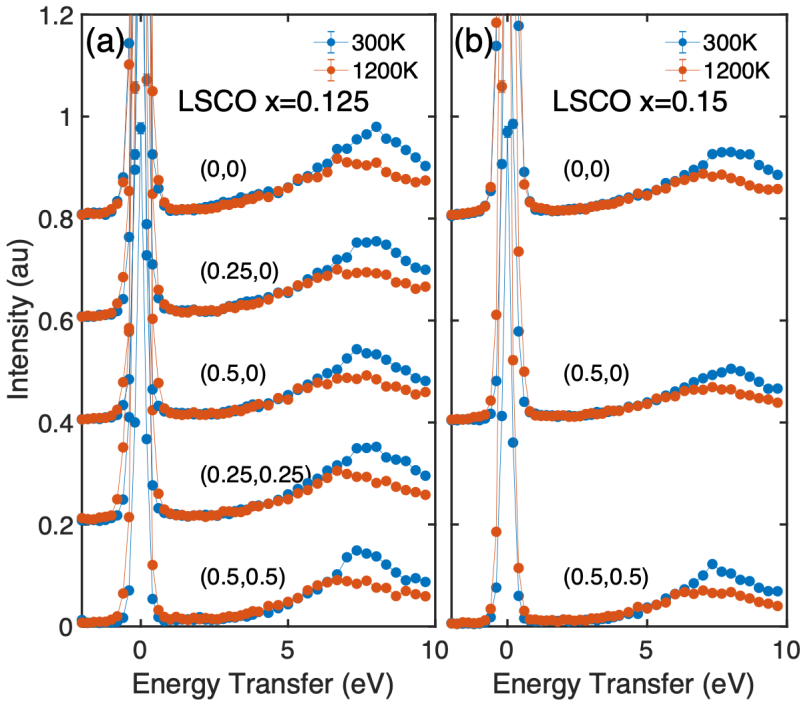

Figure 5.12: RIXS spectra for LSCO (a) $x = 0.125$ and (b) $x = 0.15$ with $E_i = 9003$ eV. The data are vertically shifted for clariety. The measured momentum is noted for each spectrum. Note that no normalization is applied.

Since the intraband excitations are expected to be more pronounced at higher carrier densities (the $1s$ core-hole potential is less screened), two LSCO samples with intermediate ($x = 0.125$) and optimal ($x = 0.15$) doping levels were studied. Figure 5.12 shows the RIXS spectra with $E_i = 9003$ eV. Since the intensity completely recovers at 300 K after cycling to 1200 K, the data are not normalized. The CT peak in the 8991.3 eV data (not measured in present study, but available in [218] and [217] for similar doping levels), which disperses from 4 to 5 eV at all momenta, is replaced by a peak around

7 eV in the 9003 eV data. This excitation is attributed to the molecular-orbital (MO) excitation [222]: due to the hybridization between the Cu $3d_{x^2-y^2}$ level and the O $2p$ level, the bonding and anti-bonding hybridized d molecular orbitals are non-degenerate. This MO peak softens at 1200 K because of the lattice expansion at high temperature. However, the low-energy part (< 5 eV) of the RIXS spectra remains the same at 300 K and 1200 K. Therefore, no thermally excited intraband excitations are observed in LSCO $x = 0.125$ and 0.15.

5.3.3 NCCO measurements with $E_i = 8991$ eV

Although similar CT excitation energies of ~ 2 eV were observed for LSCO and NCCO, quite different momentum dependences were reported [216, 218, 220]. In LSCO, the RIXS spectral shape is almost the same at different momentum transfers except for small shifts in energy, whereas in NCCO, a sharp CT peak at 2 eV is observed at the zone center and found to broaden in energy with increasing momentum transfer [220]. It was suggested theoretically that the strength of the antiferromagnetic correlations plays a crucial role in the latter case [223]. For NCCO, the doping and temperature dependence of the antiferromagnetic correlations has been determined in detail via neutron scattering [224, 225]. Even at optimal doping, antiferromagnetic correlations are still significant, with a correlation length of $\xi/a \sim$ 15-20 [224, 225]. We performed a RIXS study of reduced NCCO to monitor changes in the charge-transfer response as antiferromagnetic correlations decrease with increasing temperature and increasing doping.

Figure 5.13 shows the RIXS spectra for NCCO with $E_i = 8991$ eV. Three NCCO samples were measured at 10 K and 400 K: undoped $x = 0$, underdoped $x = 0.05$ and optimally-doped $x = 0.16$. At 10 K, only the $x = 0$ and $x = 0.05$ samples are in Néel state, whereas the $x = 0.16$ sample is in the superconducting state and features a correlation length of $\xi/a \sim$ 15-20. At 400 K, short-range antiferromagnetic correlations persists in the $x = 0$ and $x = 0.05$ samples, with $\xi/a \sim$ 15-20, whereas in the case of the $x = 0.16$ sample, the correlation length is well below 10 lattice constants. Similar to prior RIXS measurements [220,226], the CT peak around 2 eV is observed and found to slightly shift toward higher energy at higher doping levels. The peak is sharpest at the zone center and broadens on approaching the zone boundary. Interestingly, at 400

K, an intensity enhancement below the CT gap is observed at $\boldsymbol{q} = (0, 0)$, especially for the doped samples.

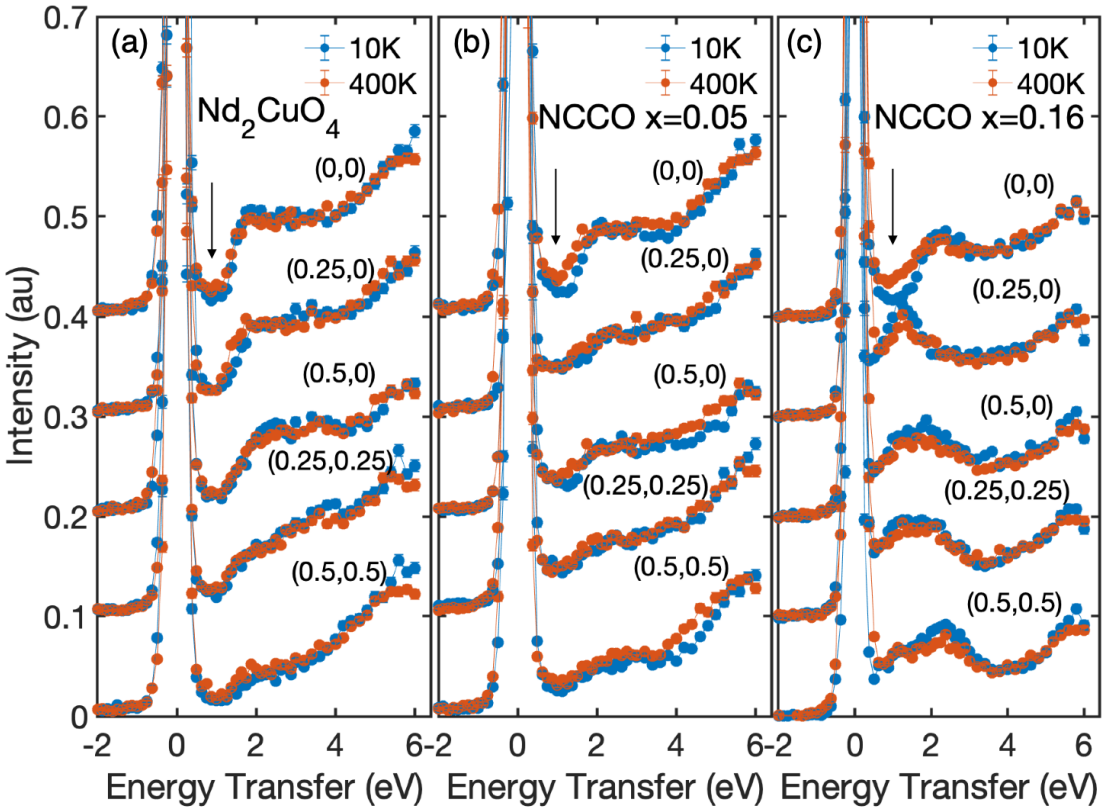

Figure 5.13: RIXS spectra for NCCO with (a) $x = 0$, (b) $x = 0.05$, and (c) $x = 0.15$, measured at 10 K and 400 K with $E_i = 8991$ eV. The spectra were normalized at 6 eV. The arrows indicate an intensity enhancement below the charge-transfer gap at 400 K for the zone-center data. All samples were annealed in Ar flow (at 800 °C for $x = 0$ and 900 °C for $x = 0.05$ and $x = 0.16$) for 10 hours prior to the experiment.

In order to further study the evolution of this spectral weight change, we performed a detailed temperature-dependent measurement of a NCCO $x = 0.13$ sample (Figure 5.14). The spectra were normalized at 6 eV. The spectral weight below the CT gap was estimated by integrating intensity in the 0.5-2 eV range. A significant effect is seen at the zone center, where the intensity increases monotonically from 300 K to 800 K. On the other hand, no significant temperature dependence is discerned at the other

momenta.

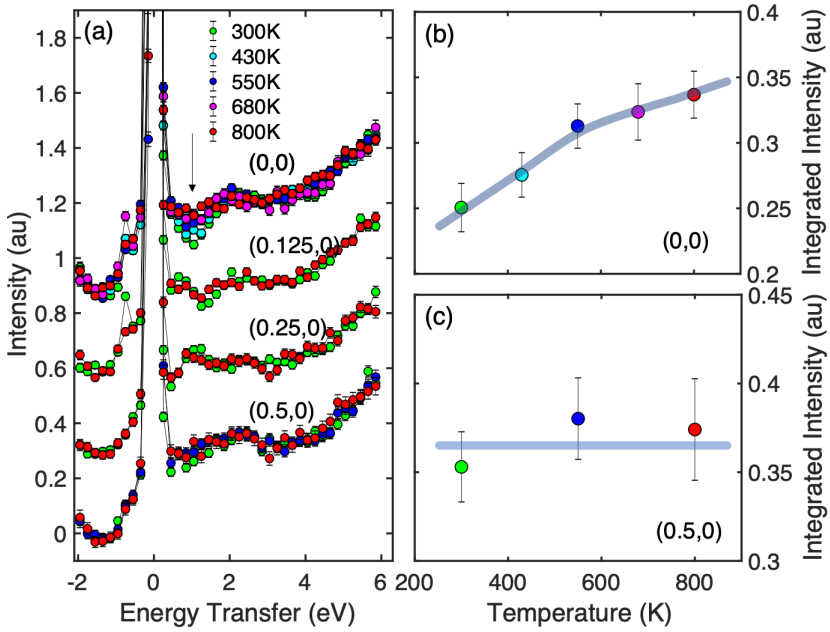

Figure 5.14: (a) RIXS spectra for NCCO (x = 0.13) with $E_i = 8991$ eV measured from 300 K to 800 K. The spectra were normalized at 6 eV. Temperature dependence of the integrated intensity between 0.5-2 eV at (b) (0,0) and (c) (0.5,0). The solid lines are guides to the eye.

5.4 Discussion

In the case of LSCO, both optical conductivity and RIXS measurements reveal a spectral weight transfer from the CT gap $\sim$ 2 eV to lower energy ($\sim$ 0-1.5 eV) with increasing doping [205, 217, 218] (see Figures 5.2 and 5.3). The study of the CT excitations presented in this Chapter reveals an overall spectral weight loss above $\sim$ 2 eV with increasing temperature for both $x = 0.02$ and $x = 0.07$. For $x = 0.07$, the intensity in the intermediate-energy range 0.75-1.75 eV remains the same even at the highest measured temperature. For $x = 0.02$, on the other hand, a clear intensity enhancement is seen in this range that is most prominent at the zone center. For electron-doped

NCCO, an intensity enhancement around ~ 1 eV is clearly discernible at the zone center with increasing temperature, although no spectral weight transfer is observed. Our results for LSCO somewhat suggest dissimilar doping and temperature dependences of the CT excitations in the cuprates. Below, I consider several possible reasons for this discrepancy.

First, the optical conductivity study of LSCO shows that the spectral weight above the CT gap is mostly transferred to a 'hump' that moves toward low energy and to the Drude peak that increases in strength with increasing doping (Figure 5.2) [205]. The broad hump is seen to merge with the coherent quasiparticle (Drude) peak near optimal doping. This feature is observed around ~ 0.6 eV for $x = 0.02$, and its energy decreases approximately linearly with increasing doping [120, 205]. Considering Figure 5.2 and the model of [120], the main changes in RIXS intensity with temperature (at least at the zone center) are in fact expected below ~ 1.5 eV for $x = 0.02$ and below ~ 0.5 eV for $x = 0.07$ and larger doping levels. This is not inconsistent with our data. Given our energy resolution of 0.25 eV, and the contribution of phonon excitations to the low-energy response, our experiment is not sensitive to changes below ~ 0.6 eV. Therefore, temperature-induced changes are probably hidden in the quasi-elastic range and not resolvable in the present study.

Second, although a measurement of the low-energy excitations (< 0.6 eV) is not possible with the present energy resolution, a near-infrared intensity enhancement may be expected at high temperatures, since a peak at ~ 1.5 eV is present at higher doping levels in the optical data (Figure 5.2) [205]. For LSCO, upon both heating and doping, the high energy RIXS spectral weight (> 2 eV) decreases significantly, whereas the lower-energy signal is expected to increase. The two effects might cancel out in the near-infrared regime, resulting in a temperature-independent intensity.

Third, it is known that the RIXS response is highly dependent on the incident photon energy (E_i): even a small ~ 0.5 eV change in incident energy may cause considerable changes in the RIXS intensity [215, 227]. Although in our experiment the incident photon energy was always calibrated at room temperature using XAS (Figure 5.6) prior to the RIXS measurement, a small energy shift after several days of measurement is possible. Moreover, we kept the same E_i at all temperatures, and it is possible that the resonant energy effectively changes at these high temperatures due to lattice expansion,

which needs to be taken into account in future studies.

Fourth, the electronic structure of the doped cuprates is not fully understood. Importantly, there exist considerable differences in the doping-dependent CT excitations probed by optical conductivity and Cu K-edge RIXS [205, 217, 218]. Finally, we note that the heterogeneous charge (de)localization model, which partially motivated the present RIXS study, is phenomenological in nature. We hope that the present investigation the temperature dependence of CT excitations will not only serve to motivate future RIXS measurements with improved energy resolution, but also to inspire refined theoretical work on the electronic structure of the cuprates.

Chapter 6

XAS/XMCD Study of Ion-gel-gated $La_{0.5}Sr_{0.5}CoO_{3-\delta}$

Electrolyte-based transistors utilizing ionic liquids/gels have been highly successful in the study of charge-density-controlled phenomena in diverse materials, particularly oxides. Experimental probes beyond electronic transport have played a significant role, despite challenges to their application in the electric double-layer transistor geometry. In this Chapter, I demonstrate the application of synchrotron *soft* X-ray absorption spectroscopy (XAS) and X-ray magnetic circular dichroism (XMCD) as *operando* probes of the charge state and magnetism in ion-gel-gated ferromagnetic perovskite thin film $LaAlO_3(001)/La_{0.5}Sr_{0.5}CoO_{3-\delta}$ (LSCoO).

6.1 Introduction

Electric double-layer transistors (EDLTs) employing ionic liquids/gels have proven successful in the study of charge-density-dependent effects in many materials [32–35]. This approach allows the density of doped carriers to be varied in a single device, to extremely high charge densities ($> 10^{14}$ cm^{-2}) [32–36, 41, 43, 44, 46–48, 228–230], at least an order of magnitude above conventional (e.g., SiO_2-based) field-effect devices. EDLTs are thus widely used to study electronic and magnetic phase transitions [32–39,41,43–48,228–230] and map phase diagrams [37, 228]. For instance, electrically-induced superconductivity was observed in electrolyte-gated $KTaO_3$ [43], $SrTiO_3$ [44], and high-temperature

superconductors [33, 36–39]. Control of the insulator-metal transition was achieved in VO_2 [54, 229, 231, 232] and nickelates [47, 230], and modulation of magnetism was found possible in $Ti_{1-x}Co_xO_2$ [48], $La_{1-x}Sr_xMnO_3$ [41, 233], and $La_{1-x}Sr_xCoO_{3-\delta}$ [52, 59, 64].

It is increasingly recognized that EDLT operating mechanisms are typically not purely electrostatic, and that there exist a range of alternative responses [34, 49–52, 54, 59, 64, 231]. In oxides, for example, the gate response can be electrochemical, where the EDLT electric field induces redox chemistry, often via oxygen vacancy (V_O) formation/annihilation. Evidence for this originally came from transport measurements in controlled atmosphere, with tracking of irreversibility [52, 53, 55–58]. Recently, however, synchrotron-based hard X-ray diffraction [59–62] and hard XAS [60, 63], as well as neutron reflectometry [59, 64] have been developed as *operando* probes of EDLTs, complementing transport. Our recent *operando* X-ray diffraction measurements of ion-gel-gated $La_{0.5}Sr_{0.5}CoO_{3-\delta}$ (LSCoO) highlighted the importance of gate-bias polarity: a large lattice expansion was found at positive gate bias (V_g) due to V_O formation, whereas only minor structural changes occurred at negative V_g [59]. Importantly, the V_g-induced V_O penetrated the entire film thickness, confirmed by depth-sensitive neutron reflectometry; this is enabled by the high diffusivity of V_O in LSCoO, which has led to much attention on redox control of these compounds [52, 59, 62, 64, 234, 235].

Although application of EDLTs is growing, an element-sensitive *operando* probe such as XAS, which enables element-specific determination of valence, has not been fully developed. Some absorption spectroscopy studies in the hard X-ray regime [60, 63] provided insights into EDLT gating mechanisms, but *soft* XAS at the O K and transition-metal L edges, which directly probes transition-metal electronic/magnetic structure, has not yet been performed in an *operando* fashion. The main challenges in such measurements (as opposed to *ex-situ* studies of non-volatile gate effects) include penetrating thick electrolyte layers with soft X-rays and getting absorption signals out.

In this Chapter, I establish soft XAS and XMCD, its magnetic variant, as *operando* probes of the charge state and magnetism in electrolyte-gated (specifically ion-gel-gated) epitaxial LSCoO films. Baseline information is first gathered from 4-25 unit-cell-thick bare films by determining the evolution in hole doping from O K edge XAS and in ferromagnetism from Co L edge XMCD. The ion gel (i.e., ionic liquid in a polymer network) used for *operando* measurements was optimized in terms of thickness (to ~ 1

μm) and composition. We show that, upon applying $V_g = +4$ V, the O K edge XAS prepeak intensity is strongly suppressed, indicating a substantial decrease in effective hole density. Concomitantly, the Co magnetic moment is substantially reduced, as revealed in energy- and magnetic-field-dependent XMCD. These results, which complement prior X-ray diffraction and neutron reflectometry work [59,64], not only yield new insight into gating mechanisms in oxide EDLTs, but also demonstrate a powerful element-sensitive approach to *operando* studies of gated oxides.

6.2 Experimental Procedure

6.2.1 Device

As described previously [52], epitaxial LSCoO films were grown using high-pressure-oxygen reactive sputtering in 1.4 Torr of O_2 from ceramic LSCoO targets onto 10×10 mm^2 $LaAlO_3(001)$ substrates at 600 °C. Extensive structural, chemical, magnetic and transport characterization has been published [29, 236–238]. To prepare EDLTs, 28-unit-cell-thick films were patterned into 3×3 mm^2 channels between two Pt side-gate electrodes [52, 59]. Ion gels based on the ionic liquids 1-ethyl-3-methylimidazolium bis (trifluoro-methylsulfonyl) imide (EMI:TFSI) or 1-ethyl-3-methylimidazolium dicyanamide (EMI:DCA) in poly(vinylidene fluoride-*co*-hexafluoropropylene) (P(VDF-HFP)) were spin-coated across the channel and gate electrodes to complete devices. EMI:TFSI was chosen for consistency with prior work, whereas EMI:DCA was chosen as it is oxygen-free and thus may avoid contamination of the O K edge. Devices were then wired up and immediately loaded into the beamline vacuum chamber (kept at $< 10^{-8}$ Torr).

6.2.2 Ion-gel Optimization

A pivotal challenge in *operando* soft XAS and XMCD measurements is to optimize the thickness of the ion gel overlying the gated films: while a thin gel is desirable because of the low X-ray penetration depth (~ 1 μm at the Co L edge), the gel must be thick enough to function electrically and achieve uniform gating. The ion-gel optimization was performed by J. Gotchnik and J. Walter in C. Leighton's group at UMN.

Optimization of ion gels for *operando* soft XAS/XMCD was achieved via a series of spin-coating experiments on Si/SiO_x substrates. Solutions with varied polymer : ionic liquid : acetone(solvent) ratio (by mass) were prepared, heated to $\sim 35\,^{\circ}C$, and spun at 1500 rpm for 30 s. Tilt-view (45° with respect to the substrate plane) secondary electron scanning electron microscopy (SEM) images were then collected in a JEOL JSM-6010 PLUS/LA microscope, using 5 kV accelerating voltage. Images collected near an intentional scratch, so that the ion gel thickness (d) could be extracted, are shown in Figure 6.1. Panels (a) - (d) and (e) - (h), for EMI:TFSI and EMI:DCA gels, respectively, show that ion gels become thinner with increasing ratios of ionic liquid and/or solvent. Excessively high ionic liquid/solvent ratios result in an "island and hole" morphology (Figure 6.1d and 6.1h), unsuitable for gating. We thus established the optimized solutions to be about 1:150:50 for EMI:TFSI (Figure 6.1c) and 1:350:50 for EMI:DCA (Figure 6.1g), resulting in $d \approx 1.5 - 2.5$ μm. Upon testing optimized EMI:DCA gels, however (in fact, any EMI:DCA gels), we observed that the LSCoO resistance increased by orders of magnitude in a matter of minutes following spin coating, whereas minimal change (< 0.1 %/min, consistent with prior work [52]) was observed for EMI:TFSI. The rest of the work presented here will thus utilize the 1:150:50 EMI:TFSI gel.

6.2.3 Synchrotron X-ray Measurements

Synchrotron X-ray measurements were performed at beamline 4-ID-C of the Advanced Photon Source. Three different detectors/measurement modes are available: total-electron-yield mode (TEY), total-fluorescence-yield mode (TFY), and reflectivity mode (REF). TEY is dominated by the photoelectric effect, and its probing depth is thus limited to the top unit cells. TFY measures emitted fluorescence photons, and thus has a larger probing depth due to the longer photon mean-free-path. REF deals with the reflection of the X-ray beam by the sample/device at a specific angle, with intensity dependent on the real and imaginary parts of the refractive index. Based on this, bare films were measured in TEY and TFY modes, in grazing-incidence geometry. For *operando* gating, on the other hand, in order to utilize both TFY and REF modes, the films were rotated by 30° facing the X-ray beam, with the fluorescence and reflectivity detectors at 90° and 60°, respectively (Figure 6.2). The TEY mode was not used in gating experiments, as the overlying ion gel inhibits release of photoelectrons. The

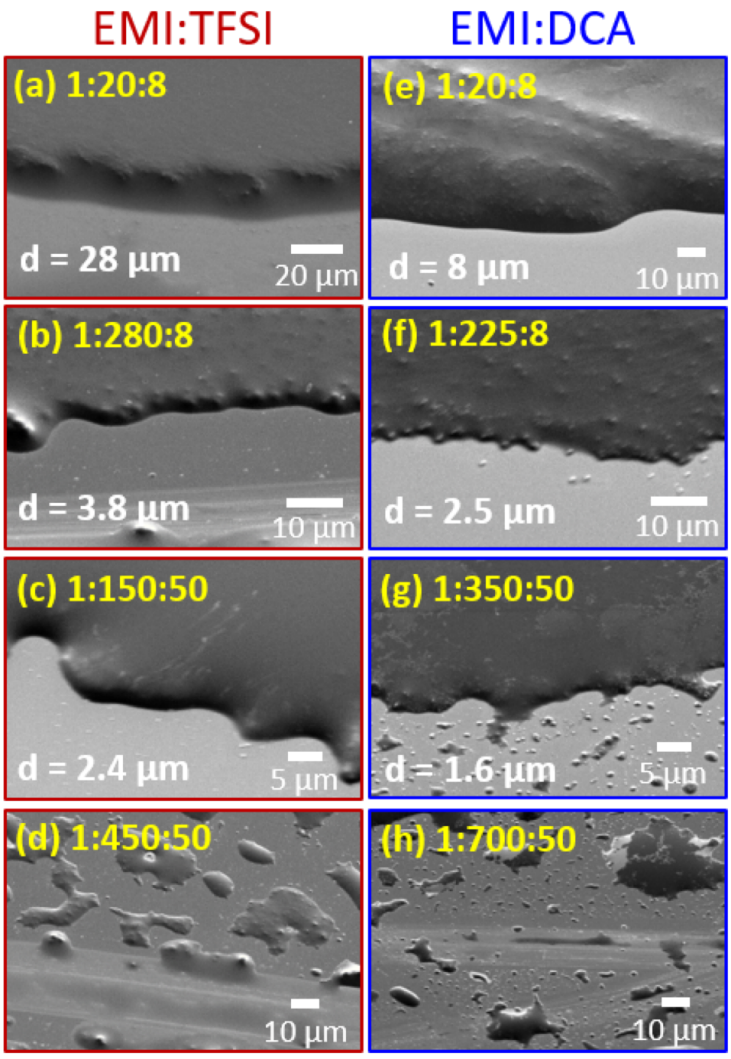

Figure 6.1: Ion-gel optimization. Tilt-view (45°) secondary electron scanning electron microscopy images of ion gels spin-coated on Si/SiO_x substrates at different ratios (by mass) of PVDF-HFP : ionic liquid : acetone, as shown. The ionic liquid was (a-d) EMI:TFSI and (e-h) EMI:DCA. Each coated film was scratched with a blade to enable thickness determination, with the resulting value (d) shown in each panel. The data were taken by J. Gotchnik and J. Walter in C. Leighton's group at UMN.

incident polarization was switched between left-circular and right-circular during the measurements. The sum $(I^+ + I^-)$ of these signals probes the electronic environment of the electrons (XAS), whereas the difference $(I^+ - I^-)$ contains magnetic information (XMCD). The EDLTs were operated at $< 10^{-8}$ Torr, with V_g applied at 310 K for 30 min, with *in-situ* monitoring of electronic transport. *Operando* XAS and XMCD were measured at 75 K (below the Curie temperature, $T_C \approx 220$ K at this thickness), with a magnetic field $H = 4{,}000$ Oe along the X-ray beam; 75 K was chosen so that a large magnetic moment could be reached while keeping the saturation field safely below the maximum available field (4,600 Oe).

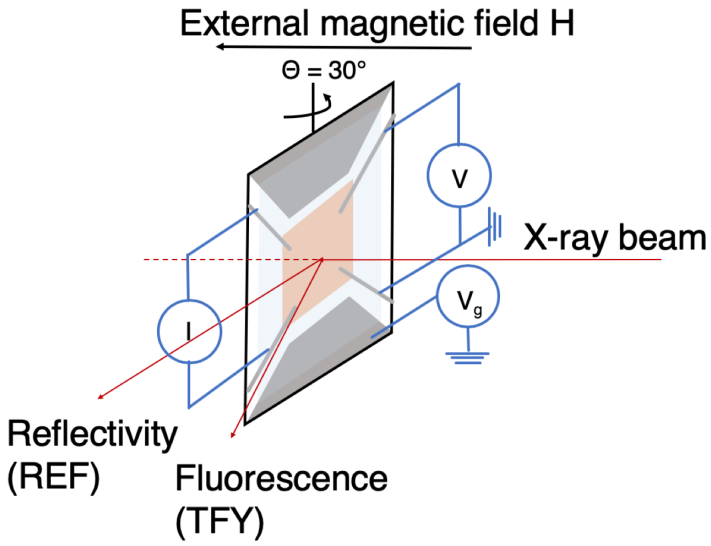

Figure 6.2: Schematic of the device and experimental setup for *operando* XAS/XMCD measurements of ion-gel-gated LSCoO films. The orange area is the LSCoO film (28 unit-cells thick), and the grey pads are Pt electrodes for bias voltage application and *operando* transport measurements. The sample is rotated by $\theta = 30°$ such that both reflectivity and fluorescence channels can be probed. For XMCD (Figure 6.6), a field of $H = 4{,}000$ Oe was applied along the X-ray beam, resulting in a field of about 3,500 Oe in the film plane. The X-ray beam was defocused to cover the entire sample and minimize beam damage.

6.3 Results

6.3.1 Baseline information

We first gathered baseline information for $LaAlO_3(001)$/LSCoO films by probing the evolution of hole doping and magnetism in bare films. Figure 6.3 shows the O K- and Co L-edge XAS and XMCD spectra (TFY) for films of 4, 8, and 25 unit cells (u.c.). The data are normalized to 1 at the main peaks (540 eV for the O K edge, 780 eV for the Co L edge). The O K-edge pre-peak near 527 eV is seen in all films (Figure 6.3a), its intensity noticeably decreasing with decreasing thickness. This pre-peak has been well characterized in bulk LSCoO and linked to the O $2p$ hole density [239]. The clear pre-peak decrease with decreasing thickness thus indicates an obvious decrease in effective hole doping in thinner films. Earlier work tied this to an increase in O deficiency δ near the substrate, leading to a decrease in effective hole doping, i.e., $x_{eff} = x - 2\delta$, in the simplest model [30]. This O deficiency was in turn linked to V_O ordering, which was shown to be the lattice mismatch accommodation mechanism in this system [240]. This effect is also seen in the Co L-edge XAS (Figure 6.3b), from the $\sim$ 0.6 eV shift to lower energy; this is also known to indicate a decrease in Co valence [241]. Consequently, the Co magnetic moment is reduced on going from 25 to 8 u.c. thickness. In particular, as seen from the Co L-edge TFY XMCD in Figure 6.3d, we find no evidence for ferromagnetism in the 4 u.c. film, whereas 8 and 25 u.c. films are clearly ferromagnetic. For bulk LSCoO, it is known that O holes also form magnetic states at the Fermi level, and that the O moment grows with doping [239]. We indeed observe an evolution of magnetism at O hole sites in TEY mode (Figure 6.3c inset), although the low signal-to-noise ratio in TFY mode (Figure 6.3c) results in an inability to resolve this signal. XMCD spectra at the O K edge were not measured further since, as noted, the TEY mode was not possible in gating experiments.

6.3.2 *Operando* XAS Study

With ion gels optimized, we performed *operando* XAS/XMCD measurements of an electrolyte-gated LSCoO film (28 u.c. thickness). Throughout this study, only positive biases were applied, as a model test case. As noted, this V_g polarity causes V_O formation through the entire volume of LSCoO films in this thickness regime, resulting in

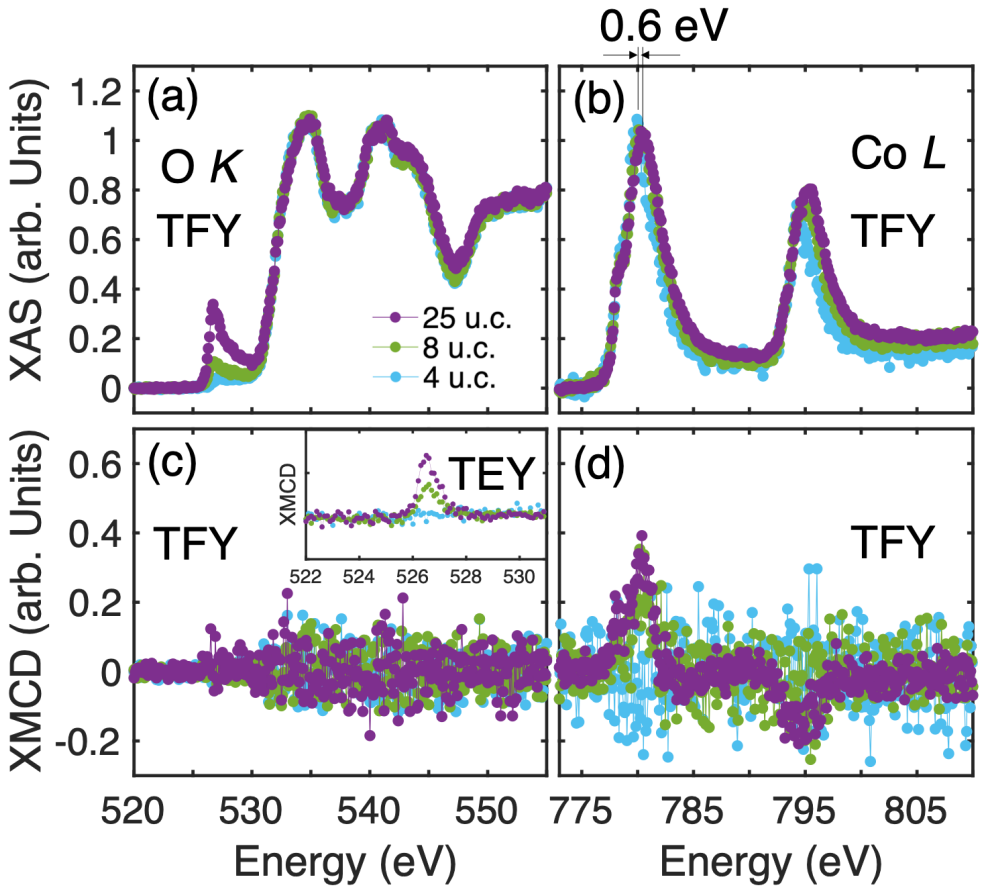

Figure 6.3: Baseline information for bare $LaAlO_3(001)$/LSCoO thin films. (a) O K-edge and (b) Co L-edge XAS spectra of $LaAlO_3(001)/La_{0.5}Sr_{0.5}CoO_{3-\delta}$ films with thickness (t) 4, 8, and 25 unit cells (u.c.). (c) O K-edge and (d) Co L-edge XMCD spectra of the same films. All data taken with grazing incidence X-rays in TFY mode, at temperature $T = 30$ K, with a field $H = 4{,}600$ Oe along the incident beam (i.e., the full field was in the film plane). In (b), a shift from 25 to 8 u.c. is observed (about 0.6 eV at the L_3 edge, as indicated). Inset to (c): TEY XMCD spectra near the pre-peak.

large resistivity [52] and lattice parameter increases [59], and a concomitant decrease in magnetization and Curie temperature. Figure 6.4(a, b) shows the O K-edge electronic structure changes at 75 K, after applying $V_g = +\ 4$ V at 310 K. Most noticeably, the 527 eV O $2p$ pre-peak is seen to be essentially extinguished at $V_g = +\ 4$ V, in both TFY (Figure 6.4a) and REF (Figure 6.4b) modes. This suppression is consistent with formation of a high V_O density at positive biases, decreasing the effective hole concentration ($x_{eff} = x - 2\delta$) by compensation of doped holes. Consistently, the Co L_3-edge XAS peak shifts ~ 1.2 eV to lower energy at $V_g = +\ 4$ V (Figure 6.5), indicating decreasing Co formal valence. The responses of the O K-edge and Co L-edge spectra to *operando* gating are thus qualitatively consistent. We note that, in addition to the LSCoO films, both the $LaAlO_3$ substrate and the ion gel include oxygen. The slight spectral changes at the O K edge above 530 eV might thus involve not only LSCoO, but also the ion gel, e.g., through beam damage.

6.3.3 *Operando* XMCD Study at the Co L_3 Edge

Subsequent gate-induced magnetism changes were probed via Co L_3-edge XMCD. Figure 6.6a and 6.6b show the energy dependence of the TFY and REF XMCD, respectively; these data were obtained at 75 K with an effective magnetic field in the film plane of $\sim$ 3,500 Oe. At $V_g = 0$, a peak occurs around 780.5 eV in TFY mode, whereas two peaks are seen in REF mode due to interference effects, indicative of a substantial Co moment, as expected. Upon application of $V_g = +\ 4$ V these peaks essentially vanish, meaning that the Co moment is strongly suppressed by the hole doping decrease due to V_O formation, as evidenced by XAS. Figure 6.6c shows corresponding hysteresis loops measured at the peak energy ($\sim$ 780.5 eV). The loops show pronounced magnetization and hysteresis (1,740 Oe coercivity) at $V_g = 0$. At $V_g = +\ 4$ V, however, the saturation magnetization decreases substantially (by a factor of ~ 7), in agreement with prior neutron reflectometry measurements [59]. In the latter, a decrease of peak magnetization by a factor of ~ 8 was observed at 30 K for $V_g = +\ 3$ V; our *operando* XMCD results are thus in quantitative agreement with prior neutron reflectometry [59].

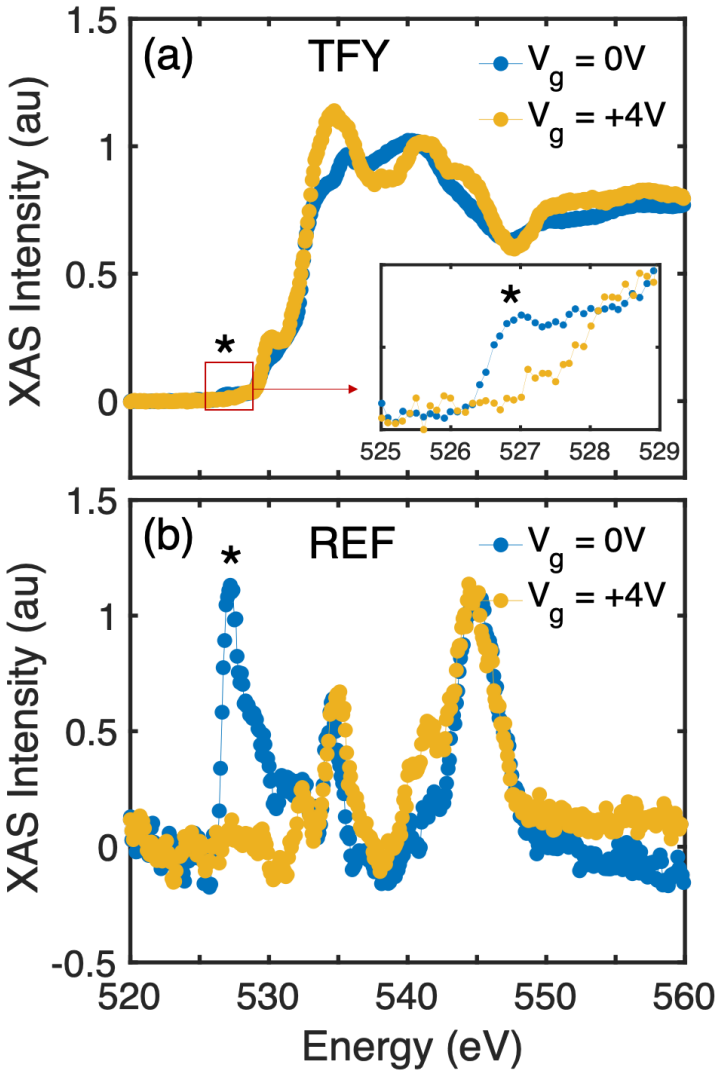

Figure 6.4: Gate-bias (V_g) dependence of O K-edge XAS taken in (a) TFY mode and (b) REF mode. '*' denotes the pre-peak around 527 eV, as highlighted in the inset to (a). All data were taken at $T = 75$ K.

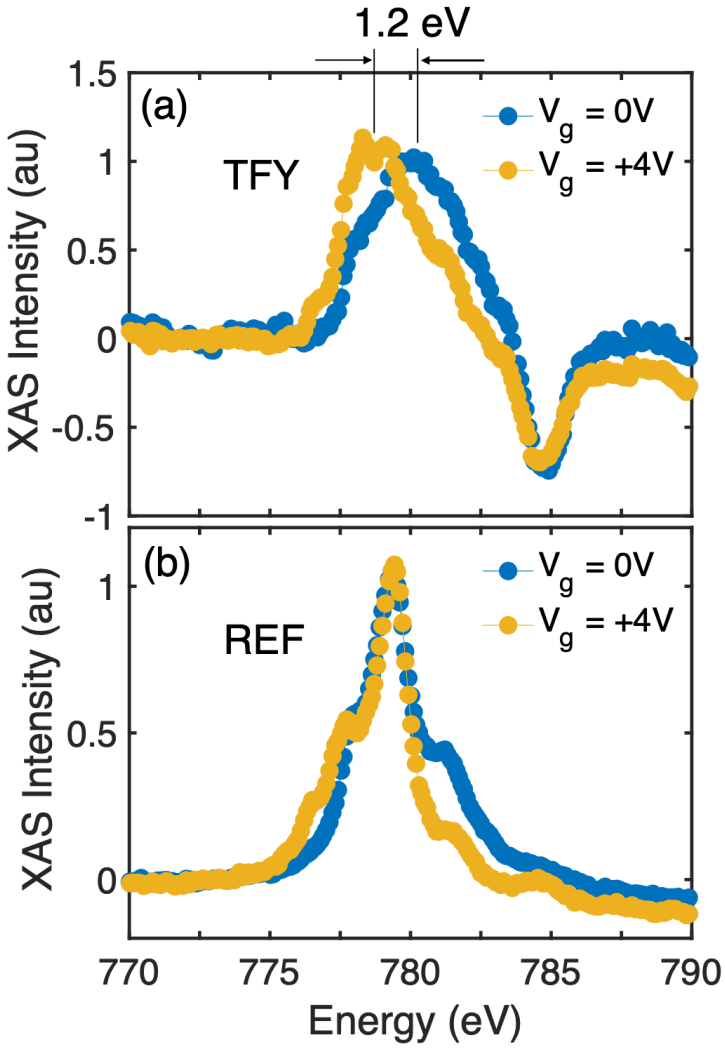

Figure 6.5: Gate-bias (V_g) dependence of Co L_3-edge XAS taken in (a) TFY and (b) REF mode. All data were taken at $T = 75$ K. In (a), the Co L_3 main edge shifts by ~ 1.2 eV at $V_g = +4$ V.

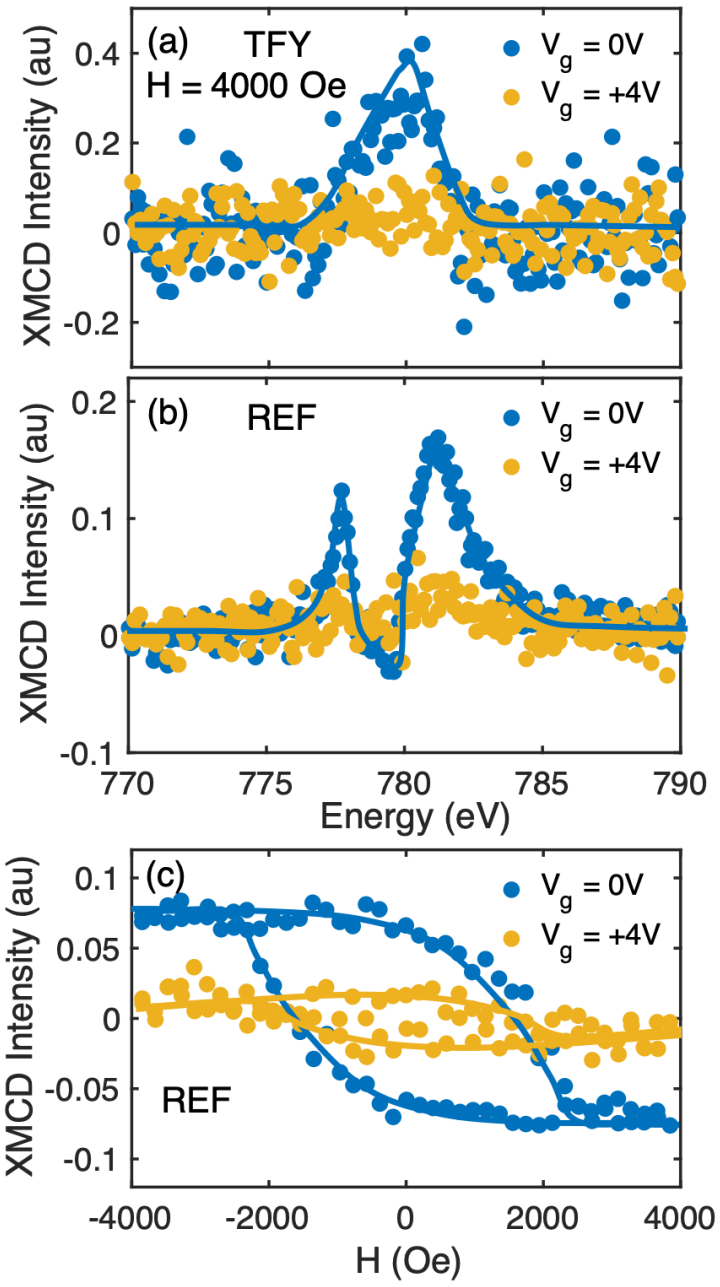

Figure 6.6: Gate-bias (V_g) dependence of magnetic properties probed by XMCD at the Co L_3 edge in (a) TFY and (b) REF mode. Data were taken at T = 75 K with H = 4,000 Oe along the X-ray beam. (c) Change of magnetic hysteresis loop with V_g measured by REF XMCD at 75 K with phonon energy 780.5 eV. Lines are guides to the eye in all cases.

6.4 Challenges

The main limitation in measuring side-gated electrostatically-doped systems is the low penetration depth of soft X-rays. In our earlier tests, we found that the thicker ion gels block X-rays from penetrating the thin film, whereas the thinner ion gels usually result in disconnected islands and holes and cause a non-uniform gating effect. In addition, the ionic liquid (EMI:TFSI) contains a small amount of fluorine, whose K-edge fluorescence tail extends to the Co L edge. Figure 6.7 shows XAS measurements of a sample with a thick ion gel and another identical sample without gel. Although the energy of the F K edge is about ~ 100 eV below the Co L edge, it tails off at much higher energies, with a high intensity that completely covers the thin-film signal at the Co L edge. Our in-house tests of different solutions of ion gels proved to be successful. By optimizing the polymer, ionic-liquid and acetone ratio, we were able to achieve thin and smooth ion-gels. The final thickness of ion-gel is around 1 μm, comparable to the X-ray penetration depth at the Co L edge, therefore enabling the measurements at the Co L edge.

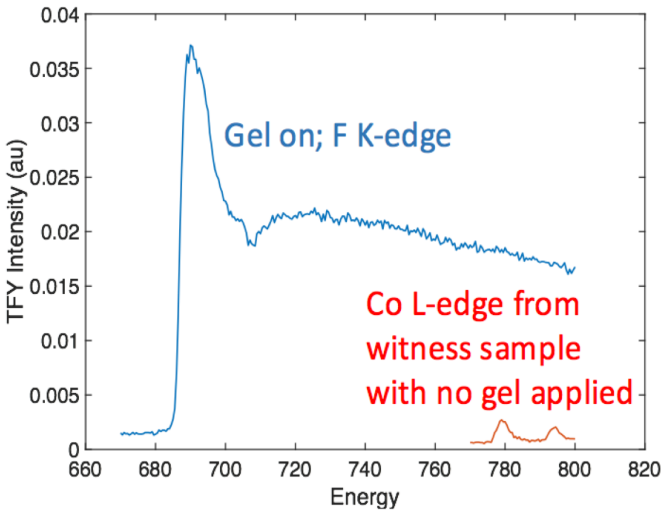

Figure 6.7: F K-edge effect. XAS measurements of a sample with thick ion gel and another identical sample without gel. The thin-film signal at the Co L edge is completely dominated by the long intensity tail from the F K edge.

The other challenge is to minimize beam damage to the ion-gel. During our experiment, we defocused the X-ray beam, and thus worked with a larger beam size to minimize the exposure. However, beam damage still occured, as the spectral shape changed slightly over time (Figure 6.4). We performed a beam-damage test, as shown in Figure 6.8, to ensure that the thin-film properties were unaltered. In this test, the beam flux was intentionally doubled to accelerate the beam damage. The XAS spectra changed slightly due to the beam damage to the gel, but the pre-peak at 527 eV did not change over time, neither in intensity nor in energy.

In summary, we have demonstrated *operando soft* XAS/XMCD measurements on electrolyte-gated oxides, using ion-gel-gated LSCoO films as a test case. Baseline information regarding hole doping and ferromagnetism was first established by measuring O K- and Co L-edge XAS/XMCD on bare $LaAlO_3$/LSCoO films with thickness 4, 8, and 25 u.c. To overcome the penetration depth problem, the ion-gel was optimized with regard to composition and thickness, the latter reaching ~ 1 μm. Data for gated films were then obtained in TFY and REF modes. Application of $V_g = +4$ V resulted in dramatic suppression of the O K-edge XAS pre-peak, indicating a significant decrease in hole doping due to V_O formation at positive V_g. Concomitantly, a significantly reduced Co moment was observed in energy- and field-dependent XMCD spectra. Our investigation of LSCO-based ion-gel EDLTs via *operando soft* XAS/XMCD therefore provides direct evidence for electrochemical changes in hole doping and magnetism. This lays the foundation for *operando soft* XAS/XMCD studies of other electrolyte-gated oxides, also relevant to *operando* studies of battery, ionic conductor, and supercapacitor materials.

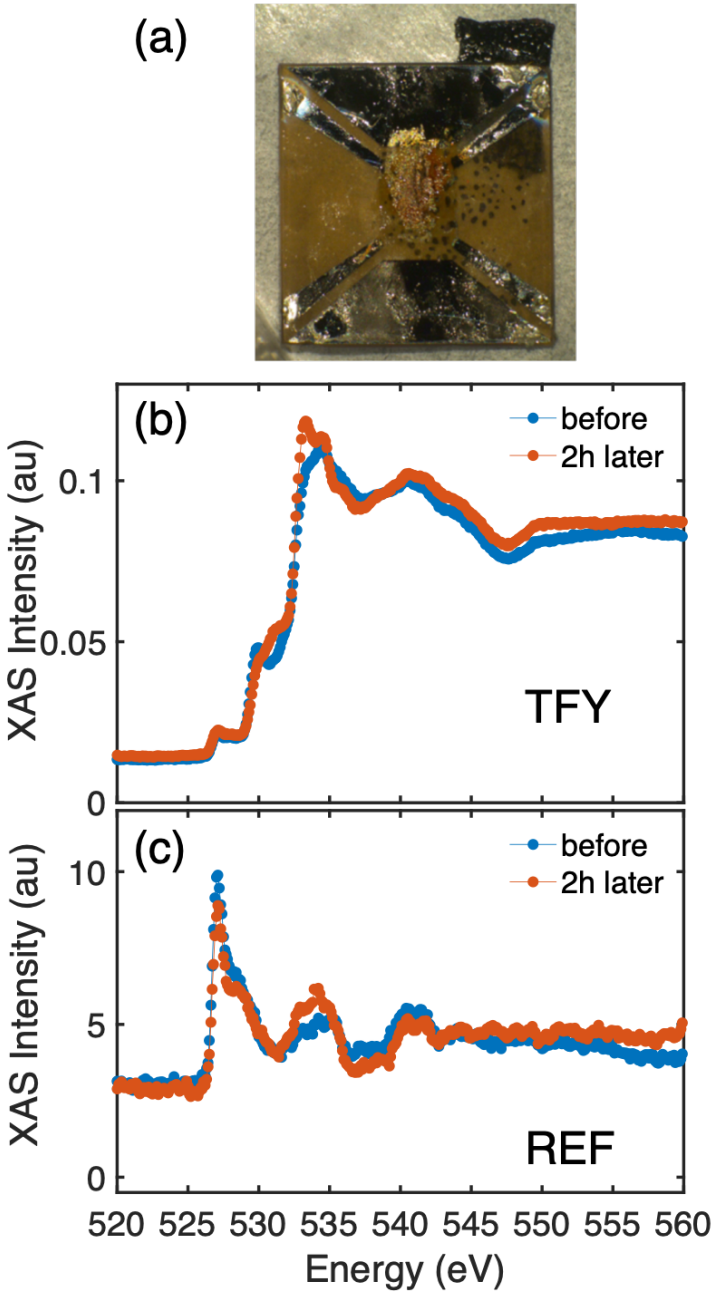

Figure 6.8: Beam damage to the gel. (a) A picture of the gel that is damaged by the beam after 2 days of measurement. XAS at the oxygen K edge before and after 2 hours of X-ray beam exposure, measured in (b) TFY and (c) REF modes. The beam flux was intentionally doubled to accelerate the beam damage. Whereas the XAS spectra changed slightly due to beam damage to the gel, the pre-peak at 527 eV did not change.

References

[1] H. K. Onnes. The resistance of pure mercury at helium temperatures. *Communications from the Laboratory of Physics at the University of Leiden*, 12:120, 1911.

[2] W. Meissner and R. Ochsenfeld. Ein neuer Effekt bei Eintritt der Supraleitfähigkeit. *Naturwissenschaften*, 21(787788):10, 1933.

[3] J. Bardeen, L. N. Cooper, and J. R. Schrieffer. Theory of superconductivity. *Physical Review*, 108(5):1175, 1957.

[4] M. R. Norman and C. Pepin. The electronic nature of high temperature cuprate superconductors. *Reports on Progress in Physics*, 66(10):1547, 2003.

[5] A. P. Drozdov, M. I. Eremets, I. A. Troyan, V. Ksenofontov, and S. I. Shylin. Conventional superconductivity at 203 Kelvin at high pressures in the sulfur hydride system. *Nature*, 525(7567):73, 2015.

[6] J. G. Bednorz and K. A. Müller. Possible high-T_c superconductivity in the Ba-La-Cu-O system. *Zeitschrift für Physik B Condensed Matter*, 64(2):189, 1986.

[7] B. Keimer, S. A. Kivelson, M. R. Norman, S. Uchida, and J. Zaanen. From quantum matter to high-temperature superconductivity in copper oxides. *Nature*, 518(7538):179, 2015.

[8] S. Chakravarty, H.-Y. Kee, and K. Völker. An explanation for a universality of transition temperatures in families of copper oxide superconductors. *Nature*, 428(6978):53, 2004.

[9] N. P. Armitage, P. Fournier, and R. L. Greene. Progress and perspectives on electron-doped cuprates. *Reviews of Modern Physics*, 82:2421, 2010.

[10] G. H. Kwei, S-W. Cheong, Z. Fisk, F. H. Garzon, J. A. Goldstone, and J. D. Thompson. Structure and oxygen stoichiometry for the electron-doped cuprate superconductor $Nd_{1.85}Ce_{0.15}CuO_{4-\delta}$. *Physical Review B*, 40:9370, 1989.

[11] C. Marin, J. Y. Henry, and J. X. Boucherle. Structural neutron diffraction study of a $Nd_2CuO_{4-\delta}$ single crystal. *Solid State Communications*, 86(7):425, 1993.

[12] N. Nücker, P. Adelmann, M. Alexander, H. Romberg, S. Nakai, J. Fink, H. Rietschel, G. Roth, H. Schmidt, and H. Spille. Is $Nd_{2-x}Ce_xCuO_4$ an electron-superconductor? *Zeitschrift für Physik B Condensed Matter*, 75(4):421, 1989.

[13] E. Pellegrin, N. Nücker, J. Fink, S. L. Molodtsov, A. Gutiérrez, E. Navas, O. Strebel, Z. Hu, M. Domke, G. Kaindl, S. Uchida, Y. Nakamura, J. Markl, M. Klauda, G. Saemann-Ischenko, A. Krol, J. L. Peng, Z. Y. Li, and R. L. Greene. Orbital character of states at the Fermi level in $La_{2-x}Sr_xCuO_4$ and $R_{2-x}Ce_xCuO_4$ (R=Nd,Sm). *Physical Review B*, 47:3354, 1993.

[14] D. N. Basov and T. Timusk. Electrodynamics of high-T_c superconductors. *Reviews of Modern Physics*, 77:721, 2005.

[15] E. Dagotto. Correlated electrons in high-temperature superconductors. *Reviews of Modern Physics*, 66:763, 1994.

[16] F. C. Zhang and T. M. Rice. Effective Hamiltonian for the superconducting Cu oxides. *Physical Review B*, 37:3759, 1988.

[17] M. Platé, J. D. F. Mottershead, I. S. Elfimov, D. C. Peets, R. Liang, D. A. Bonn, W. N. Hardy, S. Chiuzbaian, M. Falub, M. Shi, L. Patthey, and A. Damascelli. Fermi surface and quasiparticle excitations of overdoped $Tl_2Ba_2CuO_{6+\delta}$. *Physical Review Letters*, 95:077001, 2005.

[18] B. Vignolle, A. Carrington, R. A. Cooper, M. M. J. French, A. P. Mackenzie, C. Jaudet, D. Vignolles, C. Proust, and N. E. Hussey. Quantum oscillations in an overdoped high-T_c superconductor. *Nature*, 455(7215):952, 2008.

[19] U. Chatterjee, D. Ai, J. Zhao, S. Rosenkranz, A. Kaminski, H. Raffy, Z. Li, K. Kadowaki, M. Randeria, M. R. Norman, and J. C. Campuzano. Electronic phase diagram of high-temperature copper oxide superconductors. *Proceedings of the National Academy of Sciences*, 108(23):9346, 2011.

[20] E. H. da Silva Neto, R. Comin, F. He, R. Sutarto, Y. Jiang, R. L. Greene, G. Sawatzky, and A. Damascelli. Charge ordering in the electron-doped superconductor $Nd_{2-x}Ce_xCuO_4$. *Science*, 347(6219):282, 2015.

[21] E. H. da Silva Neto, B. Yu, M. Minola, R. Sutarto, E. Schierle, F. Boschini, M. Zonno, M. Bluschke, J. Higgins, Y. Li, G. Yu, E. Weschke, F. He, M. Le Tacon, R. L. Greene, M. Greven, G. A. Sawatzky, B. Keimer, and A. Damascelli. Doping-dependent charge order correlations in electron-doped cuprates. *Science Advances*, 2:e1600782, 2016.

[22] M. Itoh, I. Natori, S. Kubota, and K. Motoya. Spin-glass behavior and magnetic phase diagram of $La_{1-x}Sr_xCoO_3$ ($0 \leqslant x \leqslant 0.5$) studied by magnetization measurements. *Journal of the Physical Society of Japan*, 63(4):1486, 1994.

[23] P. S. A. Kumar, P. A. Joy, and S. K. Date. Origin of the cluster-glass-like magnetic properties of the ferromagnetic system. *Journal of Physics: Condensed Matter*, 10(29):L487, 1998.

[24] V. V. Sikolenko, A. P. Sazonov, I. O. Troyanchuk, D. Többens, U. Zimmermann, E. V. Pomjakushina, and H. Szymczak. Magnetic properties of $La_{1-x}Sr_xCoO_3$ ($x = 0.15$ and 0.3). *Journal of Physics: Condensed Matter*, 16(41):7313, 2004.

[25] H. M. Aarbogh, J. Wu, L. Wang, H. Zheng, J. F. Mitchell, and C. Leighton. Magnetic and electronic properties of $La_{1-x}Sr_xCoO_3$ single crystals across the percolation metal-insulator transition. *Physical Review B*, 74:134408, 2006.

[26] C. He, M. A. Torija, J. Wu, J. W. Lynn, H. Zheng, J. F. Mitchell, and C. Leighton. Non-Griffiths-like clustered phase above the Curie temperature of the doped perovskite cobaltite $La_{1-x}Sr_xCoO_3$. *Physical Review B*, 76:014401, 2007.

[27] A. Mineshige, M. Inaba, T. Yao, O. Zempachi, K. Kikuchi, and M. Kawase. Crystal structure and metal-insulator transition of $La_{1-x}Sr_xCoO_3$. *Journal of Solid State Chemistry*, 121(2):423, 1996.

[28] G. H. Jonker and J. H. Van Santen. Magnetic compounds with perovskite structure III. ferromagnetic compounds of cobalt. *Physica*, 19(1-12):120, 1953.

[29] J. Gazquez, S. Bose, M. Sharma, M. A. Torija, S. J. Pennycook, C. Leighton, and M. Varela. Lattice mismatch accommodation via oxygen vacancy ordering in epitaxial $La_{0.5}Sr_{0.5}CoO_{3-\delta}$ thin films. *APL Materials*, 1(1):012105, 2013.

[30] M. A. Torija, M. Sharma, J. Gazquez, M. Varela, C. He, J. Schmitt, J. A. Borchers, M. Laver, S. El-Khatib, and C. Leighton. Chemically driven nanoscopic magnetic phase separation at the $SrTiO_3(001)/La_{1-x}Sr_xCoO_3$ interface. *Advanced Materials*, 23(24):2711, 2011.

[31] J. Walter, S. Bose, M. Cabero, G. Yu, M. Greven, M. Varela, and C. Leighton. Perpendicular magnetic anisotropy via strain-engineered oxygen vacancy ordering in epitaxial $La_{1-x}Sr_xCoO_{3-\delta}$. *Physical Review Materials*, 2:111404, 2018.

[32] C. H. Ahn, A. Bhattacharya, M. Di Ventra, J. N. Eckstein, C. D. Frisbie, M. E. Gershenson, A. M. Goldman, I. H. Inoue, J. Mannhart, A. J. Millis, A. F. Morpurgo, D. Natelson, and J.-M. Triscone. Electrostatic modification of novel materials. *Reviews of Modern Physics*, 78:1185, 2006.

[33] A.M. Goldman. Electrostatic gating of ultrathin films. *Annual Review of Materials Research*, 44(1):45, 2014.

[34] C. Leighton. Electrolyte-based ionic control of functional oxides. *Nature Materials*, 18(1):13, 2019.

[35] S. Z. Bisri, S. Shimizu, M. Nakano, and Y. Iwasa. Endeavor of iontronics: from fundamentals to applications of ion-controlled electronics. *Advanced Materials*, 29(25):1607054, 2017.

[36] A. T. Bollinger, G. Dubuis, J. Misewich, A. T. Bollinger, I. Božović, D. Pavuna, and J. Yoon. Superconductor-insulator transition in $La_{2-x}Sr_xCuO_4$ at the pair quantum resistance. *Nature*, 472(7344):458, 2011.

[37] X. Leng, J. Pereiro, J. Strle, G. Dubuis, A. T. Bollinger, A. Gozar, J. Wu, N. Litombe, C. Panagopoulos, D. Pavuna, and I. Božović. Electrostatic control of the evolution from a superconducting phase to an insulating phase in ultrathin $YBa_2Cu_3O_{7-x}$ films. *Physical Review Letters*, 107(2):027001, 2011.

[38] H. Sato, K. Hanzawa, H. Hiramatsu, H. Hosono, and T. Kamiya. Electric field-induced superconducting transition of insulating FeSe thin film at 35 K. *Proceedings of the National Academy of Sciences*, 113(15):3986, 2016.

[39] T. Miyakawa, J. Shiogai, S. Shimizu, M. Matsumoto, Y. Ito, T. Harada, K. Fujiwara, T. Nojima, Y. Itoh, T. Aida, Y. Iwasa, and A. Tsukazaki. Enhancement of superconducting transition temperature in FeSe electric-double-layer transistor with multivalent ionic liquids. *Physical Review Materials*, 2(3):031801, 2018.

[40] H. Tanaka, J. Zhang, and T. Kawai. Giant electric field modulation of double exchange ferromagnetism at room temperature in the perovskite manganite/titanate $p-n$ junction. *Physical Review Letters*, 88:027204, 2001.

[41] A. S. Dhoot, C. Israel, X. Moya, N. D. Mathur, and R. H. Friend. Large electric field effect in electrolyte-gated manganites. *Physical Review Letters*, 102(13):136402, 2009.

[42] M. J. Panzer and C. D. Frisbie. Exploiting ionic coupling in electronic devices: electrolyte-gated organic field-effect transistors. *Advanced Materials*, 20(16):3177, 2008.

[43] K. Ueno, S. Nakamura, H. Shimotani, H. T. Yuan, N. Kimura, T. Nojima, H. Aoki, Y. Iwasa, and M. Kawasaki. Discovery of superconductivity in $KTaO_3$ by electrostatic carrier doping. *Nature Nanotechnology*, 6(7):408, 2011.

[44] K. Ueno, S. Nakamura, N. Kimura, A. Ohtomo, M. Kawasaki, H. Shimotani, Y. Iwasa, H. Aoki, T. Nojima, and K. Ueno. Electric-field-induced superconductivity in an insulator. *Nature Materials*, 7(11):855, 2008.

[45] W. Xie, X. Zhang, C. Leighton, and C. D. Frisbie. 2D insulator-metal transition in aerosol-jet-printed electrolyte-gated indium oxide thin film transistors. *Advanced Electronic Materials*, 3(3):1600369, 2017.

[46] H. Yuan, H. Shimotani, A. Tsukazaki, A. Ohtomo, M. Kawasaki, and Y. Iwasa. High-density carrier accumulation in ZnO field-effect transistors gated by electric double layers of ionic liquids. *Advanced Functional Materials*, 19(7):1046, 2009.

[47] R. Scherwitzl, P. Zubko, I. G. Lezama, S. Ono, A. F. Morpurgo, G. Catalan, and J. M. Triscone. Electric-field control of the metal-insulator transition in ultrathin $NdNiO_3$ films. *Advanced Materials*, 22(48):5517, 2010.

[48] Y. Yamada, K. Ueno, T. Fukumura, H. T. Yuan, H. Shimotani, Y. Iwasa, L. Gu, S. Tsukimoto, Y. Ikuhara, and M. Kawasaki. Electrically induced ferromagnetism at room temperature in cobalt-doped titanium dioxide. *Science*, 332(6033):1065, 2011.

[49] S. H. Kim, K. Hong, W. Xie, K. H. Lee, S. Zhang, T. P. Lodge, and C. D. Frisbie. Electrolyte-gated transistors for organic and printed electronics. *Advanced Materials*, 25(13):1822, 2013.

[50] T. Fujimoto and K. Awaga. Electric-double-layer field-effect transistors with ionic liquids. *Physical Chemistry Chemical Physics*, 15(23):8983, 2013.

[51] H. Du, X. Lin, Z. Xu, and D. Chu. Electric double-layer transistors: a review of recent progress. *Journal of Materials Science*, 50(17):5641, 2015.

[52] J. Walter, H. Wang, B. Luo, C. D. Frisbie, and C. Leighton. Electrostatic versus electrochemical doping and control of ferromagnetism in ion-gel-gated ultrathin $La_{0.5}Sr_{0.5}CoO_{3-\delta}$. *ACS Nano*, 10(8):7799, 2016.

[53] H. Yuan, H. Shimotani, J. Ye, S. Yoon, H. Aliah, A. Tsukazaki, M. Kawasaki, and Y. Iwasa. Electrostatic and electrochemical nature of liquid-gated electric-double-layer transistors based on oxide semiconductors. *Journal of the American Chemical Society*, 132(51):18402, 2010.

[54] J. Jeong, N. Aetukuri, T. Graf, T. D. Schladt, M. G. Samant, and S. S. P. Parkin. Suppression of metal-insulator transition in VO_2 by electric field-induced oxygen vacancy formation. *Science*, 339(6126):1402, 2013.

[55] M. Li, W. Han, J. Jeong, M. G. Samant, and S. S. P. Parkin. Suppression of ionic liquid gate-induced metallization of $SrTiO_3$ (001) by oxygen. *Nano Letters*, 13(10):4675, 2013.

[56] H. T. Yi, B. Gao, W. Xie, S. W. Cheong, and V. Podzorov. Tuning the metal-insulator crossover and magnetism in $SrRuO_3$ by ionic gating. *Scientific Reports*, 4(1):6604, 2014.

[57] S. Bubel, A. J. Hauser, A. M. Glaudell, T. E. Mates, S. Stemmer, and M. L. Chabinyc. The electrochemical impact on electrostatic modulation of the metal-insulator transition in nickelates. *Applied Physics Letters*, 106(12):122102, 2015.

[58] T. D. Schladt, T. Graf, N. B. Aetukuri, M. Li, A. Fantini, X. Jiang, M. G. Samant, and S. S. P. Parkin. Crystal-facet-dependent metallization in electrolyte-gated rutile TiO_2 single crystals. *ACS Nano*, 7(9):8074, 2013.

[59] J. Walter, G. Yu, B. Yu, A. Grutter, B. Kirby, J. Borchers, Z. Zhang, H. Zhou, T. Birol, M. Greven, and C. Leighton. Ion-gel-gating-induced oxygen vacancy formation in epitaxial $La_{0.5}Sr_{0.5}CoO_{3-\delta}$ films from in operando X-ray and neutron scattering. *Physical Review Materials*, 1(7):071403(R), 2017.

[60] Y. Dong, H. Zhou, D. D. Fong, W. Wu, Z. Luo, C. Gao, and H. Xu. Effect of gate voltage polarity on the ionic liquid gating behavior of $NdNiO_3/NdGaO_3$ heterostructures. *APL Materials*, 5(5):051101, 2017.

[61] X. Leng, J. Pereiro, J. Strle, G. Dubuis, A. T. Bollinger, A. Gozar, J. Wu, N. Litombe, C. Panagopoulos, D. Pavuna, and I. Božović. Insulator to metal transition in WO_3 induced by electrolyte gating. *npj Quantum Materials*, 2(1):35, 2017.

[62] N. Lu, P. Zhang, Q. Zhang, R. Qiao, Q. He, H. B. Li, Y. Wang, J. Guo, D. Zhang, Z. Duan, Z. Li, M. Wang, S. Yang, M. Yan, E. Arenholz, S. Zhou, W. Yang, L. Gu, C. W. Nan, J. Wu, Y. Tokura, and P. Yu. Electric-field control of tri-state phase transformation with a selective dual-ion switch. *Nature*, 546(7656):124, 2017.

[63] A. M. Perez-Muñoza, P. Schioa, R. Polonid, A. Fernandez-Martineze, A. Rivera-Calzadaa, J. C. Cezarc, E. Salas-Coleraf, G. R. Castrof, J. Kinneyh, C. Leona, J. Santamariaa, J. Garcia, and A. M. Goldman. In operando evidence of deoxygenation in ionic liquid gating of $YBa_2Cu_3O_{7-\delta}$. *Proceedings of the National Academy of Sciences*, 114(2):215, 2016.

[64] J. Walter, T. Charlton, H. Ambaye, M. R. Fitzsimmons, P. P. Orth, R. M. Fernandes, and C. Leighton. Giant electrostatic modification of magnetism via electrolyte-gate-induced cluster percolation in $La_{1-x}Sr_xCoO_{3-\delta}$. *Physical Review Materials*, 2:111406(R), 2018.

[65] J. Walter. *Ion gel gating of perovskite cobaltite thin films: Understanding mechanisms and control of magnetism.* PhD thesis, University of Minnesota, 2018.

[66] K. H. Lee, M. S. Kang, S. Zhang, Y. Gu, T. P. Lodge, and C. D. Frisbie. "cut and stick" rubbery ion gels as high capacitance gate dielectrics. *Advanced Materials*, 24(32):4457, 2012.

[67] B. Yu, W. Tabis, I. Bialo, F. Yakhou, N. Brookes, Z. Anderson, Y. Tang, G. Yu, and M. Greven. Unusual dynamic charge-density-wave correlations in $HgBa_2CuO_{4+\delta}$. *arXiv:1907.10047.*

[68] B. Yu, G. Yu, J. Walter, V. Chaturvedi, J. Gotchnik, J. W. Freeland, C. Leighton, and M. Greven. Soft X-ray absorption spectroscopy and magnetic circular dichroism as operando probes of complex oxide electrolyte gate transistors. *arXiv:1911.07139.*

[69] W. Tabis, B. Yu, I. Bialo, M. Bluschke, T. Kolodziej, A. Kozlowski, E. Blackburn, K. Sen, E. M. Forgan, M. v. Zimmermann, Y. Tang, E. Weschke, B. Vignolle, M. Hepting, H. Gretarsson, R. Sutarto, F. He, M. Le Tacon, N. Barišić, G. Yu, and M. Greven. Synchrotron X-ray scattering study of charge-density-wave order in $HgBa_2CuO_{4+\delta}$. *Physical Review B*, 96:134510, 2017.

[70] E. H. da Silva Neto, M. Minola, B. Yu, W. Tabis, M. Bluschke, D. Unruh, H. Suzuki, Y. Li, G. Yu, D. Betto, K. Kummer, F. Yakhou, N. B. Brookes, M. Le Tacon, M. Greven, B. Keimer, and A. Damascelli. Coupling between

dynamic magnetic and charge-order correlations in the cuprate superconductor $Nd_{2-x}Ce_xCuO_4$. *Physical Review B*, 98:161114(R), 2018.

[71] L. Wang, B. Yu, R. Jing, X. Luo, J. Zeng, J. Li, I. Bialo, M. Bluschke, Y. Tang, J. Freyermuth, G. Yu, R. Sutarto, F. He, E. Weschke, W. Tabis, M. Greven, and Y. Li. Doping-dependent phonon anomaly and charge-order phenomena in the $HgBa_2CuO_{4+\delta}$ and $HgBa_2CaCu_2O_{6+\delta}$. *arXiv:1910.08254*.

[72] L. Wang, X. Luo, J. Li, J. Zeng, M. Cheng, J. Freyermuth, Y. Tang, B. Yu, G. Yu, M. Greven, and Y. Li. Growth and characterization of $HgBa_2CaCu_2O_{6+\delta}$ and $HgBa_2Ca_2Cu_3O_{8+\delta}$ crystals. *Physical Review Materials*, 2(12):123401, 2018.

[73] H. Wang, J. Walter, K. Ganguly, B. Yu, G. Yu, Z. Zhang, H. Zhou, H. Fu, M. Greven, and C. Leighton. Wide-voltage-window reversible control of electronic transport in electrolyte-gated epitaxial $BaSnO_3$. *Physical Review Materials*, 3:075001, 2019.

[74] D. Pelc, Z. Anderson, B. Yu, C. Leighton, and M. Greven. Universal superconducting precursor in three classes of unconventional superconductors. *Nature Communications*, 10:2729, 2019.

[75] H. J. Scheel. Crystal growth problems of $YBa_2Cu_3O_{7-x}$. *Physica C: Superconductivity*, 153-155:44, 1988.

[76] K. Oka and H. Unoki. Phase diagram of the La_2O_3-CuO system and crystal growth of $(LaBa)_2CuO_4$. *Japanese Journal of Applied Physics*, 26(10A):L1590, 1987.

[77] J. M. S Skakle and A. R. West. Subsolidus relations in the La_2O_3-CuO-CaO phase diagram and the La_2O_3-CuO binary join. *Journal of the American Ceramic Society*, 77(8):2199, 1994.

[78] O. P. Vajk. *Quantum impurities in a two-dimensional Heisenberg antiferromagnet*. PhD thesis, Stanford University, 2003.

[79] A. Schilling, M. Cantoni, J. D. Guo, and H. R. Ott. Superconductivity above 130 K in the Hg–Ba–Ca–Cu–O system. *Nature*, 363(6424):56, 1993.

[80] E. V. Antipov, A. M. Abakumov, and S. N. Putilin. Chemistry and structure of Hg-based superconducting Cu mixed oxides. *Superconductor Science and Technology*, 15(7):R31, 2002.

[81] X. Zhao, G. Yu, Y. Cho, G. Chabot-Couture, N. Barišić, P. Bourges, N. Kaneko, Y. Li, L. Lu, E. M. Motoyama, O. P. Vajk, and M. Greven. Crystal growth and characterization of the model high-temperature superconductor $HgBa_2CuO_{4+\delta}$. *Advanced Materials*, 18(24):3243, 2006.

[82] Y. Tang. *Neutron Scattering Study of the Cuprate Superconductor $HgBa_2CuO_{4+\delta}$*. PhD thesis, University of Minnesota, 2018.

[83] W. Friedrich, P. Knipping, and M. Laue. Interferenzerscheinungen bei Röntgenstrahlen. *Annalen der Physik*, 346(10):971, 1913.

[84] K. Uchinokura, T. Ino, I. Terasaki, and I. Tsukada. Effect of substitution of Zn^{2+} for Cu^{2+} on the magnetic properties of $La_2Cu_{1-x}Zn_xO_4$ single crystals. *Physica B: Condensed Matter*, 205(2):234, 1995.

[85] N. Barišić, Y. Li, X. Zhao, Y.-C. Cho, G. Chabot-Couture, G. Yu, and M. Greven. Demonstrating the model nature of the high-temperature superconductor $HgBa_2CuO_{4+\delta}$. *Physical Review B*, 78:054518, 2008.

[86] B. Keimer, A. Aharony, A. Auerbach, R. J. Birgeneau, A. Cassanho, Y. Endoh, R. W. Erwin, M. A. Kastner, and G. Shirane. Néel transition and sublattice magnetization of pure and doped La_2CuO_4. *Physical Review B*, 45(13):7430, 1992.

[87] R. J. Birgeneau, A. Aharony, N. R. Belk, F. C. Chou, Y. Endoh, M. Greven, S. Hosoya, M. A. Kastner, C. H. Lee, Y. S. Lee, G. Shirane, S. Wakimoto, B. O. Wells, and K. Yamada. Magnetism and magnetic fluctuations in $La_{1-x}Sr_xCuO_4$ for $x = 0$ (2d antiferromagnet), 0.04 (3d spin glass) and $x = 0.15$ (superconductor). *Journal of Physics and Chemistry of Solids*, 56(12):1913, 1995. Proceedings of the Conference on Spectroscopies in Novel Superconductors.

[88] L. J. P. Ament, M. Van Veenendaal, T. P. Devereaux, J. P. Hill, and J. Van Den Brink. Resonant inelastic X-ray scattering studies of elementary excitations. *Reviews of Modern Physics*, 83(2):705, 2011.

[89] G. L. Squires. *Introduction to the theory of thermal neutron scattering*. Courier Corporation, 1996.

[90] H. A. Kramers and W. Heisenberg. Über die streuung von strahlung durch atome. *Zeitschrift für Physik*, 31(1):681, 1925.

[91] F. Sette and M. Krisch. Inelastic X-ray scattering from collective atom dynamics. In *Neutron and X-ray Spectroscopy*, page 169. Springer, 2006.

[92] L. Van Hove. Correlations in space and time and born approximation scattering in systems of interacting particles. *Physical Review*, 95(1):249, 1954.

[93] R. F. Egerton. *Electron energy-loss spectroscopy in the electron microscope*. Springer Science & Business Media, 2011.

[94] K. Ishii, T. Tohyama, and J. Mizuki. Inelastic X-ray scattering studies of electronic excitations. *Journal of the Physical Society of Japan*, 82(2):021015, 2013.

[95] J. L. Tallon, C. Bernhard, H. Shaked, R. L. Hitterman, and J. D. Jorgensen. Generic superconducting phase behavior in high-T_c cuprates: T_c variation with hole concentration in $YBa_2Cu_3O_{7-\delta}$. *Physical Review B*, 51:12911, 1995.

[96] M. Vojta and S. Sachdev. Charge order, superconductivity, and a global phase diagram of doped antiferromagnets. *Physical Review Letters*, 83(19):3916, 1999.

[97] J. M. Tranquada, B. J. Sternlieb, J. D. Axe, Y. Nakamura, and S. Uchida. Evidence for stripe correlations of spins and holes in copper oxide superconductors. *Nature*, 375(6532):561, 1995.

[98] N. Doiron-Leyraud, C. Proust, D. LeBoeuf, J. Levallois, J. Bonnemaison, R. Liang, D. A. Bonn, W. N. Hardy, and L. Taillefer. Quantum oscillations and the Fermi surface in an underdoped high-T_c superconductor. *Nature*, 447(7144):565, 2007.

[99] D. LeBoeuf, N. Doiron-Leyraud, J. Levallois, R. Daou, J.-B. Bonnemaison, N. E. Hussey, L. Balicas, B. J. Ramshaw, R. Liang, D. A. Bonn, W. N. Hardy, S. Adachi, C. Proust, and L. Taillefer. Electron pockets in the Fermi surface of hole-doped high-T_c superconductors. *Nature*, 450(7169):533, 2007.

[100] W. D. Wise, M. C. Boyer, K. Chatterjee, T. Kondo, T. Takeuchi, H. Ikuta, Y. Wang, and E. W. Hudson. Charge-density-wave origin of cuprate checkerboard visualized by scanning tunnelling microscopy. *Nature Physics*, 4(9):696, 2008.

[101] T. Wu, H. Mayaffre, S. Krämer, M. Horvatić, C. Berthier, W. N. Hardy, R. Liang, D. A. Bonn, and M.-H. Julien. Magnetic-field-induced charge-stripe order in the high-temperature superconductor $YBa_2Cu_3O_y$. *Nature*, 477:191, 2011.

[102] G. Ghiringhelli, M. Le Tacon, M. Minola, C. Mazzoli, N. B. Brookes, G. M. De Luca, A. Frano, D. G. Hawthorn, F. He, T. Loew, M. Moretti Sala, D. C. Peets, M. Salluzzo, E. Schierle, R. Sutarto, G. A. Sawatzky, E. Weschke, B. Keimer, and L. Braicovich. Long-range incommensurate charge fluctuations in (Y,Nd)$Ba_2Cu_3O_{6+\delta}$. *Science*, 337:821, 2012.

[103] J. Chang, E. Blackburn, A. T. Holmes, N. B. Christensen, J. Larsen, J. Mesot, R. Liang, D. A. Bonn, W. N. Hardy, A. Watenphul, M. V. Zimmermann, E. M. Forgan, and S. M. Hayden. Direct observation of competition between superconductivity and charge density wave order in $YBa_2Cu_3O_{6.67}$. *Nature Physics*, 8(12):871, 2012.

[104] J. Chang, E. Blackburn, O. Ivashko, A. T. Holmes, N. B. Christensen, M. Hücker, R. Liang, D. A. Bonn, W. N. Hardy, U. Rütt, M. V. Zimmermann, E. M. Forgan, and S. M. Hayden. Magnetic field controlled charge density wave coupling in underdoped $YBa_2Cu_3O_{6+x}$. *Nature Communications*, 7:11494, 2016.

[105] R. Comin, A. Frano, M. M. Yee, Y. Yoshida, H. Eisaki, E. Schierle, E. Weschke, R. Sutarto, F. He, A. Soumyanarayanan, Y. He, M. Le Tacon, I. S. Elfimov, J. E. Hoffman, G. A. Sawatzky, B. Keimer, and A. Damascelli. Charge order driven by Fermi-arc instability in $Bi_2Sr_{2-x}La_xCuO_{6+\delta}$. *Science*, 343(6169):390, 2014.

[106] W. Tabis, Y. Li, M. Le Tacon, L. Braicovich, A. Kreyssig, M. Minola, G. Dellea, E. Weschke, M. J. Veit, M. Ramazanoglu, A. I. Goldman, T. Schmitt, G. Ghiringhelli, N. Barišić, M. K. Chan, C. J. Dorow, G. Yu, X. Zhao, B. Keimer, and M. Greven. Charge order and its connection with Fermi-liquid charge transport in a pristine high-T_c cuprate. *Nature Communications*, 5:5875, 2014.

[107] T. P. Croft, C. Lester, M. S. Senn, A. Bombardi, and S. M. Hayden. Charge density wave fluctuations in $La_{2-x}Sr_xCuO_4$ and their competition with superconductivity. *Physical Review B*, 89:224513, 2014.

[108] S. Blanco-Canosa, A. Frano, E. Schierle, J. Porras, T. Loew, M. Minola, M. Bluschke, E. Weschke, B. Keimer, and M. Le Tacon. Resonant X-ray scattering study of charge density wave correlations in $YBa_2Cu_3O_{6+x}$. *Physical Review B*, 90:054513, 2014.

[109] M. Hashimoto, G. Ghiringhelli, W. S. Lee, G. Dellea, A. Amorese, C. Mazzoli, K. Kummer, N. B. Brookes, B. Moritz, Y. Yoshida, H. Eisaki, Z. Hussain, T. P. Devereaux, Z. X. Shen, and L. Braicovich. Direct observation of bulk charge modulations in optimally doped $Bi_{1.5}Pb_{0.6}Sr_{1.54}CaCu_2O_{8+\delta}$. *Physical Review B*, 89(22):220511, 2014.

[110] E. H. da Silva Neto, P. Aynajian, A. Frano, R. Comin, E. Schierle, E. Weschke, A. Gyenis, J. Wen, J. Schneeloch, Z. Xu, S. Ono, G. Gu, M. Le Tacon, and A. Yazdani. Ubiquitous interplay between charge ordering and high-temperature superconductivity in cuprates. *Science*, 343(6169):393, 2014.

[111] S. Gerber, H. Jang, H. Nojiri, S. Matsuzawa, H. Yasumura, D. A. Bonn, R. Liang, W. N. Hardy, Z. Islam, A. Mehta, S. Song, M. Sikorski, D. Stefanescu, Y. Feng, S. A. Kivelson, and T. P. Devereaux. Three-dimensional charge density wave order in $YBa_2Cu_3O_{6.67}$ at high magnetic fields. *Science*, 350(6263):949, 2015.

[112] Y. Y. Peng, M. Salluzzo, X. Sun, A. Ponti, D. Betto, A. M. Ferretti, F. Fumagalli, K. Kummer, M. Le Tacon, X. J. Zhou, N. B. Brookes, L. Braicovich, and G. Ghiringhelli. Direct observation of charge order in underdoped and optimally doped $Bi_2(Sr,La)_2CuO_{6+\delta}$ by resonant inelastic X-ray scattering. *Physical Review B*, 94(18):184511, 2016.

[113] R. Arpaia, S. Caprara, R. Fumagalli, G. De Vecchi, Y. Y. Peng, E. Andersson, D. Betto, G. M. De Luca, N. B. Brookes, F. Lombardi, M. Salluzzo, L. Braicovich, C. D. Castro, M. Grilli, and G. Ghiringhelli. Dynamical charge density fluctuations pervading the phase diagram of a Cu-based high-T_c superconductor. *Science*, 365(6456):906, 2019.

[114] Y. Y. Peng, R. Fumagalli, Y. Ding, M. Minola, S. Caprara, D. Betto, M. Bluschke, G. M. Luca, K. Kummer, E. Lefranamp, M. Salluzzo, H. Suzuki, M. Tacon, X. J. Zhou, N. B. Brookes, B. Keimer, L. Braicovich, M. Grilli, and G. Ghiringhelli. Re-entrant charge order in overdoped $(Bi,Pb)_{2.12}Sr_{1.88}CuO_{6+\delta}$ outside the pseudogap regime. *Nature Materials*, 17(8):697, 2018.

[115] S. E. Sebastian, N. Harrison, and G. G. Lonzarich. Towards resolution of the Fermi surface in underdoped high-T_c superconductors. *Reports on Progress in Physics*, 75:102501, 2012.

[116] H. Miao, J. Lorenzana, G. Seibold, Y. Y. Peng, A. Amorese, F. Yakhou-Harris, K. Kummer, N. B. Brookes, R. M. Konik, V. Thampy, G. D. Gu, G. Ghiringhelli, L. Braicovich, and M. P. M. Dean. High-temperature charge density wave correlations in $La_{1.875}Ba_{0.125}CuO_4$ without spin-charge locking. *Proceedings of the National Academy of Sciences of the United States of America*, 114:12430, 2017.

[117] P. Abbamonte, A. Rusydi, S. Smadici, G. D. Gu, G. A. Sawatzky, and D. L. Feng. Spatially modulated mottness in $La_{2-x}Ba_xCuO_4$. *Nature Physics*, 1:155, 2005.

[118] C. Castellani, C. Di Castro, and M. Grilli. Non-Fermi-liquid behavior and d-wave superconductivity near the charge-density-wave quantum critical point. *Zeitschrift für Physik B Condensed Matter*, 103(2):137, 1997.

[119] S. Caprara, C. Di Castro, G. Seibold, and M. Grilli. Dynamical charge density waves rule the phase diagram of cuprates. *Physical Review B*, 95:224511, 2017.

[120] D. Pelc, P. Popčević, M. Požek, M. Greven, and N. Barišić. Unusual behavior of cuprates explained by heterogeneous charge localization. *Science Advances*, 5:eaau4538, 2019.

[121] M. H. Hamidian, S. D. Edkins, C. K. Kim, J. C. Davis, A. P. Mackenzie, H. Eisaki, S. Uchida, M. J. Lawler, E. A. Kim, S. Sachdev, and K. Fujita. Atomic-scale electronic structure of the cuprate d-symmetry form factor density wave state. *Nature Physics*, 12:150, 2016.

[122] H. Eisaki, N. Kaneko, D. L. Feng, A. Damascelli, P. K. Mang, K. M. Shen, Z-X. Shen, and M. Greven. Effect of chemical inhomogeneity in bismuth-based copper oxide superconductors. *Physical Review B*, 69:064512, 2004.

[123] Y. Li, N. Egetenmeyer, J. L. Gavilano, N. Barišić, and M. Greven. Magnetic vortex lattice in $HgBa_2CuO_{4+\delta}$ observed by small-angle neutron scattering. *Physical Review B*, 83(5):054507, 2011.

[124] N. Barišić, M. K. Chan, Y. Li, G. Yu, X. Zhao, M. Dressel, A. Smontara, and M. Greven. Universal sheet resistance and revised phase diagram of the cuprate high-temperature superconductors. *Proceedings of the National Academy of Sciences of the United States of America*, 110(30):12235–12240, 2013.

[125] N. Barišić, S. Badoux, M. K. Chan, C. Dorow, W. Tabis, B. Vignolle, G. Yu, J. Béard, X. Zhao, C. Proust, and M. Greven. Universal quantum oscillations in the underdoped cuprate superconductors. *Nature Physics*, 9(12):761, 2013.

[126] S. I. Mirzaei, D. Stricker, J. N. Hancock, C. Berthod, A. Georges, E. van Heumen, M. K. Chan, X. Zhao, Y. Li, M. Greven, N. Barišić, and D. van der Marel. Spectroscopic evidence for Fermi liquid-like energy and temperature dependence of the relaxation rate in the pseudogap phase of the cuprates. *Proceedings of the National Academy of Sciences of the United States of America*, 110(15):5774, 2013.

[127] M. K. Chan, M. J. Veit, C. J. Dorow, Y. Ge, Y. Li, W. Tabis, Y. Tang, X. Zhao, N. Barišić, and M. Greven. In-plane magnetoresistance obeys Kohler's rule in the pseudogap phase of cuprate superconductors. *Physical Review Letters*, 113(17):177005, 2014.

[128] N. Barišić, M. K. Chan, M. J. Veit, C. J. Dorow, Y. Ge, Y. Li, W. Tabis, Y. Tang, G. Yu, X. Zhao, and M. Greven. Evidence for a universal Fermi-liquid scattering rate throughout the phase diagram of the copper-oxide superconductors. *New Journal of Physics*, 21(11):113007, 2019.

[129] M. K. Chan, C. J. Dorow, L. Mangin-Thro, Y. Tang, Y. Ge, M. J. Veit, G. Yu, X. Zhao, A. D. Christianson, J. T. Park, Y. Sidis, P. Steffens, D. L. Abernathy,

P. Bourges, and M. Greven. Commensurate antiferromagnetic excitations as a signature of the pseudogap in the tetragonal high-T_c cuprate $HgBa_2CuO_{4+\delta}$. *Nature Communications*, 7:10819, 2016.

[130] M. K. Chan, N. Harrison, R. D. McDonald, B. J. Ramshaw, K. A. Modic, N. Barišić, and M. Greven. Single reconstructed Fermi surface pocket in an underdoped single-layer cuprate superconductor. *Nature Communications*, 7:12244, 2016.

[131] P. Popčević, D. Pelc, Y. Tang, K. Velebit, Z. Anderson, V. Nagarajan, G. Yu, M. Požek, N. Barišić, and M. Greven. Percolative nature of the direct-current paraconductivity in cuprate superconductors. *npj Quantum Materials*, 3:42, 2018.

[132] D. Pelc, M. J. Veit, C. J. Dorow, Y. Ge, N. Barišić, and M. Greven. Resistivity phase diagram of cuprates revisited. *arXiv:1902.00529*.

[133] J. P. Hinton, E. Thewalt, Z. Alpichshev, F. Mahmood, J. D. Koralek, M. K. Chan, M. J. Veit, C. J. Dorow, N. Barišić, A. F. Kemper, D. A. Bonn, W. N. Hardy, R. Liang, N. Gedik, M. Greven, A. Lanzara, and J. Orenstein. The rate of quasiparticle recombination probes the onset of coherence in cuprate superconductors. *Scientific Report*, 6:23610, 2016.

[134] A. Yamamoto, W. Z. Hu, and S. Tajima. Thermoelectric power and resistivity of $HgBa_2CuO_{4+\delta}$ over a wide doping range. *Physical Review B*, 63(2):024504, 2000.

[135] U. Chatterjee, J. Zhao, M. Iavarone, R. Di Capua, J. P. Castellan, G. Karapetrov, C. D. Malliakas, M. G. Kanatzidis, H. Claus, J. P. C. Ruff, F. Weber, J. van Wezel, J. C. Campuzano, R. Osborn, M. Randeria, M. Trivedi, M. R. Norman, and S. Rosenkranz. Emergence of coherence in the charge-density wave state of 2H-$NbSe_2$. *Nature Communications*, 6:6313, 2015.

[136] L. Braicovich, M. Moretti Sala, L. J.P. Ament, V. Bisogni, M. Minola, G. Balestrino, D. Di Castro, G. M. De Luca, M. Salluzzo, G. Ghiringhelli, and J. Van Den Brink. Momentum and polarization dependence of single-magnon spectral weight for Cu L_3-edge resonant inelastic X-ray scattering from layered cuprates. *Physical Review B*, 81:174533, 2010.

[137] M. d'Astuto, A. Mirone, P. Giura, D. Colson, A. Forget, and M. Krisch. Phonon dispersion in the one-layer cuprate $HgBa_2CuO_{4+\delta}$. *Journal of Physics: Condensed Matter*, 15(50):8827, 2003.

[138] H. Uchiyama, A. Q. R. Baron, S. Tsutsui, Y. Tanaka, W.-Z. Hu, A. Yamamoto, S. Tajima, and Y. Endoh. Softening of Cu-O bond stretching phonons in tetragonal $HgBa_2CuO_{4+\delta}$. *Physical Review Letters*, 92(19):197005, 2004.

[139] I. Ahmadova, T.C. Sterling, A.C. Sokolik, D. Abernathy, M. Greven and D. Reznik, Phonon spectrum of underdoped $HgBa_2CuO_{4+\delta}$ investigated by neutron scattering. *Preprint*, 2019.

[140] M. W. Haverkort. Theory of resonant inelastic X-ray scattering by collective magnetic excitations. *Physical Review Letters*, 105(16):167404, 2010.

[141] L. J. P. Ament, G. Ghiringhelli, M. M. Sala, L. Braicovich, and J. Van Den Brink. Theoretical demonstration of how the dispersion of magnetic excitations in cuprate compounds can be determined using resonant inelastic X-ray scattering. *Physical Review Letters*, 103:117003, 2009.

[142] M. Le Tacon, G. Ghiringhelli, J. Chaloupka, M. Moretti Sala, V. Hinkov, M. W. Haverkort, M. Minola, M. Bakr, K. J. Zhou, S. Blanco-Canosa, C. Monney, Y. T. Song, G. L. Sun, C. T. Lin, G. M. De Luca, M. Salluzzo, G. Khaliullin, T. Schmitt, L. Braicovich, and B. Keimer. Intense paramagnon excitations in a large family of high-temperature superconductors. *Nature Physics*, 7(9):725, 2011.

[143] Y. Murakami and S. Ishihara. *Resonant X-ray scattering in correlated systems*. Springer, 2017.

[144] L. Braicovich, L. J.P. Ament, V. Bisogni, F. Forte, C. Aruta, G. Balestrino, N. B. Brookes, G. M. De Luca, P. G. Medaglia, F. Miletto Granozio, M. Radovic, M. Salluzzo, J. Van Den Brink, and G. Ghiringhelli. Dispersion of magnetic excitations in the cuprate La_2CuO_4 and $CaCuO_2$ compounds measured using resonant X-ray scattering. *Physical Review Letters*, 102(16):22, 2009.

[145] R. Coldea, S. M. Hayden, G. Aeppli, T. G. Perring, C. D. Frost, T. E. Mason, S. W. Cheong, and Z. Fisk. Spin waves and electronic interactions in La_2CuO_4. *Physical Review Letters*, 86(23):5377, 2001.

[146] N. S. Headings, S. M. Hayden, R. Coldea, and T. G. Perring. Anomalous high-energy spin excitations in the high-T_c superconductor parent antiferromagnet La_2CuO_4. *Physical Review Letters*, 105(24):247001, 2010.

[147] M. P. M. Dean, G. Dellea, R. S. Springell, F. Yakhou-Harris, K. Kummer, N. B. Brookes, X. Liu, Y-J. Sun, J. Strle, T. Schmitt, L. Braicovich, G. Ghiringhelli, I. Božović, and J. P. Hill. Persistence of magnetic excitations in $La_{2-x}Sr_xCuO_4$ from the undoped insulator to the heavily overdoped non-superconducting metal. *Nature Materials*, 12(11):1019, 2013.

[148] L. Braicovich, J. van den Brink, V. Bisogni, M. Moretti Sala, L. J. P. Ament, N. B. Brookes, G. M. De Luca, M. Salluzzo, T. Schmitt, V. N. Strocov, and G. Ghiringhelli. Magnetic excitations and phase separation in the underdoped $La_{2-x}Sr_xCuO_4$ superconductor measured by resonant inelastic X-ray scattering. *Physical Review Letters*, 104:077002, 2010.

[149] W. Kohn and D. Sherrington. Two kinds of Bosons and Bose condensates. *Reviews of Modern Physics*, 42:1, 1970.

[150] W. J. Padilla, Y. S. Lee, M. Dumm, G. Blumberg, S. Ono, Kouji Segawa, Seiki Komiya, Yoichi Ando, and D. N. Basov. Constant effective mass across the phase diagram of high-T_c cuprates. *Physical Review B*, 72:060511, 2005.

[151] S. Ono, S. Komiya, and Y. Ando. Strong charge fluctuations manifested in the high-temperature Hall coefficient of high-T_c cuprates. *Physical Review B*, 75:024515, 2007.

[152] T. Honma and P. H. Hor. Unified electronic phase diagram for hole-doped high-T_c cuprates. *Physical Review B*, 77(18):184520, 2008.

[153] J. W. Alldredge, K. Fujita, H. Eisaki, S. Uchida, and K. Mcelroy. Universal disorder in $Bi_2Sr_2CaCu_2O_{8+x}$. *Physical Review B*, 87(10):104520, 2013.

[154] K. K. Gomes, A. N. Pasupathy, A. Pushp, S. Ono, Y. Ando, and A. Yazdani. Visualizing pair formation on the atomic scale in the high-T_c superconductor $Bi_2Sr_2CaCu_2O_{8+\delta}$. *Nature*, 447:569, 2007.

[155] J. L. Tallon, J. G. Story, J. R. Cooper, and J. W. Loram, Locating the pseudogap closing point in the cuprate superconductors: absence of entrant or reentrant behavior, arXiv:1907.12018.

[156] E. G. Dalla Torre, D. Benjamin, Y. He, D. Dentelski, and E. Demler. Friedel oscillations as a probe of fermionic quasiparticles. *Physical Review B*, 93:205117, 2016.

[157] L. Yue, S. Xue, J. Li, W. Hu, A. Barbour, F. Zheng, L. Wang, J. Feng, S. B. Wilkins, C. Mazzoli, R. Comin, and Y. Li. Distinct fingerprints of charge density waves and electronic standing waves in $ZrTe_3$. *arXiv:1905.06666*.

[158] M. Bluschke, A. Frano, E. Schierle, D. Putzky, F. Ghorbani, R. Ortiz, H. Suzuki, G. Christiani, G. Logvenov, E. Weschke, R. J. Birgeneau, E. H. da Silva Neto, M. Minola, S. Blanco-Canosa, and B. Keimer. Stabilization of three-dimensional charge order in $YBa_2Cu_3O_{6+x}$ via epitaxial growth. *Nature Communications*, 9(1):2978, 2018.

[159] M. R. Norman and A. V. Chubukov. High-frequency behavior of the infrared conductivity of cuprates. *Physical Review B*, 73(14):140501, 2006.

[160] E. van Heumen, E. Muhlethaler, A. B. Kuzmenko, H. Eisaki, W. Meevasana, M. Greven, and D. van der Marel. Optical determination of the relation between the electron-boson coupling function and the critical temperature in high-T_c cuprates. *Physical Review B*, 79:184512, 2009.

[161] N. Doiron-Leyraud, S. Lepault, O. Cyr-Choiniere, B. Vignolle, G. Grissonnanche, F. Laliberté, J. Chang, N. Barišić, M. K. Chan, L. Ji, X. Zhao, Y. Li, M. Greven, C. Proust, and L. Taillefer. Hall, Seebeck, and Nernst coefficients of underdoped $HgBa_2CuO_{4+\delta}$: Fermi-surface reconstruction in an archetypal cuprate superconductor. *Physical Review X*, 3:021019, 2013.

[162] J. A. Krumhansl. Fine scale mesostructures in superconducting and other materials. In *Proceedings of the Conference of the Lattice Effects in High-T_c Superconductors*, January 13-15, 1992.

[163] L. Chaix, G. Ghiringhelli, Y. Y. Peng, M. Hashimoto, B. Moritz, K. Kummer, N. B. Brookes, Y. He, S. Chen, S. Ishida, Y. Yoshida, H. Eisaki, M. Salluzzo, L. Braicovich, Z.-X. Shen, T. P. Devereaux, and W.-S. Lee. Dispersive charge density wave excitations in $Bi_2Sr_2CaCu_2O_{8+\delta}$. *Nature Physics*, 13:952, 2017.

[164] D. Reznik. Phonon anomalies and dynamic stripes. *Physica C*, 481:75, 2012.

[165] S. R. Park, T. Fukuda, A. Hamann, D. Lamago, L. Pintschovius, M. Fujita, K. Yamada, and D. Reznik. Evidence for a charge collective mode associated with superconductivity in copper oxides from neutron and X-ray scattering measurements of $La_{2-x}Sr_xCuO_4$. *Physical Review B*, 89(2):020506, 2014.

[166] S. Dal Conte, C. Giannetti, G. Coslovich, F. Cilento, D. Bossini, T. Abebaw, F. Banfi, G. Ferrini, H. Eisaki, M. Greven, A. Damascelli, D. van der Marel, and F. Parmigiani. Disentangling the electronic and phononic glue in a high-T_c superconductor. *Science*, 335:1600, 2012.

[167] Y. Li, W. Tabis, G. Yu, N. Barišić, and M. Greven. Hidden Fermi-liquid charge transport in the antiferromagnetic phase of the electron-doped cuprate superconductors. *Physical Review Letters*, 117:197001, 2016.

[168] D. Pelc, M. Vučković, M. S. Grbić, M. Požek, G. Yu, T. Sasagawa, M. Greven, and N. Barišić. Emergence of superconductivity in the cuprates via a universal percolation process. *Nature Communications*, 9:4327, 2018.

[169] M. Jurkutat, R. Rybicki, O. P. Sushkov, G. V. M. Williams, A. Erb, and J. Haase. Distribution of electrons and holes in cuprate superconductors as determined from ^{17}O and ^{63}Cu nuclear magnetic resonance. *Physical Review B*, 90:140504, 2014.

[170] T. Wu, H. Mayaffre, S. Krämer, M. Horvatic, C. Berthier, W. N. Hardy, R. Liang, D. A. Bonn, and M. H. Julien. Incipient charge order observed by NMR in the normal state of $YBa_2Cu_3O_y$. *Nature Communications*, 6:6438, 2015.

[171] S. Reichardt, M. Jurukutat, A. Erb, and J. Haase. Charge variations in cuprate superconductors from nuclear magnetic resonance. *Journal of Superconductivity and Novel Magnetism*, 29:3017, 2016.

[172] A. A. Husain, M. Mitrano, M. S. Rak, S. I. Rubeck, B. Uchoa, J. Schneeloch, R. Zhong, G. D. Gu, and P. Abbamonte. Crossover of charge fluctuations across the strange metal phase diagram. *arXiv:1903.04038*.

[173] Y. Li, M. Le Tacon, M. Bakr, D. Terrade, D. Manske, R. Hackl, L. Ji, M. K. Chan, N. Barišić, X. Zhao, M. Greven, and B. Keimer. Feedback effect on high-energy magnetic fluctuations in the model high-Temperature superconductor $HgBa_2CuO_{4+\delta}$ observed by electronic Raman scattering. *Physical Review Letters*, 108:227003, 2012.

[174] B. Loret, N. Auvray, Y. Gallais, M. Cazayous, A. Forget, D. Colson, M.-H. Julien, I. Paul, M. Civelli, and A. Sacuto. Intimate link between charge density wave, pseudogap and superconducting energy scales in cuprates. *Nature Physics*, 15:771, 2019.

[175] S. V. Dordevic, C. C. Homes, J. J. Tu, T. Valla, M. Strongin, P. D. Johnson, G. D. Gu, and D. N. Basov. Extracting the electron-boson spectral function $\alpha^2F(\omega)$ from infrared and photoemission data using inverse theory. *Physical Review B*, 71(10):104529, 2005.

[176] J. Hwang, T. Timusk, E. Schachinger, and J. P. Carbotte. Evolution of the bosonic spectral density of the high-temperature superconductor $Bi_2Sr_2CaCu_2O_{8+\delta}$. *Physical Review B*, 75:144508, 2007.

[177] B. Muschler, W. Prestel, E. Schachinger, J. P. Carbotte, R. Hackl, S. Ono, and Y. Ando. An electron–boson glue function derived from electronic Raman scattering. *Journal of Physics: Condensed Matter*, 22(37):375702, 2010.

[178] L. Fanfarillo, M. Mori, M. Campetella, M. Grilli, and S. Caprara. Glue function of optimally and overdoped cuprates from inversion of the Raman spectra. *Journal of Physics: Condensed Matter*, 28(6):065701, 2016.

[179] O. Ahmadi, L. Coffey, J. F. Zasadzinski, N. Miyakawa, and L. Ozyuzer. Eliashberg analysis of tunneling experiments: Support for the pairing glue hypothesis in cuprate superconductors. *Physical Review Letters*, 106:167005, 2011.

[180] S. A. Kivelson, I. P. Bindloss, E. Fradkin, V. Oganesyan, J. M. Tranquada, A. Kapitulnik, and C. Howald. How to detect fluctuating stripes in the high-temperature superconductors. *Reviews of Modern Physics*, 75:1201, 2003.

[181] M. Le Tacon, A. Bosak, S. M. Souliou, G. Dellea, T. Loew, R. Heid, K.-P. Bohnen, G. Ghiringhelli, M. Krisch, and B. Keimer. Inelastic X-ray scattering in $YBa_2Cu_3O_{6.6}$ reveals giant phonon anomalies and elastic central peak due to charge-density-wave formation. *Nature Physics*, 10:52, 2013.

[182] E. Blackburn, J. Chang, A. H. Said, B. M. Leu, R. Liang, D. A. Bonn, W. N. Hardy, E. M. Forgan, and S. M. Hayden. Inelastic X-ray study of phonon broadening and charge-density wave formation in ortho-ii-ordered $YBa_2Cu_3O_{6.54}$. *Physical Review B*, 88:054506, 2013.

[183] H. Miao, D. Ishikawa, R. Heid, M. Le Tacon, G. Fabbris, D. Meyers, G. D. Gu, A. Q. R. Baron, and M. P. M. Dean. Incommensurate phonon anomaly and the nature of charge density waves in cuprates. *Physical Review X*, 8:011008, 2018.

[184] Y. He, S. Wu, Y. Song, W.-S. Lee, A. H. Said, A. Alatas, A. Bosak, A. Girard, S. M. Souliou, A. Ruiz, M. Hepting, M. Bluschke, E. Schierle, E. Weschke, J.-S. Lee, H. Jang, H. Huang, M. Hashimoto, D.-H. Lu, D. Song, Y. Yoshida, H. Eisaki, Z.-X. Shen, R. J. Birgeneau, M. Yi, and A. Frano. Persistent low-energy phonon broadening near the charge-order q vector in the bilayer cuprate $Bi_2Sr_2CaCu_2O_{8+\delta}$. *Physical Review B*, 98:035102, 2018.

[185] R. J. McQueeney, Y. Petrov, T. Egami, M. Yethiraj, G. Shirane, and Y. Endoh. Anomalous dispersion of LO phonons in $La_{1.85}Sr_{0.15}CuO_4$ at low temperatures. *Physical Review Letters*, 82:628, 1999.

[186] D. Reznik, L. Pintschovius, M. Ito, S. Iikubo, M. Sato, H. Goka, M. Fujita, K. Yamada, G. D. Gu, and J. M. Tranquada. Electron-phonon coupling reflecting dynamic charge inhomogeneity in copper oxide superconductors. *Nature*, 440(7088):1170, 2006.

[187] D. Reznik, L. Pintschovius, J. M. Tranquada, M. Arai, Y. Endoh, T. Masui, and S. Tajima. Temperature dependence of the bond-stretching phonon anomaly in $YBa_2Cu_3O_{6.95}$. *Physical Review B*, 78:094507, 2008.

[188] J. Graf, M. d'Astuto, C. Jozwiak, D. R. Garcia, N. L. Saini, M. Krisch, K. Ikeuchi, A. Q. R. Baron, H. Eisaki, and A. Lanzara. Bond stretching phonon softening and kinks in the angle-resolved photoemission spectra of optimally doped $Bi_2Sr_{1.6}La_{0.4}Cu_2O_{6+\delta}$ superconductors. *Physical Review Letters*, 100:227002, 2008.

[189] H. Uchiyama, A. Q. R. Baron, S. Tsutsui, Y. Tanaka, W.-Z. Hu, A. Yamamoto, S. Tajima, and Y. Endoh. Softening of Cu-O bond stretching phonons in tetragonal $HgBa_2CuO_{4+\delta}$. *Physical Review Letters*, 92:197005, 2004.

[190] D. Reznik, L. Pintschovius, M. Fujita, K. Yamada, G. D. Gu, and J. M. Tranquada. Electron-phonon anomaly related to charge stripes: Static stripe phase versus optimally doped superconducting $La_{1.85}Sr_{0.15}CuO_4$. *Journal of Low Temperature Physics*, 147(3):353, 2007.

[191] V. Thampy, M. P. M. Dean, N. B. Christensen, L. Steinke, Z. Islam, M. Oda, M. Ido, N. Momono, S. B. Wilkins, and J. P. Hill. Rotated stripe order and its competition with superconductivity in $La_{1.88}Sr_{0.12}CuO_4$. *Physical Review B*, 90:100510, 2014.

[192] B. Keimer, N. Belk, R. J. Birgeneau, A. Cassanho, C. Y. Chen, M. Greven, M. A. Kastner, A. Aharony, Y. Endoh, R. W. Erwin, and G. Shirane. Magnetic excitations in pure, lightly doped, and weakly metallic La_2CuO_4. *Physical Review B*, 46:14034, 1992.

[193] M. d'Astuto, G. Dhalenne, J. Graf, M. Hoesch, P. Giura, M. Krisch, P. Berthet, A. Lanzara, and A. Shukla. Sharp optical-phonon softening near optimal doping

in $La_{2-x}Ba_xCuO_{4+\delta}$ observed via inelastic X-ray scattering. *Physical Review B*, 78:140511, 2008.

[194] D. Reznik, T. Fukuda, D. Lamago, A.Q.R. Baron, S. Tsutsui, M. Fujita, and K. Yamada. Q-dependence of the giant bond-stretching phonon anomaly in the stripe compound $La_{1.48}Nd_{0.4}Sr_{0.12}CuO_4$ measured by IXS. *Journal of Physics and Chemistry of Solids*, 69(12):3103, 2008.

[195] S. R. Park, A. Hamann, L. Pintschovius, D. Lamago, G. Khaliullin, M. Fujita, K. Yamada, G. D. Gu, J. M. Tranquada, and D. Reznik. Effects of charge inhomogeneities on elementary excitations in $La_{2-x}Sr_xCuO_4$. *Physical Review B*, 84:214516, 2011.

[196] M. d'Astuto, P. K. Mang, P. Giura, A. Shukla, P. Ghigna, A. Mirone, M. Braden, M. Greven, M. Krisch, and F. Sette. Anomalous dispersion of longitudinal optical phonons in $Nd_{1.86}Ce_{0.14}CuO_{4+\delta}$ determined by inelastic X-Ray scattering. *Physical Review Letters*, 88:167002, 2002.

[197] M. Braden, L. Pintschovius, T. Uefuji, and K. Yamada. Dispersion of the high-energy phonon modes in $Nd_{1.85}Ce_{0.15}CuO_4$. *Physical Review B*, 72:184517, 2005.

[198] J.-G. Zhang, X.-X. Bi, E. McRae, P. C. Eklund, B. C. Sales, and M. Mostoller. Optical studies of single-crystal $Nd_{2-x}Ce_xCuO_{4-\delta}$. *Physical Review B*, 43:5389, 1991.

[199] A. Ino, C. Kim, M. Nakamura, T. Yoshida, T. Mizokawa, A. Fujimori, Z.-X. Shen, T. Kakeshita, H. Eisaki, and S. Uchida. Doping-dependent evolution of the electronic structure of $La_{2-x}Sr_xCuO_4$ in the superconducting and metallic phases. *Physical Review B*, 65:094504, 2002.

[200] T. Yoshida, X. J. Zhou, T. Sasagawa, W. L. Yang, P. V. Bogdanov, A. Lanzara, Z. Hussain, T. Mizokawa, A. Fujimori, H. Eisaki, Z.-X. Shen, T. Kakeshita, and S. Uchida. Metallic behavior of lightly doped $La_{2-x}Sr_xCuO_4$ with a Fermi surface forming an arc. *Physical Review Letters*, 91:027001, 2003.

[201] T. Yoshida, X. J. Zhou, K. Tanaka, W. L. Yang, Z. Hussain, Z.-X. Shen, A. Fujimori, S. Sahrakorpi, M. Lindroos, R. S. Markiewicz, A. Bansil, S. Komiya,

Y. Ando, H. Eisaki, T. Kakeshita, and S. Uchida. Systematic doping evolution of the underlying Fermi surface of $La_{2-x}Sr_xCuO_4$. *Physical Review B*, 74:224510, 2006.

[202] Y. Ando, Y. Kurita, S. Komiya, S. Ono, and K. Segawa. Evolution of the Hall coefficient and the peculiar electronic structure of the cuprate superconductors. *Physical Review Letters*, 92(19):197001, 2004.

[203] J. C. Phillips, A. Saxena, and A. R. Bishop. Pseudogaps, dopants, and strong disorder in cuprate high-temperature superconductors. *Reports on Progress in Physics*, 66(12):2111, 2003.

[204] E. Dagotto. Complexity in strongly correlated electronic systems. *Science*, 309(5732):257, 2005.

[205] S. Uchida, T. Ido, H. Takagi, T. Arima, Y. Tokura, and S. Tajima. Optical spectra of $La_{2-x}Sr_xCuO_4$: Effect of carrier doping on the electronic structure of the CuO_2 plane. *Physical Review B*, 43:7942, 1991.

[206] S. Uchida, K. Tamasaku, and S. Tajima. *c*-axis optical spectra and charge dynamics in $La_{2-x}Sr_xCuO_4$. *Physical Review B*, 53:14558, 1996.

[207] Y. Onose, Y. Taguchi, K. Ishizaka, and Y. Tokura. Charge dynamics in underdoped $Nd_{2-x}Ce_xCuO_4$: Pseudogap and related phenomena. *Physical Review B*, 69:024504, 2004.

[208] A. J. Millis, A. Zimmers, R. P. S. M. Lobo, N. Bontemps, and C. C. Homes. Mott physics and the optical conductivity of electron-doped cuprates. *Physical Review B*, 72:224517, 2005.

[209] J. Fink, N. Nücker, E. Pellegrin, H. Romberg, M. Alexander, and M. Knupfer. Electron energy-loss and X-ray absorption spectroscopy of cuprate superconductors and related compounds. *Journal of Electron Spectroscopy and Related Phenomena*, 66(3):395, 1994.

[210] P. Abbamonte, C. A. Burns, E. D. Isaacs, P. M. Platzman, L. L. Miller, S. W. Cheong, and M. V. Klein. Resonant inelastic X-Ray scattering from valence excitations in insulating copper oxides. *Physical Review Letters*, 83:860, 1999.

[211] M. Z. Hasan, E. D. Isaacs, Z.-X. Shen, L. L. Miller, K. Tsutsui, T. Tohyama, and S. Maekawa. Electronic structure of mott insulators studied by inelastic X-ray scattering. *Science*, 288(5472):1811, 2000.

[212] L. Lu, G. Chabot-Couture, X. Zhao, J. N. Hancock, N. Kaneko, O. P. Vajk, G. Yu, S. Grenier, Y. J. Kim, D. Casa, T. Gog, and M. Greven. Charge-transfer excitations in the model superconductor $HgBa_2CuO_{4+\delta}$. *Physical Review Letters*, 95:217003, 2005.

[213] K. Ishii, K. Tsutsui, Y. Endoh, T. Tohyama, K. Kuzushita, T. Inami, K. Ohwada, S. Maekawa, T. Masui, S. Tajima, Y. Murakami, and J. Mizuki. Mott gap excitations in twin-free $YBa_2Cu_3O_{7-\delta}$ ($T_c = 93$ K) studied by resonant inelastic X-Ray scattering. *Physical Review Letters*, 94:187002, 2005.

[214] K. Ishii, K. Tsutsui, T. Tohyama, T. Inami, J. Mizuki, Y. Murakami, Y. Endoh, S. Maekawa, K. Kudo, Y. Koike, and K. Kumagai. Momentum-dependent charge excitations of a two-leg ladder: Resonant inelastic X-ray scattering of $(La, Sr, Ca)_{14}Cu_{24}O_{41}$. *Physical Review B*, 76:045124, 2007.

[215] Y. J. Kim, J. P. Hill, C. A. Burns, S. Wakimoto, R. J. Birgeneau, D. Casa, T. Gog, and C. T. Venkataraman. Resonant inelastic X-ray scattering study of charge excitations in $La_{2-x}Sr_xCuO_4$. *Physical Review Letters*, 89:177003, 2002.

[216] Y.-J. Kim, J. P. Hill, S. Komiya, Y. Ando, D. Casa, T. Gog, and C. T. Venkataraman. Doping dependence of charge-transfer excitations in $La_{2-x}Sr_xCuO_4$. *Physical Review B*, 70:094524, 2004.

[217] D. S. Ellis, J. Kim, H. Zhang, J. P. Hill, G. Gu, S. Komiya, Y. Ando, D. Casa, T. Gog, and Y.-J. Kim. Electronic structure of doped lanthanum cuprates studied with resonant inelastic X-ray scattering. *Physical Review B*, 83:075120, 2011.

[218] S. Wakimoto, K. Ishii, H. Kimura, K. Ikeuchi, M. Yoshida, T. Adachi, D. Casa, M. Fujita, Y. Fukunaga, T. Gog, Y. Koike, J. Mizuki, and K. Yamada. Resonant

inelastic X-ray scattering study of intraband charge excitations in hole-doped high-T_c cuprates. *Physical Review B*, 87:104511, 2013.

[219] S. Ono, S. Komiya, and Y. Ando. Strong charge fluctuations manifested in the high-temperature Hall coefficient of high-T_c cuprates. *Physical Review B*, 75:024515, 2007.

[220] K. Ishii, K. Tsutsui, Y. Endoh, T. Tohyama, S. Maekawa, M. Hoesch, K. Kuzushita, M. Tsubota, T. Inami, J. Mizuki, Y. Murakami, and K. Yamada. Momentum dependence of charge excitations in the electron-doped superconductor $Nd_{1.85}Ce_{0.15}CuO_4$: A resonant inelastic X-ray scattering study. *Physical Review Letters*, 94:207003, 2005.

[221] C. J. Jia, C.-C. Chen, A. P. Sorini, B. Moritz, and T. P. Devereaux. Uncovering selective excitations using the resonant profile of indirect inelastic X-ray scattering in correlated materials: observing two-magnon scattering and relation to the dynamical structure factor. *New Journal of Physics*, 14(11):113038, 2012.

[222] Y.-J. Kim, J. P. Hill, G. D. Gu, F. C. Chou, S. Wakimoto, R. J. Birgeneau, S. Komiya, Y. Ando, N. Motoyama, K. M. Kojima, S. Uchida, D. Casa, and T. Gog. Molecular orbital excitations in cuprates: Resonant inelastic X-ray scattering studies. *Physical Review B*, 70:205128, Nov 2004.

[223] K. Tsutsui, T. Tohyama, and S. Maekawa. Mott gap excitations and resonant inelastic X-ray scattering in doped cuprates. *Physical Review Letters*, 91:117001, 2003.

[224] E. M. Motoyama, G. Yu, I. M. Vishik, O. P. Vajk, P. K. Mang, and M. Greven. Spin correlations in the electron-doped high-transition-temperature superconductor $Nd_{2-x}Ce_xCuO_{4-\delta}$. *Nature*, 445(7124):186, 2007.

[225] Y. Li. *Neutron Scattering, Muon Spin Rotation/Relaxation, and Charge Transport Study of the Electron-Doped Cuprate Superconductors.* PhD thesis, University of Minnesota, 2017.

[226] K. Ishii, M. Hoesch, T. Inami, K. Kuzushita, K. Ohwada, M. Tsubota, Y. Murakami, J. Mizuki, Y. Endoh, K. Tsutsui, T. Tohyama, S. Maekawa, K. Yamada,

T. Masui, S. Tajima, H. Kawashima, and J. Akimitsu. Momentum-resolved charge excitations in high-T_c cuprates studied by resonant inelastic X-ray scattering. *Journal of Physics and Chemistry of Solids*, 69(12):3118, 2008.

[227] L. Lu, J. N. Hancock, G. Chabot-Couture, K. Ishii, O. P. Vajk, G. Yu, J. Mizuki, D. Casa, T. Gog, and M. Greven. Incident energy and polarization-dependent resonant inelastic X-ray scattering study of La_2CuO_4. *Physical Review B*, 74(22):224509, 2006.

[228] J. T. Ye, Y. J. Zhang, R. Akashi, M. S. Bahramy, R. Arita, and Y. Iwasa. Superconducting dome in a gate-tuned band insulator. *Science*, 338:1193, 2012.

[229] M. Nakano, K. Shibuya, D. Okuyama, T. Hatano, S. Ono, M. Kawasaki, Y. Iwasa, and Y. Tokura. Collective bulk carrier delocalization driven by electrostatic surface charge accumulation. *Nature*, 487(7408):459, 2012.

[230] S. Asanuma, P.-H. Xiang, H. Yamada, H. Sato, I. H. Inoue, H. Akoh, A. Sawa, K. Ueno, H. Shimotani, H. Yuan, M. Kawasaki, and Y. Iwasa. Tuning of the metal-insulator transition in electrolyte-gated $NdNiO_3$ thin films. *Applied Physics Letters*, 97(14):142110, 2010.

[231] H. Ji, J. Wei, and D. Natelson. Modulation of the electrical properties of VO_2 nanobeams using an ionic liquid as a gating medium. *Nano Letters*, 12(6):2988, 2012.

[232] Z. Yang, Y. Zhou, and S. Ramanathan. Studies on room-temperature electric-field effect in ionic-liquid gated VO_2 three-terminal devices. *Journal of Applied Physics*, 111(1):014506, 2012.

[233] L. M. Zheng, X. R. Wang, W. M. Lü, C. J. Li, T. R. Paudel, Z. Q. Liu, Z. Huang, S. W. Zeng, K. Han, Z. H. Chen, X. P. Qiu, M. S. Li, S. Yang, B. Yang, M. F. Chisholm, L. W. Martin, S. J. Pennycook, E. Y. Tsymbal, J. M. D. Coey, and W. W. Cao. Ambipolar ferromagnetism by electrostatic doping of a manganite. *Nature Communications*, 9:1897, 2018.

[234] Q. Lu and B. Yildiz. Voltage-controlled topotactic phase transition in thin-film $SrCoO_x$ monitored by in situ X-ray diffraction. *Nano Letters*, 16(2):1186, 2016.

[235] D. A. Gilbert, A. J. Grutter, P. D. Murray, R. V. Chopdekar, A. M. Kane, A. L. Ionin, M. S. Lee, S. R. Spurgeon, B. J. Kirby, B. B. Maranville, A. T. N'Diaye, A. Mehta, E. Arenholz, K. Liu, Y. Takamura, and J. A. Borchers. Ionic tuning of cobaltites at the nanoscale. *Physical Review Materials*, 2:104402, 2018.

[236] M. A. Torija, M. Sharma, M. R. Fitzsimmons, M. Varela, and C. Leighton. Epitaxial $La_{0.5}Sr_{0.5}CoO_3$ thin films: structure, magnetism, and transport. *Journal of Applied Physics*, 104(2):023901, 2008.

[237] M. A. Torija, M. Sharma, J. Gazquez, M. Varela, C. He, J. Schmitt, J. A. Borchers, M. Laver, S. El-Khatib, and C. Leighton. Chemically driven nanoscopic magnetic phase separation at the $SrTiO_3(001)/La_{1-x}Sr_xCoO_3$ interface. *Advanced Materials*, 23(24):2711, 2011.

[238] S. Kelly, F. Galli, J. Aarts, S. Bose, M. Sharma, and C. Leighton. Direct real space observation of magneto-electronic inhomogeneity in ultra-thin film $La_{0.5}Sr_{0.5}CoO_{3-\delta}$ on $SrTiO_3(001)$. *Applied Physics Letters*, 105(11):112909, 2014.

[239] S. Medling, Y. Lee, H. Zheng, J. F. Mitchell, J. W. Freeland, B. N. Harmon, and F. Bridges. Evolution of magnetic oxygen states in Sr-doped $LaCoO_3$. *Physical Review Letters*, 109(15):157204, 2012.

[240] J. Gazquez, S. Bose, M. Sharma, M. A. Torija, S. J. Pennycook, C. Leighton, and M. Varela. Lattice mismatch accommodation via oxygen vacancy ordering in epitaxial $La_{0.5}Sr_{0.5}CoO_{3-\delta}$ thin films. *APL Materials*, 1(1):012105, 2013.

[241] J. W. Freeland, J. X. Ma, and J. Shi. Ferromagnetic spin-correlations in strained $LaCoO_3$ thin films. *Applied Physics Letters*, 93(21):212501, 2008.